Inversion of Surface Contacting Antenna Measurements for Sea Ice Complex Permittivity Reconstruction

Tyler Matthew Tiede

A Thesis Submitted to the Faculty of Graduate Studies of
the University of Manitoba
in partial fulfillment of the requirements of the degree of

Master of Science

Department of Electrical and Computer Engineering
University of Manitoba
Winnipeg, Manitoba, Canada

Abstract

The need to monitor geophysical properties of first year ice (FYI) in the Arctic is increasing as this type of sea ice becomes more prevalent. One such method of monitoring the Arctic is the use of electromagnetic remote sensing techniques. These methods determine dielectric properties of the illuminated sea ice by interpreting how the electromagnetic waves interact within the medium. In the literature, there are empirical formulas relating these dielectric properties to the geophysical properties of the sea ice. The contributions of this research are the development and testing of a surface based active microwave remote sensor to monitor sea ice growth in the winter through the reconstruction of the time series complex permittivity profile of FYI.

To collect experimental data, we designed an antenna, and collected measurements in the winter of 2015 and 2016 at the Sea-ice Environmental Research Facility (SERF). In these experiments, we collected antenna measurements as well as performed physical sampling of the sea ice. In addition, cold lab experiments were utilized to gauge the sensitivity of our antenna to the geophysical properties of sea ice.

To process the measured data, we developed an inversion algorithm which reconstructs the unknown parameters by minimizing a data misfit cost function. This cost function represents the discrepancy between the measured data and the simulated data by a transmission line based forward solver due to predicted unknowns. To this end, we used simulated annealing (SA) as the global optimization technique to iteratively optimize the cost function. The method was able to follow the general time series trend of the sea ice properties for synthetically collected data. With regards to experimental measurements, we needed to develop a data calibration procedure to alleviate our modeling error. We then presented preliminary inversion results using these calibrated measured data. The model is still in the preliminary stages, and as such, future expansion on this model could prove useful to the Arctic remote sensing community.

Contributions

The contributions of this thesis are:

- **Data collection**
  - The design and fabrication of an open-ended waveguide (OEW) antenna having a low mismatch loss with snow-covered sea ice over the frequency range of 3 GHz to 5 GHz. To this end, we inserted an ultra-high molecular weight (UHMW) plastic into the OEW's cavity to match with snow.
  - We performed near-field (NF) and far-field (FF) measurements of the OEW in free space. These measurements give a comparison to general pattern of the fields inside sea ice.
  - Using cold room experiments, a sensitivity analysis was performed on the antenna with respect to different salinity, temperatures, and thicknesses of sea ice.
  - Time series antenna measurements, salinity, temperature, and thickness profile collected at the SERF during winter 2015 and 2016.
- **Data calibration**
  - Adapting a data calibration process from microwave tomography to this application.
- **Data processing**
  - The development of a MATLAB computer code to reconstruct the time series complex permittivity profile of sea ice. The method consisted of a single layer and a three layer model. The developed algorithms were tested with synthetic and experimental data. Key aspects of the technique were:
    - Simulated annealing for continuous model parameters.
    - Transmission line based forward solver rather than a full wave scattering inversion.

Below we provide a list of the published work during this research.

Submitted Refereed Journal Papers

1. Nariman Firoozy, Thomas Nuesitzer, Durrel Desmond, **Tyler Tiede**, Marcos Lemes, Jack Landy, Puyan Mojabi, Sø ren Rysgaard, Gary Stern, and David Barber, "Electromagnetic detection of crude oil spill in young sea ice - A case study," IEEE Transactions on Geoscience and Remote Sensing. (in review).
    - Role: Help with SERF data collection and physical sampling.
    - Note: The results of this paper are not within the scope of this thesis.

Refereed Conference Papers

1. **Tyler Tiede**, Nariman Firoozy, Thomas Neusitzer, Puyan Mojabi, and David Barber, "Complex Permittivity Profile Reconstruction of Sea Ice using a Transmission Line Model," APS/URSI 2016, July 2016.
    - Role: Lead researcher.
2. **Tyler Tiede**, Puyan Mojabi, and David Barber, "Challenges of Implementing an RF Sensor in the Arctic," ArcticNet Annual Scientific Meetings, December 2016.
    - Role: Lead researcher.
3. Puyan Mojabi, Nariman Firoozy, Nozhan Bayat, Trevor Brown, Chaitanya Narendra, Pedram Mojabi, Chen Niu, **Tyler Tiede**, Thomas Neusitzer, Xiang Li, Ian Jeffrey, Joe LoVetri, and David Barber, "Electromagnetic Inversion for Biomedical Imaging, Antenna Characterization, and Sea Ice Remote Sensing Applications," URSI AsiaPacific Radio Science Conference, August 21-25, 2016.
    - Role: Active participant in SERF data collection and physical sampling.

Acknowledgments

I would like to express my gratitude to my academic advisors, Dr. Puyan Mojabi and Dr. David Barber for their continuous advice, guidance, and encouragement throughout the research work. I would also like to thank Dr. Dustin Isleifson and Dr. Tim Papakyriakou for reviewing my thesis. I thank my friends and colleagues for making the days enjoyable. Without them, this time would have not been nearly as exciting. I would also like to express my appreciation to Brad Tabachnick, David Binne, and Cory Smit for their technical support and use of equipment for this research.

Finally, I thank my parents for everything they have done for me. Your love and support growing up has allowed me to accomplish all that I have done. Ma, you make amazing potato salad. Dad, you are a great fishing buddy.

To my parents

Contents

List of Tables

List of Figures

List of Abbreviations

AUT	Antenna Under Test
CATR	Compact Antenna Test Range
CEOS	Center for Earth Observation Science
FF	Far-Field
FYI	First Year Ice
GPR	Ground Penetrating Radar
HFSS	High Frequency Structure Simulator
MYI	Multi-year Ice
NF	Near-Field
NRCS	Normalized Radar Cross Section
OEW	Open-ended Waveguide
PSU	Practical Salinity Unit
SA	Simulated Annealing
SAR	Synthetic Aperture Radar
SERF	Sea-ice Environmental Research Facility
SNFR	Spherical Near-field Range
S_{11}	Scattering Parameter
UHMW	Ultra High Molecular Weight
VNA	Vector Network Analyzer

1

Introduction

Broadly speaking, this research falls into the area of electromagnetic inversion at the microwave frequency range. "Electromagnetic inversion is defined as the process by which some properties of an investigation domain are inferred from external electromagnetic observations" [4]. In this research, our investigation domain is sea ice, and the properties to be determined are thickness and dielectric properties (complex permittivity). We investigate the use of a single antenna element, which is in direct contact with the top surface of the investigation domain, to collect the external measured data. These measured data are then to be used to reconstruct the unknowns, internal parameters, by solving the associated electromagnetic inverse problem. Electromagnetic inversion often requires three steps: data collection, data calibration, and data processing (inversion algorithm) [4]. This thesis addresses all these three steps for the proposed remote sensing strategy.

The research work completed for this thesis was the design and fabrication of an active microwave device for electromagnetic remote sensing of sea ice growth in the Arctic. A global

optimization technique, utilizing a transmission line based forward solver, was created to relate measured data to the complex permittivity profile of the sea ice. A calibration factor was then implemented in an attempt to relate the transmission line and physical model. This chapter will give reason for this research, followed by an outline of the thesis.

1.1 Motivation

Climate change is a big concern as temperatures increase. Studies show a decline in the amount of multi-year sea ice (MYI) due to increase in global temperatures [5]. This MYI is being replaced by seasonal first year sea ice. The formation of thinner sea ice leads to changes in both dynamic and thermodynamic characteristics. These changes impact the Arctic environment, Arctic transportation, and the oil industry. As the sea ice becomes thinner, the Arctic will start to see more human presence. There are certain risks associated with this increase in activity such as damage to ships and oil spills. Therefore, it is crucial to develop different monitoring techniques of sea ice in preparation of the influx of human activity in the Arctic. Sea ice is a complicated structure, where no one system can characterize every aspect. An array of sensors are required to monitor sea ice, especially when oil contaminated [6]. To this end, we chose to focus on the time series growth of FYI in the winter. This includes snowfall on the sea ice.

The use of active remote sensing is an effective method of sea ice monitoring. Within the framework of active microwave remote sensing in the Arctic, devices such as synthetic aperture radar (SAR) systems and ground-based scatterometers are used [7]. Data obtained from these systems can be processed by appropriate inversion algorithms (e.g. electromagnetic inverse scattering algorithms) in order to reconstruct the properties of sea ice [8].

Unfortunately, these systems can be quite expensive and/or not provide enough temporal

resolution. That is, sensors such as space-borne SARs can only take measurements when the surface is in its field of vision. Surface based sensors have the advantage in cases where high temporal resolution is required (such as oil spill detection). As well, the cost can be significantly less than space-borne or airborne remote sensors. Another factor to consider is that the retrieval algorithms for active microwave remote sensing require "sufficient" data. To this end, scatterometers have relatively low bandwidth and use multiple incident angles in order to acquire sufficient data. To achieve different angles, typically the system must reposition the sensor which can be a costly component.

In this thesis, we look to use multiple frequency measurements in order to collect sufficient data for the inversion algorithm. We look to develop a surface based active remote sensor that is relatively cost effective, to be an addition to these current methods. This sensor will be able to provide high temporal resolution of the complex permittivity profile of FYI growth in the winter. As well, we look to be able to monitor the diurnal effects on the surface layers of the sea ice. That is, measure the effects of brine movement within the surface layer of the ice.

The vision of this research is to deploy a network of these sensors across an area of interest. They would connect wirelessly to a base station where the raw data would be processed by the inversion algorithm. As well, they would be equipped with GPS in order to track location. This mapping of the sea ice would provide information about ice growth, ice movement, and would have the potential of tracking oil contaminants.

1.2 Thesis Outline

This thesis provides an electromagnetic-based approach to the monitoring of the time series growth of snow-covered sea ice during freeze up in the Arctic. The outline of the thesis is

as follows:

Chapter 2 provides an overview of the Arctic environment and descriptions of the engineering concepts used in this research. The topics discussed include: 1) geophysics and thermodynamics of snow-covered sea ice, 2) electromagnetic remote sensing, and 3) geophysical inversion.

In Chapter 3, we design an antenna that is capable of penetrating into snow-covered sea ice. We discuss the optimization process and our results using a modeling software, ANSYS HFSS. We present the simulated S_{11} and near-field of the optimized antenna.

In Chapter 4, a series of experiments are conducted on the fabricated antenna to verify simulation results. To this end, we performed anechoic chamber experiments to confirm the radiation pattern of the antenna. In addition, we outline the experimental setup and test techniques that were used when performing measurements on sea ice. We then studied the effects low temperature has on the calibration of the antenna and experimental setup.

Chapter 5 presents the experimental data collected from SERF 2015 and SERF 2016. This data includes the antenna measurements and physical samples of sea ice. As well, a cold laboratory experiment was conducted to analyze the antenna sensitivity to sea ice geophysical properties.

In Chapter 6, we process our SERF 2015 data to generate our true complex permittivity profiles. We then discuss a transmission line model forward solver to be used in our geophysical inversion. Finally, a calibration technique is presented which is used to relate the transmission line model to the true physical model of the snow-covered sea ice.

Finally, Chapter 7 presents an inversion technique using simulated annealing. This inversion is used to reconstruct the time series complex permittivity profile of sea ice from simulated

and measured S_{11} data. The results and performance of the algorithm are given for simulated and for calibrated experimental measurements. Finally, Chapter 8 concludes with a summary of the objectives and the results of the project.

2

Background

This chapter provides background from three areas of study which are critical to this research. These fields include: geophysical and thermodynamics of snow-covered sea ice, electromagnetic remote sensing, and geophysical inversion. We begin with the characterization of the problem domain (snow and sea ice). Following, we present the background on electromagnetic remote sensing which is used in the acquisition of our data. Finally, we will discuss the basics of geophysical inversion and the specific method chosen for this research.

2.1 Geophysics and Thermodynamics of Snow-Covered Sea Ice

The Arctic is a complex environment due to the interconnection between geophysical, thermodynamic, biological, hydrological, and atmospheric conditions [9]. Snow-covered sea ice affects all of these conditions, and is the medium we focus on in this research. To this end, we limit the discussion to Arctic topics pertinent to this research.

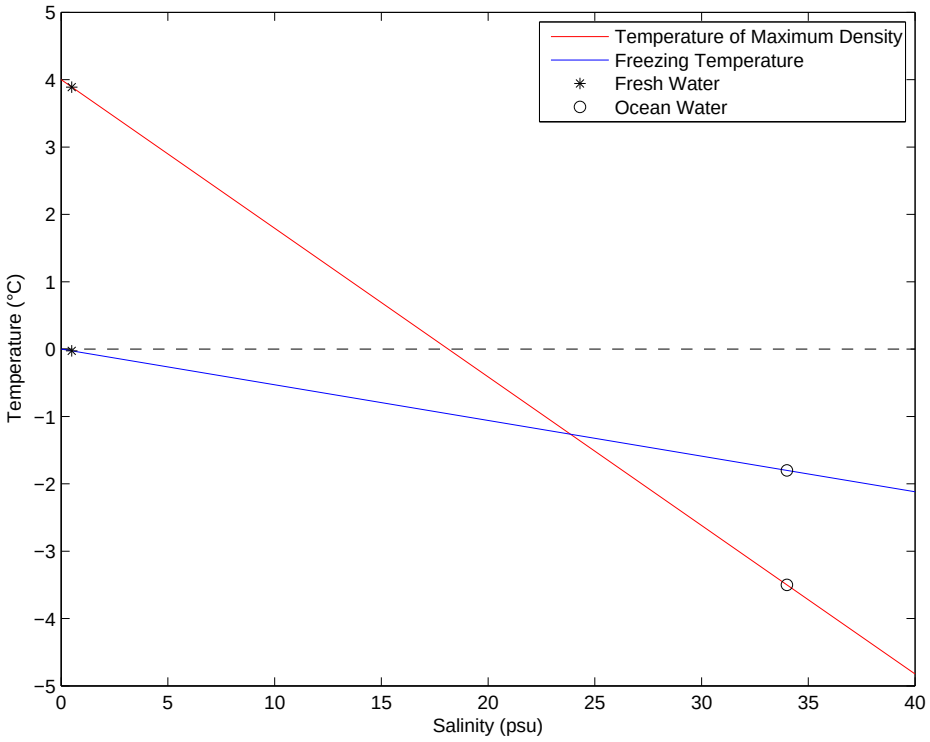

Fig. 2.1: The freezing temperature and maximum density are inversely proportional to salinity. For fresh water (red line) the temperature of maximum density is greater than the freezing point, whereas in sea water (blue line), the temperature of maximum density is lower than the freezing point [1, 2].

2.1.1 Initial Sea Ice Formation

We begin with a discussion on the initial formation of sea ice. Sea ice typically forms slower than pure ice due to the presence of dissolved salts in the ocean [1]. Sea water salinity is 35 psu on average, though 34 psu is common in the Arctic and Antarctic regions [2]. Water salinity within the Canadian Archipelago are often found to be close to 30 psu. The main salt dissolved in sea water is sodium chloride, though other salts such as sodium sulfate, magnesium sulfate, and magnesium chloride are present.

The freezing temperature and temperature of maximum density of water is inversely proportional to salinity, as shown in Figure 2.1. Pure water freezes at a higher temperature ($0°C$) than sea water ($-1.86°C$ with a salinity of 34 psu). In addition, pure ice at the freezing point

floats due to being less dense than the warmer water underneath. On the other hand, sea ice at the freezing point sinks due to having a higher density than the water underneath; this produces a convective effect within the surface layers. It should be noted that fresh water has this vertical convection, but only until the surface layer temperature reaches the maximum density at approximately $4°C$ (above freezing temperature). Of course, other factors such as wind can cause circulation of the water column.

There is a large increase in density at the base of the ocean surface layers (100 m to 150 m) called the pycnocline [10]. Due to this large increase in density, only the surface layers of the ocean must be near freezing in order for sea ice to form. The need to have these surface layers below freezing is another reason that makes sea ice formation slower than pure ice in similar climatic conditions. Overall, more heat must be removed in sea water compared to fresh water in order to freeze [2].

After the surface layers of the ocean are sufficiently cold, randomly oriented ice crystals, known as frazil ice, begin to form at the surface [9]. These crystals are approximately 3 mm to 4 mm in diameter. The term grease ice is given to the soup-like mixture as these crystals coalesce.

The subsequent freezing process of grease ice is dependent on oceanic and atmospheric conditions [11]. These conditions can be separated into: 1) calm, 2) turbulent, and 3) combination of (1) and (2). Initially, sea ice grows laterally along the surface of the sea water where there is contact with the colder Arctic air. Under calm conditions the ice crystals amass into a uniformly thin sheet of ice called nilas. When there is turbulence, ocean swell or wave action, the crystals freeze together to form circular discs [12, 13]. The discs then aggregate to form pancake ice. Typically a combination of calm and turbulent conditions occur during this freezing process [11]. This combination can lead to nilas breaking apart and forming into pancake ice, or grease ice can develop into nilas if the waves subside.

The ice layers formed under the initial surface layer have a different texture. These subsequent layers transition from granular ice to congelation ice. Congelation ice has a distinct columnar crystal texture due to the downward growth of the ice. This growth is caused by the conductive heat flux of the ice floe being directed primarily upwards. Initially we have fairly rapid ice growth. As the ice thickens, this heat flux decreases resulting in slower ice growth. This is due to the temperature gradient of the ice decreasing. The heat flux of sea ice is given by

$$F = -K\frac{\partial T}{\partial z} \tag{2.1}$$

where K is the thermal conductivity in $\frac{Watts}{meter \cdot Kelvin}$, T is the temperature in Kelvin, and z is the vertical direction of the ice sheet [2]. The thermal conductivity of sea ice is influenced by temperature, salinity, and the volume fraction of brine and air. Typically, the thermal conductivity of sea ice is lower than that of pure ice due to the inclusions in sea ice (brine and air) being poor thermal conductors.

These are some ideal simple cases of ice growth. At any point in the freezing process, wave action, collisions with other ice structures, solar and temperature fluctuations can alter the structure of ice [2]. For the scope of this thesis, it is sufficient to end the discussion with ideal lateral and vertical ice growth.

2.1.2 Salinity and Brine Movement

First year ice typically has a C-shaped salinity profile where the top and bottom layer of the ice is more saline than the middle section [2]. This phenomenon is caused by the way brine moves within the ice during growth. Brine movement in sea ice is primarily influenced by a combination of molecular diffusion and advection.

A simplified description of brine movement is as follows. As the temperature of the upper

layers decrease, the encapsulated brine pockets decrease in size due to the water molecules freezing [9]. The newly formed ice precipitates salts causing the salinity, as well as the density, of the brine to increase. Naturally, the brine will tend to travel downward through the ice towards the ocean through brine channels. These channels can be created, but are not limited to, the initial freezing process or the superheating of brine due to the introduction of more saline brine from above. However, brine channels decrease in size as temperature decreases resulting in brine being trapped in the upper layer of the ice; the porosity of the sea ice decreases with temperature.

From this basic description of brine movement, we can see that sea ice is a complex structure composed of pure ice, brine, and air pockets. It is the volume fraction of these three geophysical components that influence complex permittivity of the ice. As well, temperature of the sea ice plays a major role in the volume fraction of each component [14].

2.1.3 Snow Fall on Sea Ice

The albedo of a material indicates how well solar radiation is reflected [13]. Sea ice and snow have a much higher albedo than the ocean. This results in the sea ice and snow having a major influence on the heat exchange between the atmosphere and the ocean. In this thesis, we primarily focus on sea ice with no snow cover. However, even a thin layer of snow plays a significant part in the heat transfer between the atmosphere and ocean [2]. The snow acts as a thermal insulator for the sea ice. To this end, we present a rather quick summary of snowfall on sea ice since it plays a major role in the Arctic environment.

Snow can be characterized into dry and wet snow. The properties of the snow change rather quickly due to changes in atmospheric temperature, humidity, and pressure [9]. The variation in snow properties increases as the snow ages. At the snow/ice interface a layer of

highly saline, relatively large snow grains (hoar layer) can be found. This layer forms due to brine from the sea ice mixing with the snow base.

With respect to remote sensing, the wetness of the snow has a major impact on the electromagnetic waves propagating in it [2]. As well, the micro-structure of the snow pact can have significant effects on the propagation and scattering of these waves. In the next section, we will discuss how these geophysical properties influence wave propagation.

2.2 Electromagnetic Remote Sensing

Remote sensing in the Arctic provides a means of obtaining information about the environment from a distance [15]. Remote sensors can be separated into active and passive. The former type of sensor emits energy towards the target and measures the reflected or backscattered signal. The latter sensor does not emit energy (*i.e.*, does not irradiate the object), rather it measures natural energy that is emitted by the target being observed. In this thesis, we focus on active electromagnetic remote sensing.

In active electromagnetic remote sensing, there are a variety of common sensors used such as scatterometers, SARs, and ground penetrating radars (GPR) [16]. Inherently, these sensors are all a form of non-destructive measurements since they do not alter the target or object. As stated in Chapter 1, the sensor designed for this research is an active microwave remote sensor that is situated directly on the target we are to measure. As well, the sensor uses a continuous wave, rather than pulse waves, in order to interrogate our target. To this end, we will limit our discussion to time harmonic electromagnetics (the time dependency is assumed to be $\exp(+j\omega t)$ where $j^2 = -1$, ω is the angular frequency, and t denotes the time). We will begin with describing time harmonic waves absent of sources (antennas in our case), followed by a discussion on the fundamentals of antennas. Finally we end this section with

the mixing models relating the electrical and physical properties of snow-covered sea ice.

2.2.1 Time Harmonic Waves in Dielectric Medium

We begin this discussion with Maxwell's equations in the frequency domain in order to formulate our time harmonic wave equations. The Maxwell equations are a set of partial differential equations that describe the way in which fields can exist. We start with the following (Faraday) equation

$$\boldsymbol{\nabla} \times \boldsymbol{E} = -j\omega\mu\boldsymbol{H} \tag{2.2}$$

where $\boldsymbol{E}$ is the electric field intensity, ω is the angular frequency, μ is the permeability of the material[1], $\boldsymbol{H}$ is the magnetic flux intensity, and the operator $\boldsymbol{\nabla}\times$ denotes the curl operator. Equation (2.2) states that a time-varying magnetic field will always have a spatially-varying electric field. Next we have the following equation, which is the extended for of Ampére's law

$$\boldsymbol{\nabla} \times \boldsymbol{H} = \boldsymbol{J} + j\omega\epsilon\boldsymbol{E} \tag{2.3}$$

where $\boldsymbol{J}$ is the electric current density, and ϵ is the permittivity of the material. We define the permittivity $\epsilon = \epsilon_o\epsilon_r$ where ϵ_o is the permittivity of free space ($\epsilon_o = 8.854 \times 10^{-12}\ \frac{F}{m}$) and $\epsilon_r = \epsilon' - j\epsilon''$ (real and imaginary parts). This law states that the magnetic field induced around a closed loop is proportional to the electric current and the rate of change of the electric field. Following, we have Guass's law, given by

$$\boldsymbol{\nabla} \cdot (\epsilon\boldsymbol{E}) = \rho \tag{2.4}$$

where ρ is the electric charge density. Gauss's law states that $\boldsymbol{E}$ leaving a volume is proportional to the charge contained within. Finally we have the following law for magnetism,

[1] In our research, we do not work with magnetic materials, therefore we assume $\mu = \mu_o = 4\pi \times 10^{-7}\ \frac{H}{m}$.

given by

$$\boldsymbol{\nabla} \cdot (\mu \boldsymbol{H}) = 0 \tag{2.5}$$

Simply put, this law stems from there being no magnetic monopoles which results in the magnetic flux through a closed surface being zero. Now that we have our set of laws governing field interactions, we can look to solve for time harmonic waves in our medium which is free of sources.

In a non-magnetic, conductive, lossy homogeneous medium with no sources, we can take the curl of both sides of (2.2), and substituting in (2.4) and (2.3) as necessary, to obtain the homogeneous Helmholtz wave equation, given by

$$\nabla^2 \mathbf{E} + \gamma^2 \mathbf{E} = 0 \tag{2.6}$$

where γ is

$$\gamma = \omega \sqrt{\mu_o \epsilon_o (\epsilon' - j \frac{\sigma_s + \omega \epsilon_o \epsilon''}{\omega \epsilon_o})} \tag{2.7}$$

and where σ_s is the ionic conductivity of our medium. We note that our loss, or imaginary part of our complex permittivity, is a combination of the ionic conductivity and the dispersive property, ϵ''. The latter term, which is frequency dependent, refers to the loss of energy due to the polarization of the material in the presence of an oscillating or changing electric field. As the fields oscillate, there may not be enough time for the material to reach equilibrium. Therefore, energy is needed to counteract the particles opposing momentum. In the context of this research, we assume this value to be constant since we are dealing with a relatively narrow frequency range. To simplify the problem, an effective loss, ϵ''_{eff}, is introduced and defined as

$$\epsilon''_{eff} = \frac{\sigma_s + \omega \epsilon_o \epsilon''}{\omega \epsilon_o}. \tag{2.8}$$

Let's now consider a plane wave which satisfies the Helmholtz equation. A plane wave

is a wave whose surfaces of constant phase are parallel planes normal to the direction of propagation. If we are far from a source, and look at a small section of a wavefront, we can approximate most wave fronts as plane waves. Another important property of plane waves is that an arbitrary field distribution on a plane can be expanded in terms of summation of plane waves coming from different directions. This concept is usually referred to as the plane wave spectrum [17]. An important property of a plane wave is that there are no fields in the direction of propagation. That is, assuming that the direction of propagation is $\hat{z}$, $E_z = 0$ and $H_z = 0$. A wave having no electric field in the direction of propagation is known as a transverse electric wave (TE). If there is no magnetic field in the direction of propagation, the wave is considered transverse magnetic (TM). Therefore, a plane wave is a TEM wave (satisfying both TE and TM requirements).

In regards to this research, we model the wave propagation as TEM, with respect to $\hat{z}$[2]. Therefore, we may write the solution as

$$\mathbf{E} = \boldsymbol{E}_{\boldsymbol{o}}^{+} e^{-j\gamma z} + \boldsymbol{E}_{\boldsymbol{o}}^{-} e^{+j\gamma z} \tag{2.9}$$

where the two terms on the right hand side represent the forward and backward traveling waves respectively, and $\boldsymbol{E}_{\boldsymbol{o}}^{+}$ and $\boldsymbol{E}_{\boldsymbol{o}}^{-}$ are the respective amplitudes of the electric fields polarized transverse to $\hat{z}$. We note here that the real part of γ affects the phase, and its imaginary part determines the wave attenuation. Through Maxwell's equations and the properties of plane waves, we can establish a relationship between the electric field and magnetic fields, given by

$$\hat{z} \times \boldsymbol{E} = \eta \boldsymbol{H} \tag{2.10}$$

[2] The actual wave propagation will be different than TEM. The TEM is used for simplification. The discrepancy between the TEM model and the actual propagation is addresses in the calibration section of this thesis.

where η is the characteristic impedance of the material, given by[3]

$$\eta = \sqrt{\frac{\mu_o}{\epsilon_o(\epsilon' - j\epsilon'')}}. \tag{2.11}$$

2.2.2 Normal Incidence Reflection at a Boundary

This section will present how plane waves interact at single boundary and in a multi-layered media. We begin the discussion with a statement of the boundary conditions at an interface, followed by how the waves transmit and reflect at this boundary. Using the integral form of (2.2 - 2.5), we can derive how the normal and tangential electric and magnetic fields interact at a boundary. Assuming a wave traveling from a lossy dielectric medium 1 into another dielectric medium 2, shown in Figure 2.2, the boundary equations are given by

$$\hat{n} \cdot (\epsilon_1 \boldsymbol{E_1} - \epsilon_2 \boldsymbol{E_2}) = \rho_s \tag{2.12}$$

$$\hat{n} \cdot (\mu_1 \boldsymbol{H_1} - \mu_2 \boldsymbol{H_2}) = 0 \tag{2.13}$$

$$\hat{n} \times (\boldsymbol{E_1} - \boldsymbol{E_2}) = 0 \tag{2.14}$$

$$\hat{n} \times (\boldsymbol{H_1} - \boldsymbol{H_2}) = \boldsymbol{J_s} \tag{2.15}$$

where $\hat{n}$ is the normal vector to the boundary surface pointing from medium 2 to medium 1, and ρ_s and $\boldsymbol{J_s}$ are the surface charge and surface current density, respectively. Assuming we have a plane wave with normal incidence to the boundary, $\boldsymbol{E_i}$, we assume we will also have a reflected wave, $\boldsymbol{E_r}$, in medium 1 and a transmitted wave, $\boldsymbol{E_t}$, in medium 2. By invoking our boundary conditions we find that the tangential electric and magnetic fields are continuous across the boundaries. That is, these conditions yield

[3] For simplicity, we are now using ϵ'' instead of ϵ''_{eff}.

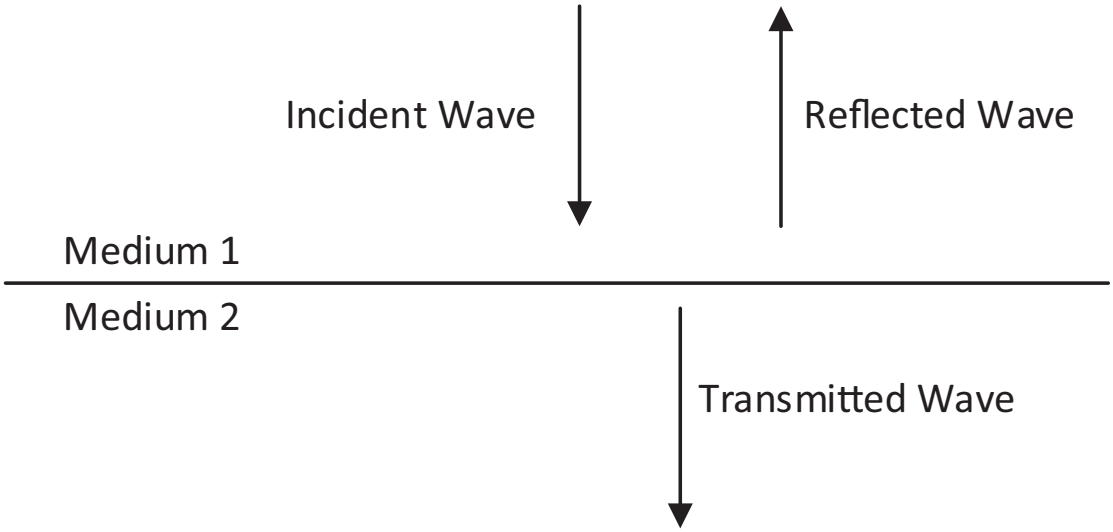

Fig. 2.2: The reflection and transmission of an incident electromagnetic wave at a boundary.

$$\boldsymbol{E_i} + \boldsymbol{E_r} = \boldsymbol{E_t} \tag{2.16}$$

and by (2.10), the boundary conditions for the tangential magnetic fields yield

$$\frac{\boldsymbol{E_i}}{\eta_1} - \frac{\boldsymbol{E_r}}{\eta_1} = \frac{\boldsymbol{E_t}}{\eta_2}. \tag{2.17}$$

From these equations we can establish the following relationships between the incident, reflected, and transmitted waves

$$E_r = \left(\frac{\eta_2 - \eta_1}{\eta_1 + \eta_2}\right) E_i = \Gamma E_i \tag{2.18}$$

$$E_t = \left(\frac{2\eta_2}{\eta_1 + \eta_2}\right) E_i = T E_i \tag{2.19}$$

$$1 + \Gamma = T \tag{2.20}$$

where we define the Fresnel reflection coefficient, Γ, and the Fresnel transmission coefficient, T, for normally incident TE waves [18]. Furthermore, in a multi-layered medium, having more than a single boundary, the reflection at a boundary includes additional sub-

surface reflections as well as the initial layer reflection. The combination of the Fresnel reflection coefficient and subsequent reflections is known as the generalized Fresnel reflection coefficient, $\widetilde{\Gamma}$. In [18], the author derives a recursive equation to find $\widetilde{\Gamma}$ at a boundary when subjected to TE waves. This equation is given by

$$\widetilde{\Gamma}_{i,i+1} = \frac{\Gamma_{i,i+1} + \widetilde{\Gamma}_{i+1,i+2} e^{-2j\gamma_{i+1} l_{i+1}}}{1 + \Gamma_{i,i+1} \widetilde{\Gamma}_{i+1,i+2} e^{-2j\gamma_{i+1} l_{i+1}}} \tag{2.21}$$

where $\widetilde{\Gamma}_{i,i+1}$ is the generalized Fresnel reflection coefficient at the boundary of a layer, i, and the subsequent layer, $i+1$, $\Gamma_{i,i+1}$ is the Fresnel reflection coefficient at the boundary, γ_{i+1} is defined by (2.7), and l_{i+1} is the thickness of layer $i+1$. In order to use this equation we must know the total reflection at the bottom boundary. In our application, the last layer is either ocean which can be considered as a half space, or it is a layer of sea ice which can be modeled as a half space since the most of the energy does not reflect back due to limited penetration depth and wave attenuation. Therefore, the reflection at the interface of the last boundary is modeled by its corresponding Fresnel reflection coefficient. This completes the discussion on how plane waves interact in a non-magnetic lossy multi-layered medium consisting of homogeneous layers. Finally, we note that an antenna can be used to create incident electromagnetic fields. As will be discussed in the next chapter, we use an open-ended waveguide antenna to irradiate the domain of interest.

2.2.3 Dielectric Mixing Models

This section discusses the empirical models used in relating salinity and temperature to the complex permittivity of sea water and sea ice.[4] Bulk sea water is composed of pure water, inorganic salts, and organic matter. The organic matter does not have measurable effects upon the permittivity of sea water [19]. Sea ice is a heterogeneous mixture of liquid brine

[4] The empirical models for dry and wet snow can be found in Appendix A.

inclusions and air pockets within pure ice. The subsequent sections will present the theory and empirical dielectric models of these mediums.

2.2.3.1 Sea Water Empirical Dielectric Model

The empirical dielectric model for sea water used in this thesis is based off of previous models [20]. The new model parameters were interpolated using sea water permittivity data sets collected by Ellison (1996, 1997, and 2003) and Stogryn (1996) [19, 21, 22, 23]. The complex permittivity of sea water is a function of frequency (GHz), temperature ($^{\circ}C$), and salinity (psu) given by:

$$\begin{aligned}\epsilon_w(f,T,S) =& \frac{\epsilon_{ws}(T,S)-\epsilon_{w1}(T,S)}{1-j2\pi f\tau_{w1}(T,S)} + \frac{\epsilon_{w1}(T,S)-\epsilon_{w\infty}(T,S)}{1-j2\pi f\tau_{w2}(T,S)} \\ &+ \epsilon_{\infty}(T,S) + j\frac{\sigma_i}{2\pi\epsilon_0 f},\end{aligned} \tag{2.22}$$

where ϵ_0 is the permittivity of free space, ϵ_{ws} is the static permittivity, ϵ_{∞} is considered as a fitting parameter, f is the frequency, τ is the relaxation time constants of the polar molecules, σ_i is the ionic conductivity, and S is the salinity. Figure 2.3 shows the complex permittivity of pure water and sea water based on (2.22).

The relaxation time constant relates to a frequency dependent phenomenon where the dielectric loss increases due to dipole relaxation [24]. Dipole relaxation time is the time delay in molecular polarization with respect to a changing electric field. The polar molecules are unable to reach equilibrium (re-orientate) as frequency increases. This inability results in higher losses due to the molecules rotating against the electric field. However, the losses caused by polarization decrease as frequency further increases due to molecules not having enough time to even begin to rotate.

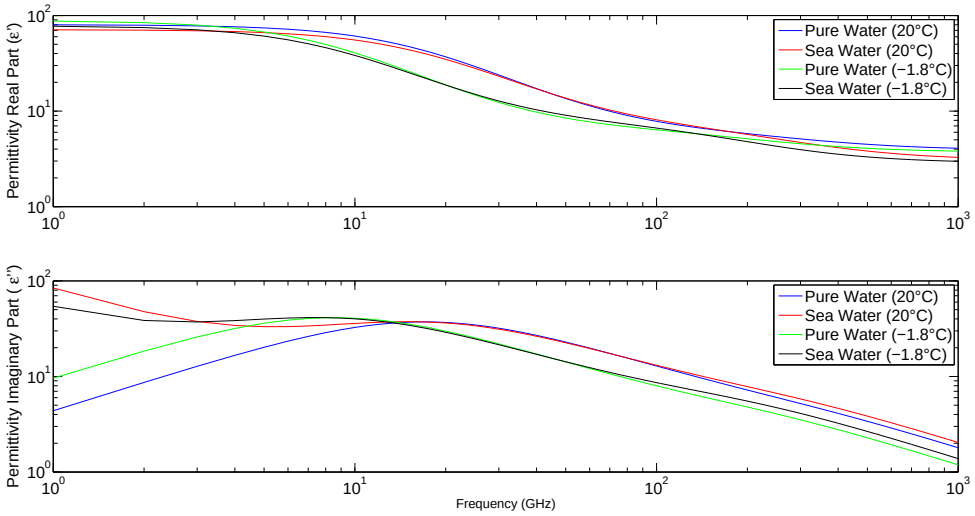

Fig. 2.3: The complex permittivity of pure water and sea water based on the dielectric mixing model. The salinity of the sea water was 32.54 psu.

2.2.3.2 Sea Ice Empirical Dielectric Model

The model used in computing the complex permittivity of sea ice, ϵ_{si}, is a function of the following parameters:

- Complex permittivity of pure ice, ϵ_i.
- Complex permittivity of brine inclusions, ϵ_b.
- Brine volume fraction, v_b.
- The shape and orientation of the brine inclusions.

In addition, ϵ_{si} is a function of the ice temperature T and the ice salinity S_i. The Polder-van Santen/de Loor formulas are used to determine the effective permittivity of the sea ice based on the brine inclusions' shape [14]. The inclusion shapes considered are circular disc, spherical, and needles; the orientation is assumed random. The resulting complex effective

permittivity is based on the host material and the inclusion material where the equations are [14]:

$$\epsilon_{si} = \epsilon_i + \frac{v_b}{3}(\epsilon_b - \epsilon_i)\left(2 + \frac{\epsilon^\star}{\epsilon_b}\right) \quad \text{(Circular Disc)}, \tag{2.23a}$$

$$\epsilon_{si} = \epsilon_i + 3v_b\epsilon^\star\frac{\epsilon_b - \epsilon_i}{\epsilon_b + 2\epsilon^\star} \quad \text{(Spherical)}, \tag{2.23b}$$

$$\epsilon_{si} = \epsilon_i + v_b\frac{(\epsilon_b - \epsilon_i)(5\epsilon^\star + \epsilon_b)}{3(\epsilon_b + \epsilon^\star)} \quad \text{(Needle)}, \tag{2.23c}$$

where $\epsilon^\star$ is an effective permittivity for the region surrounding an inclusion. Pure ice, ϵ_i, is assumed the host material and ϵ_b represents the brine inclusions. If the inclusion volume fraction is small(≤ 0.1), we assume $\epsilon^\star = \epsilon_i$. If the volume fraction of the inclusions is larger, the model assumes $\epsilon^\star = \epsilon_{si}$. The empirical formulas for ϵ_i, ϵ_b, and v_b can be found in Appendix A.

2.3 Geophysical Inversion

Geophysical inversion is a large field of study, with many proven measurement techniques and reconstruction methods. In this thesis, we investigate the use of electromagnetic inversion where we collect S_{11} measurements via an antenna operating at multiple frequencies. This section begins with a discussion on the fundamentals of geophysical inversion, which includes model parameters and the forward solver, under/over/mixed-determined problems, cost function, and derivative-based inversion. We will then discuss the advantage of global optimization for our research; simulated annealing was the global optimization technique chosen. The quality of the data, the complexity of the model, and the end use of the solution are important factors to consider when determining a suitable method (in our case, simulated

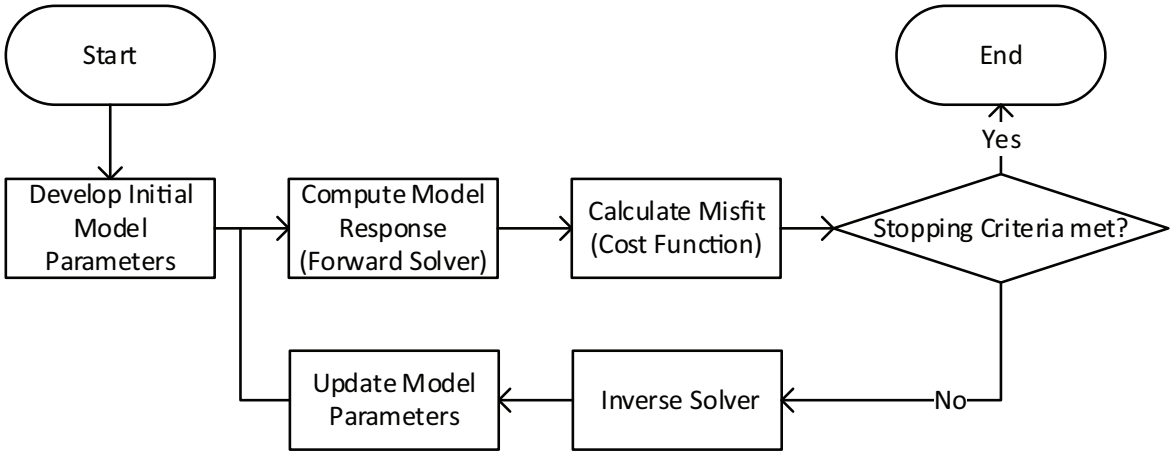

Fig. 2.4: A flowchart demonstrating the steps to solving a general inverse problem [3].

annealing algorithm).

Before proceeding, it is important to note that inversion typically is an iterative process with several iterations. A general flow chart of an inverse problem is shown in Figure 2.4. Initially, we outline our model parameters, which are the properties we are trying to obtain. Next, we use a model to relate these parameters to observed data. In an iterative process, a misfit (or error) is calculated based on the model prediction and observed data. The algorithm terminates if the error is below a predetermined threshold or if a maximum number of iterations is achieved. If the error is high, an inverse solver is used to calculate new model parameters and the iterative process continues. In the following subsections, we will discuss Figure 2.4 in more detail.

2.3.1 Data, Model Parameters, and the Forward Solver

In the geophysical/electromagnetic inversion, we typically solve a nonlinear inverse problem[5] in order to determine the electrical and geophysical properties of the material. The

[5] In electromagnetics, broadly speaking, we have two types of inverse problems: inverse scattering and inverse source. In electromagnetic inverse scattering, the goal is to find some properties (*e.g.*, permittivity, permeability, etc) of the investigation domain by irradiating the investigation domain and measuring the result-

first step in solving an inverse problem is identifying the unknowns and establishing a relationship between them and the observed data. With respect to Figure 2.4, the electrical and geophysical properties are the unknown model parameters, χ, and the microwave imaging measurements collected are the observed data, $\mathbf{d}$. Assuming we know the true model parameters, $\chi^{\mathbf{t}}$, to the measured data, we can formulate equations connecting the two, given by

$$\begin{bmatrix} d_1 \\ d_2 \\ \vdots \\ d_n \end{bmatrix} = \begin{bmatrix} G_1(\chi_1^t, \chi_2^t, \ldots, \chi_m^t) \\ G_2(\chi_1^t, \chi_2^t, \ldots, \chi_m^t) \\ \vdots \\ G_n(\chi_1^t, \chi_2^t, \ldots, \chi_m^t) \end{bmatrix}, \tag{2.24}$$

where n is the number of measured data, m is the number of model parameters, and $\mathbf{G}$ is a set of either linear or non-linear functions; $\mathbf{G}$ is our forward solver operator in Figure 2.4. The purpose of the forward solver is to compute a response, $d^\star$, based on the current model parameter prediction, χ, given by:

$$\mathbf{d}^\star = \mathbf{G}(\chi) \tag{2.25}$$

This response will then be compared to the observed data, which will be discussed in Section 2.3.3. The relationship between the number of model parameters and observed data is important when identifying suitable inversion techniques. If $\mathbf{G}$ is a set of independent functions and $n < m$, the inversion problem is considered under-determined [25]. This means there are more unknown model parameters than known measurements. If $\mathbf{G}$ is a set of independent functions and $n > m$, the inversion problem is considered over-determined; there is more data than model parameters. The third type of problem is mixed-determined [26]. Mixed-determined problems occur when a portion of the model parameters are under-determined and the rest are over-determined. This can occur when either the model, or the

ing external fields. In electromagnetic inverse source problems, a radiator is located inside the investigation domain, and the goal is to characterize this radiator (*e.g.*, through its equivalent current distribution) from the measurement of its fields outside the investigation domain [4].

measurement technique does not properly interrogate some of the model parameters or if $\mathbf{G}$ is rank deficient.

Typically in a mixed-determined problem, the sensitivity of the data to some model parameters are too low to be able to resolve them. For example, in seismic tomography you cannot resolve the mantle layers using only surface waves; these waves do not penetrate into the mantle layers [27]. Therefore, no information is obtained for these layers. One way to analyze the sensitivity of each parameter is to take the partial derivative of $\mathbf{G}$ with respect to each model parameter. This matrix of partial derivatives is called the Jacobian matrix or sensitivity matrix, given below:

$$\mathbf{J} = \begin{bmatrix} \frac{\partial G_1}{\partial \chi_1} & \cdots & \frac{\partial G_1}{\partial \chi_m} \\ \vdots & \ddots & \vdots \\ \frac{\partial G_n}{\partial \chi_1} & \cdots & \frac{\partial G_n}{\partial \chi_m}. \end{bmatrix} \tag{2.26}$$

In the following sections we will discuss some common challenges of inversion, before proceeding to global optimization techniques.

2.3.2 Common Challenges with Inverse Problems

Inverse problems are inherently difficult to solve due to common issues which include solution existence, solution uniqueness, and instability [25]. These three issues influence the quality, interpretation, and usefulness of the solution. This section will explain these three challenges and how they relate to geophysical inversion.

To begin, solution existence refers to there being no model that exactly maps a set of model parameters to the observed data. This is due to the mathematical model not matching the true

physics of the system. That is, the $\mathbf{G}$ used in the forward solver is either a bad approximation of the actual (true) $\mathbf{G}$, or is incorrect. Usually, approximations are made due to the inability to model the exact physics, and/or to reduce computation time of the forward solver. In addition to approximate mathematical models, data noise also affects solution existence. For this thesis, we assume our data has Gaussian noise, based on the Central Limit Theorem for random variables [28].

The next issue is solution uniqueness, which refers to there being more than one set of χ that exactly satisfies (2.25). For example, rank deficiency in $\mathbf{G}$, say due to lack of sufficient measured data, leads to a nontrivial null space, which can then result in having non-unique solutions. In addition, non-uniqueness of a problem can be due to some model parameters that barely affect the measured data.

Finally, solution instability occurs when small changes in the measurements lead to a large change in the estimated model. When this situation occurs, the problem becomes unstable. For example, when the matrix $\mathbf{G}$ is ill-conditioned, a small change in $\mathbf{d}^\star$ may correspond to a significant change in χ.

2.3.3 Cost Function

After establishing the relationship of our model parameters and model, we can now look at the steps necessary for reconstructing χ^t. We begin with the cost function which, for each iteration of our inversion, quantifies the error between our predicted model response and observed data. The general cost function used in this thesis is an Euclidean norm (L^2-norm) given by

$$C = ||\mathbf{d} - \mathbf{d}^\star||_2^2 = \sum_{i=1}^{n} |d_i - d_i^\star|^2, \tag{2.27}$$

where $\mathbf{d}$ is our measured data, and $\mathbf{d}^\star$ is the model response to a predicted set of model parameters. As can be see, the cost function C is a mapping from an m dimensional space (number of unknowns) to a real number. The L^2-norm given in (2.27) can be normalized in order to prevent some subset of $\mathbf{d}$ dominating the total error; this new cost function is given below:

$$C = \sum_{i=1}^{n} \frac{|d_i - d_i^\star|^2}{|d_i|^2}. \tag{2.28}$$

We can further enhance our cost function by introducing a weighting factor, $\mathbf{W}$, given by [29]:

$$C = \sum_{i=1}^{n} W_i \cdot \frac{|d_i - d_i^\star|^2}{|d_i|^2}. \tag{2.29}$$

This set of weights gives specific, rather than random, subsets of $\mathbf{d}$ a more dominant role in the overall cost (error). The selection of a weight function is based on the understanding of the data, model, and model parameters. In other words, the use of $\mathbf{W}$ requires some form of prior information about the measured data; *e.g.*, having some more accurate sensors in a multiple-sensor measurement system.

2.3.4 Derivative-Based versus Global Optimization

The final block to discuss in Figure 2.4 is the inversion algorithm. Algorithms rely on finding either the global minimum or maximum of the cost function. Therefore, we begin with the general form for optimization of a cost function. Given a function, C, and a set $S \subseteq \mathbb{R}^m$, called the feasible region [30], an optimization problem is given by

$$\min_{\chi \in S} C(\chi) \tag{2.30}$$

where we are minimizing C with respect to a combination of model parameters, χ. Within S there exists a specific set of modeling parameters, χ^g, such that

$$C(\chi^g) \leq C(\chi) \quad \forall \chi \in S. \tag{2.31}$$

This means, that there exists a specific set of model parameters that produce a value, given by $C(\chi^g)$, that is the minimum value produced by the function, C, in the feasibility region (search space), S. The way in which C is minimized is highly reliant on the shape of the search space. This is primarily due to some algorithms finding local minima rather than the global minimum.

When $\mathbf{C}$ is convex cost function in S, derivative-based optimization techniques will find the global minimum. For example, in the steepest descent method, the algorithm follows the direction of the negative gradient of $\mathbf{C}$ with respect to χ. As a result, this can lead to a non-optimal solution (a local minimum) if the search space is non-convex. That's why these derivative-based techniques depend heavily on the initial selection of χ (initial guess) when solving non-convex inverse problems. An example of the importance of an initial guess is shown in Figure 2.5, where we have a non-convex search space. Assuming a steepest descent method, the initial parameter selection at State *A* leads to solution *B* whereas if the initial guess was State *D*, the solution will be *C*. These types of methods can still be used in non-convex problems by utilizing appropriate prior information, regularization, or kernels. For our example, with prior information, the search space could be reduced to a convex search space located around State *C*.

However, with a highly non-convex $C(\chi)$, it is not always possible to reduce to a convex search space. As well, sometimes it is difficult or computationally expensive to solve for the partial derivatives of the cost function. In regards to this research , we choose the global optimization approach since our cost function is highly nonlinear and would require a very

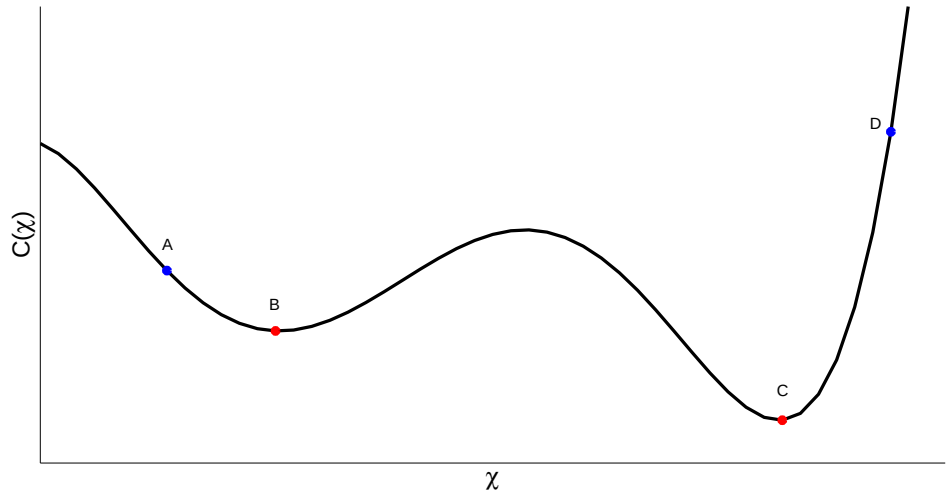

Fig. 2.5: A sample search space with non-convex features. Strictly derivative-based optimization will approach different local minima depending on the initial state of χ. State A will converge to a local minimum at B, whereas State D would approach the global minimum at C.

complex model.

Global optimization algorithms, which do not require computing the derivatives of $\mathbf{C}$ with respect to χ, are effective when the search space has many local minima. Global optimization techniques avoid stagnation by implementing non-deterministic algorithms. To this end, these methods employ randomness and probabilistic approaches when determining a new state of χ. A very basic global optimization algorithm is the Monte Carlo method in which χ are chosen randomly for every iteration [31]. Some more complex methods include simulated annealing [32], genetic algorithms [33], and particle swarm optimization [34]. Simulated annealing was the global optimization method chosen for this research.

Finally, we note that derivative-based optimization approaches often converge faster than global optimization; there are fewer iterations in derivative-based optimization. To this end, global optimization can sometimes be too computationally expensive. Therefore, it is important to use a fast forward solver in order to keep the method viable. In our case, we use a recursive forward solver that is still relatively fast.

2.3.5 Simulated Annealing

Annealing refers to the heating of a solid to a high temperature in which all particles of the solid randomly arrange themselves in a liquid phase, followed by slowly cooling the liquid back into a solid [35]. At the maximum temperature, the particles within the material can move freely and have a high energy state. As the liquid cools, the atoms' movement lessens until the material reaches a low energy crystalline lattice structure [32]. If the cooling process is too fast, the material may solidify into an amorphous structure with a high energy state. Simulated annealing is analogous to annealing of a solid.

Simulated annealing is a global optimization algorithm that is mainly used in combinatorial problems. However, they have been shown to work with continuous variables [36]. In theory, simulated annealing will always converge to the global minimum if allowed to run for infinite iterations. For each iteration the algorithm uses a probability factor, called the Boltzmann constant, to determine whether a worse configuration of χ will be kept. The algorithm will always accept a new χ if the cost function value is lower than the previous iteration.

As the system cools, this probability of accepting a worse solution decreases. Hence, initially the algorithm will have a high probability of choosing a worse solution than the current best solution. It is this process that allows simulated annealing to "jump" out of local minima. The mathematical relationship between the system temperature and the Boltzmann constant will be discussed in Section 2.3.5.1.

We begin with a general flowchart for simulated annealing, shown in Figure 2.6. The algorithm starts at a maximum temperature T_s and slowly decreases until it reaches a set minimum temperature, T_f. The number of temperatures is denoted by N_{max}. The way in which the temperature changes will be referred to as the cooling schedule. This schedule

can be linear, logarithmic, exponential, or any other function (not necessarily decreasing at every step). At each temperature, the algorithm runs for a set number of iterations, L_{max}, which emulates the process of reaching thermal equilibrium. The energy at each iteration is determined by the cost function. The way in which the model parameters are perturbed will be presented in a later subsection. Sometimes, multiple heating and cooling of the algorithm leads to a better performance. With respect to Figure 2.6, a reset counter, R_{max}, can be implemented to control the number of cooling cycles.

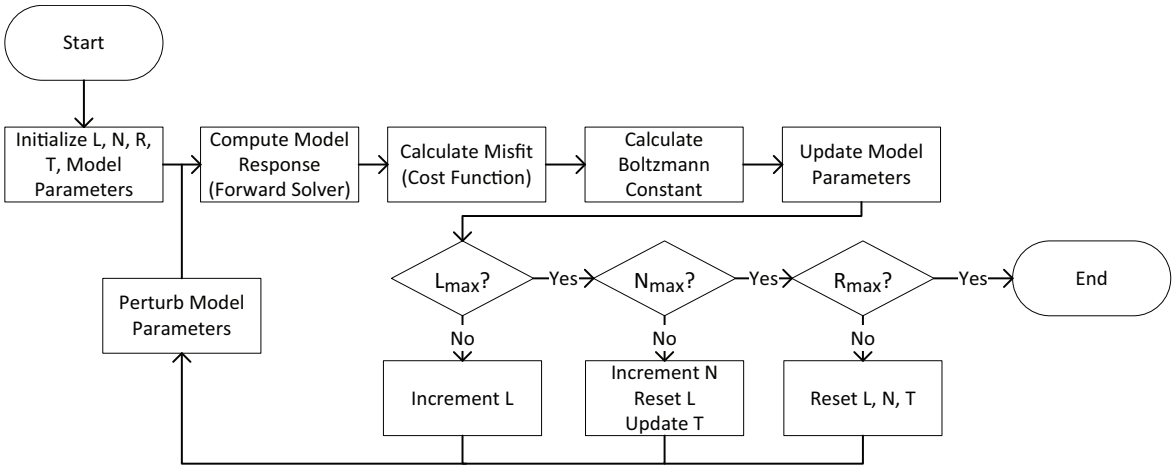

Fig. 2.6: Flow chart of a general inverse problem using the simulated annealing algorithm.

2.3.5.1 Boltzmann constant

This section will present the mathematical relationship using which the Boltzmann constant, P, is obtained. Following, we will discuss how the Boltzmann constant is used in the decision making of the algorithm. To begin, the equation determining P is given by

$$P = e^{\frac{-\Delta E}{\Delta E_{avg} T}} \tag{2.32}$$

where ΔE is the difference between the cost function value of the current iteration and the previously accepted one. In addition, T is the current temperature, and ΔE_{avg} is a running

average of the previously accepted cost function values.

For each iteration, a random number is generated between 0 and 1, which is then compared to P. If P is greater than this number, the algorithm will accept the current χ as the new configuration heading into the next iteration. We note here that if the new cost function value is lower than the previous iteration, the algorithm will accept the new χ without having to calculate the Boltzmann constant.

The value of P will be between 0 and 1, initially having higher values at the start of the algorithm. If we look at (2.32), as T decreases, the average trend of P will also decrease. This causes a decrease in the probability of the Boltzmann constant being higher than the random number generated as the algorithm progresses. The following section will describe the way in which the cooling schedule is determined.

2.3.5.2 Cooling Schedule

The cooling schedule of the algorithm is very important in solving global optimization problems accurately and time efficiently. The algorithm may not converge or may become stagnant if the schedule is not tuned to the problem. That is, the schedule may cool too fast or too slowly, or not cool sufficiently. With respect to the probabilistic nature of simulated annealing, the probability of choosing a worse solution may be too high or too low. The algorithm starts at an initial temperature T_s and finishes at a temperature T_f. T_s and T_f are determined by:

$$T_s = \frac{-1}{\ln P_s} \tag{2.33}$$

$$T_f = \frac{-1}{\ln P_f} \tag{2.34}$$

where P_s and P_f are the starting and finishing probability that a configuration with a higher cost value will be accepted. After establishing the relationship between temperature and the Boltzmann constant, we now discuss how the algorithm varies temperature. As previously stated, the cooling schedule is customizable to the given problem. For this thesis, the temperature change is given by

$$T_{new} = T_{prev} \cdot F \tag{2.35}$$

where T_{new} is the new temperature, T_{prev} is the previous temperature, and F is the cooling schedule function, given by [37]

$$F = (\frac{T_f}{T_s})^{\frac{1}{N-1}} \tag{2.36}$$

where N is the number of temperature changes. We have now established the cooling schedule of simulated annealing and how it can be used to navigate within a search space. The next section will describe how to generate new potential solutions of χ using different perturbation techniques.

2.3.5.3 Perturbation Techniques

In a stochastic optimization scheme, there exist various ways in which χ can be updated (perturbed). At the root of each method there exists an element of randomness. The simplest perturbation technique is the Monte Carlo method, where the model parameters are updated completely at random. This type of approach is typically only practical when the search space is sufficiently small or no other information is available. Otherwise the number of iterations required to find a reasonable solution would be too large. In turn, this would require too many calls to the utilized forward solver.

We can refine a completely random approach by introducing constraints and prior information. Some examples of these include subsets of model parameter partial derivatives, loose

relationships between model parameters[6], small perturbations from current χ, and knowledge of time series trends[7].

In simulated annealing, the cooling schedule can be used to implement adaptive perturbation methods. That is, the current temperature affects the amount of perturbation of specific model parameters. For example, as the temperature approaches T_f the amount of perturbation could decrease. A benefit of an adaptive method is the reduction in the search space as the likelihood of choosing a worse solution decreases. This could potentially eliminate unnecessary iterations. Overall, the random element in global optimization techniques is what allows these methods to avoid getting trapped in local minima.

[6] For example, in a first-year ice, salinity follows a C-shape trend with a the top and bottom layers being more saline than the middle layer.

[7] For example, electromagnetic measurements from the sea ice domain of interest can be taken in a time series fashion. This way, we know the probability of the unknown parameters exceeding a certain range between two successive close time steps is low.

3

Antenna Design

As noted earlier, the proposed approach that we are investigating is an active remote sensing approach in which the region of interest (in our case, sea ice) is irradiated by electromagnetic fields. The device that irradiates the region of interest is an antenna, which is the topic of this chapter.

This chapter presents the placement, design, fabrication, and verification of the antenna utilized in this research. A surface contacting open-ended waveguide was chosen due to its relatively wideband properties and robustness to the harsh Arctic climate. After fabrication, the antenna's near-field distribution and far field pattern were measured using a spherical near-field system and a compact antenna test range, respectively. In addition, we studied the S_{11} and the vector network analyzer (VNA) calibration with respect to varying temperature.

3.1 Antenna Placement

The placement of the apparatus was the first consideration in the antenna selection. The four choices include above, surface contacting, embedded inside, or underneath the ice. We opted for a surface based sensor mainly due to practical reasons. For example, under ice approaches can be expensive and difficult to position the sensor. Airborne or satellite sensors are also expensive and may not provide high temporal resolution that is required for certain applications. Surface based sensors benefit from allowing necessary temporal resolution and typically are not as costly as the other approaches. In relation to temporal resolution, in [6], the surface remote sensing has been recommended for oil spill detection in the Arctic when the oil is under or in ice.

A challenge with above-the-surface techniques is that the irradiating electromagnetic waves (in our case, microwaves) interact and are affected by the roughness parameters of the snow (ice)-air interface. From the inversion algorithm point of view, these roughness parameters will then be additional unknown model parameters, see (2.24), for the utilized inversion algorithm. Due to the lack of measurement data in a practical data collection scenario, it is often a good idea to minimize the number of unknowns.[1] In the proposed surface contacting approach, we speculate that we do not need to incorporate the roughness parameters into the inversion algorithm as the electromagnetic waves are directly coupled into the medium. This can be a potential advantage for this approach. We also note that we utilize this antenna in the monostatic configuration. That is, the same antenna is used for both transmit and receive. Finally, it should be noted that another potential advantage for the surface contacting approach is that multiple antennas can be placed in different parts of the domain of interest to create a sensor network monitoring the domain. Finally, to the best of our knowledge, this

[1] One way to handle this in the above-the-surface technique is to provide this roughness parameters to the inversion algorithm as prior information, which may then require the use of a new apparatus: Lidar.

approach (the specific combination of data collection, data calibration, and data processing as will be explained) has not been investigated for this problem before, and therefore deserves investigation.

Certain challenges are associated with designing a surface contacting antenna, primarily the coupling between the antenna and snow-covered sea ice. Most antennas are designed and optimized to radiate into free space. When an object (scatterer) is introduced in an antenna's far-field (FF) zone, it does not load the antenna; *i.e.*, the radiation properties of the antenna are not affected. On the other hand, when an object is introduced in an antenna's near-field (NF) zone, the radiation properties of the antenna and its impedance will change. (For example, in microstrip antenna design, a dielectric layer or multiple layers called superstrate(s) can be placed in the NF zone of the antenna to increase its gain [38].) In essence, this object now becomes part of the antenna. The proximity of snow and sea ice will affect the overall performance of the antenna such as bandwidth, penetration depth, NF distribution and gain. The following sections will discuss the need for multi-frequency measurements and potential antennas for the proposed application.

3.2 Operating Frequency Selection

The purpose of this antenna is to collect the S_{11} that will be used in a global optimization algorithm to reconstruct the thickness and complex permittivity of the snow-covered sea ice. A sufficient amount of independent data must be collected in order to reconstruct this profile. Independent data can be acquired by having measurements of different angular views, frequencies, and electric field directions (polarizations[2]). Herein, we opt for a multiple frequency approach since this approach does not require mechanical repositioning of the

[2] We note that "polarization" is a FF property; since the antenna operates in its near-field, we have used electric field directions instead of polarization.

antenna. In addition, if the antenna polarization changes, the antenna will "see" a different property if the dielectric properties of the snow-covered sea ice are not isotropic. Mathematically, this results in having a tensor unknown for the dielectric properties, thus, increasing the number of unknown model parameters.

A wide frequency range is necessary in order to obtain independent measurements. There is not enough new information added from each frequency if the frequency range is too narrow. If the bandwidth is too narrow, mathematically, this translates into having G_1 to G_n given in (2.24) converging to a single G, thus, resulting in having one equation and multiple unknown model parameters. With this in mind, the frequency range of interest for this research was chosen to be from 3 GHz to 5 GHz. We speculate this frequency range will give sufficient penetration depth and layer resolution. Finally, it should be noted even if get sufficiently independent G_1 and G_n through the use of this frequency bandwidth, that does not mean that the same reconstruction accuracy for χ_1 to χ_m can be achieved. This is due to the fact that the sensitivity (Jacobian) of the measured data (d_1 to d_n) to different model parameters (χ_1 to χ_m), *i.e.*, $\partial d_i/\partial \chi_j$, is dependent on the penetration depth, which itself is frequency-dependent. For example, the entire frequency bandwidth can irradiate the top layer; however, the higher end of the frequency bandwidth may not sufficiently irradiate the bottom layer, thus, the sensitivity with respect to the bottom layer properties will suffer.

In addition, this range was chosen due to the lack of previous Arctic microwave remote sensing studies done on snow-covered sea ice in this bandwidth within the Centre for Earth Observation Science at the University of Manitoba. (We have a C-band scatterometer at the University of Manitoba which operates at 5.5 GHz with a narrow bandwidth.) Below 3 GHz, ground penetrating radars have been utilized to characterize snow-covered sea ice. A recent study designed a GPR system to determine the properties and thicknesses of snow and sea ice using a bistatic system [39]. The frequency range used in this study was 400

MHz to 1.5 GHz and the maximum thicknesses of the snow and sea ice were 20 cm and 50 cm, respectively. Above 5 GHz, ground based scatterometers have been used for this application, an example given in [8]. C-band NRCS measurements were collected using a scatterometer, placed above the sea ice surface on scaffolding. The permittivity profile was then reconstructed from these measurements utilizing an electromagnetic inverse scattering algorithm.

3.3 Antenna Selection

We can look towards selecting a specific type of antenna now that the placement and frequency requirements have been determined. To this end, the selection criteria of the type of antenna was based on the penetration depth, multiple-frequency operation in the presence of lossy dielectrics, cost, and robust to the harsh environment. The two types of antennas evaluated were microstrip and OEW antennas. Basic examples of the two are shown in Figure 3.1. There have been a multitude of free space designs of these antennas over the microwave frequency spectrum.

The penetration depth of the antenna is important since illuminating further into the snow-covered sea ice provides more data. A directive[3] antenna will focus more energy into the layers as opposed to an omnidirectional antenna at the same frequency. Typical wideband patch antennas are bidirectional, with the main beam propagating into the ice and a back beam pointed towards the sky. A reflector can be positioned above the patch antenna to reflect the skyward radiation back towards the sea ice [40]. The reflector must be correctly positioned in order to prevent destructive interference between the two waves. This method may not be appropriate when placed against a lossy dielectric due to the patch's changing

[3] Directivity is a far-field quantity; However, in our application, we are mainly concerned with the NF zone. So the term directivity is loosely used. Perhaps a better word would be focussed.

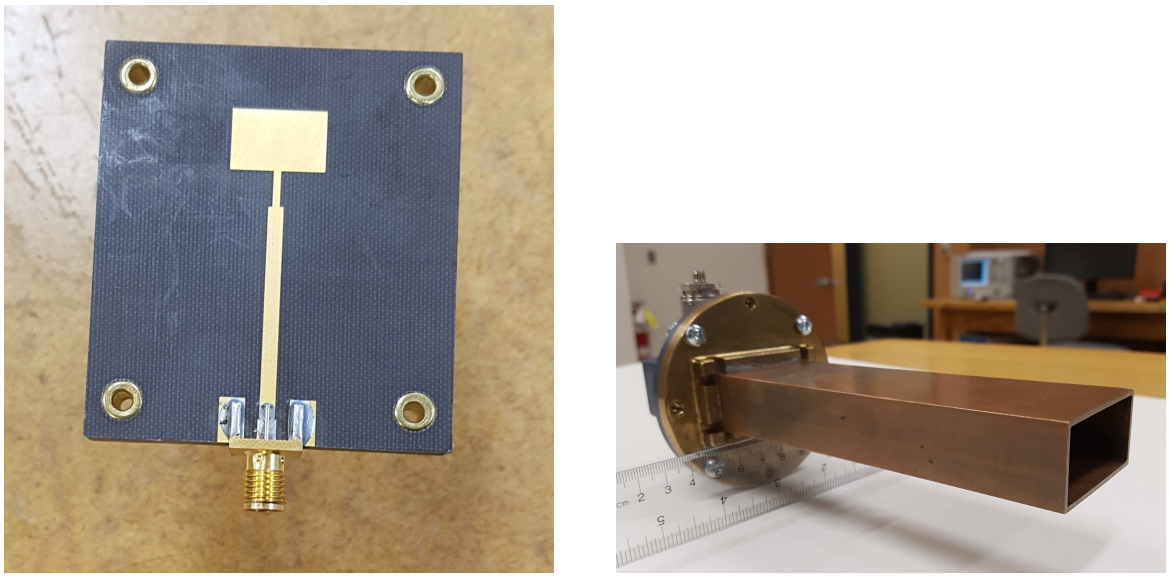

(a) (b)

Fig. 3.1: The two types of antennas to be evaluated; (a) patch antenna and (b) OEW. This specific patch antenna is not wideband.

ϵ_{eff}. On the other hand, an OEW is a directional antenna not requiring any major modifications to its structure. In other words, an OEW automatically provides a good front-to-back ratio (one of the reasons that OEWs are common in planar near-field antenna measurement systems).

Another factor that affects penetration depth is how well the antenna matches with the snow-covered sea ice. With regards to matching a microstrip antenna with snow-covered sea ice, the designer could take a pre-existing antenna that operates in free space and modify some parameters; these parameters include substrate permittivity, substrate thickness, dimensions of the patch, addition of a superstrate layer, or the feed point. The optimization process can be time consuming for an antenna having this many parameters. For an OEW, the inherent mismatch is due to the air/snow boundary at the OEW's aperture. Filling the OEW's cavity with a dielectric having similar characteristics to snow is one method to reduce this boundary reflection. This leaves the largest mismatch to be between the cable and probe feed point. Just like in air-filled waveguides, the position and length of the probe can be optimized to

provide a low mismatch loss. The number of parameters required to be optimized is lower in the OEW than that of the microstrip antenna.

In general, an antenna's bandwidth decreases when in the presence of a material having a permittivity greater than air. Therefore, we should select an antenna that has wideband properties in free space since it is expected to lose bandwidth when placed against a dielectric. Antenna bandwidth for this research is defined as a range of frequencies where the antenna's reflection coefficient, $|S_{11}|$, is less than -10 dB. OEW and modified microstrip antennas both have been shown to have relatively wideband properties in free space. For this research, a relatively wideband is considered to be 2 GHz to 3 GHz wide. We speculate this bandwidth will allow for multi-frequency inversion.

Robustness is the final requirement for the antenna. In the Arctic, the cold and salt can affect the antenna's properties. In regards to the microstrip antenna, the cold can make the substrate brittle and susceptible to cracks in either the substrate or conductor. As well, the abundance of salt in the Arctic corrodes most metals. A method to alleviate some of these problems is to encapsulate the antenna in a protective material. However, this introduces more materials in the antenna's near field resulting in a more complex design. The OEW is believed to be more robust than a microstrip antenna based on the dielectric placed inside protects the radiating probe feed and inner surface of the waveguide, without increasing complexity of the antenna design. In addition, a brass flange can be attached to the OEW in order to provide a solid base for the antenna to stand on.

Based on the above, the OEW presents an appropriate opportunity for achieving a robust, surface contacting antenna capable of irradiating snow-covered sea ice at multiple frequencies of operation. The following sections will present the initial design and optimization of the OEW.

3.4 Initial OEW Design

Based on the discussions in the previous two sections, the goal of this section is to design an antenna to irradiate directly into snow. The values obtained in this section will be a starting point for the HFSS simulations. A rectangular waveguide, rather than cylindrical, was chosen due to convenience and cost, shown in Figure 3.2. The first step in the design

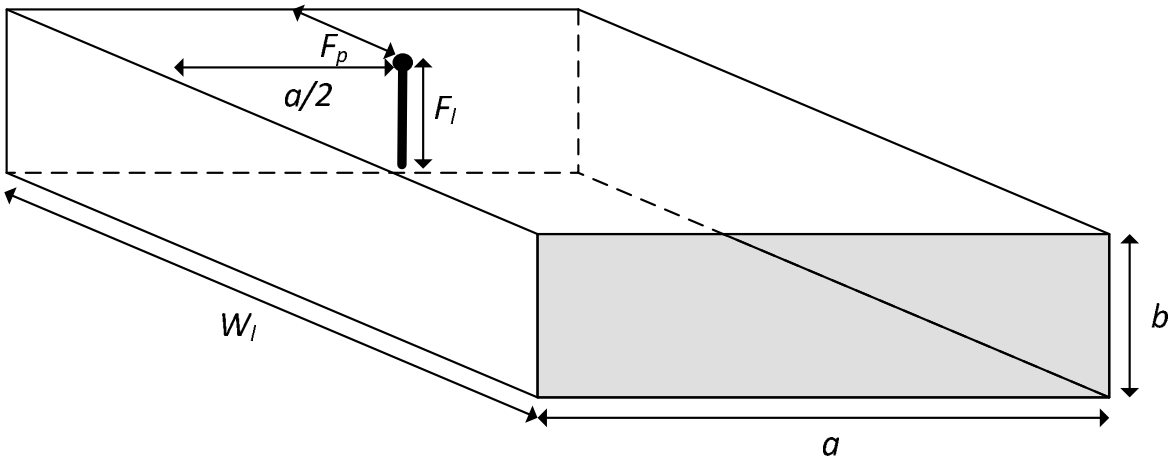

Fig. 3.2: A simple diagram of a probe fed OEW. The gray edge represents the aperture of the antenna and the thick black line represents the probe feed.

was determining the following parameters:

- Waveguide width a, height b, and length W_l.
- Probe feed length F_l.
- Probe feed position F_p from the back plate.
- Dielectric material, ϵ_r, inside the OEW.

Tab. 3.1: Cutoff frequencies of UHMW-filled G-Band OEW within desired bandwidth.

Mode	m	n	f_c (GHz)
TE	1	0	2.08
TE	2	0	4.16
TE	0	1	4.47
TE, TM	1	1	4.93
TE, TM	2	1	6.10

To start, we must choose values of a, b, and ϵ_r to obtain the required operating frequency range. The cutoff frequency for the waveguide's modes can be found as [41]:

$$f_{c_{mn}} = \frac{c}{2\pi\sqrt{\epsilon_r}}\sqrt{\left(\frac{m\pi}{a}\right)^2 + \left(\frac{n\pi}{b}\right)^2}, \tag{3.1}$$

where c is the velocity of light in free space, m and n are the modes (not zero simultaneously), and ϵ_r is the permittivity of the material inside the OEW [42]. Typically, the real part of the permittivity of snow ranges from 1.4 to 3.2 and is dependent on snow density, temperature, and wetness [14]. Therefore, the material chosen was an ultra high molecular weight (UHMW) plastic having a permittivity of 2.3, which is near the center of the snow's permittivity range.

This permittivity lowers the cutoff frequencies of standard waveguide sizes by approximately 1.5 times. A WR187 G-band waveguide ($a = 4.755$ cm and $b = 2.215$ cm)[4] met the frequency requirement and was available in the lab. The cutoff frequencies are given in Table 3.1.

Usually, OEWs are intended to operate only in their fundamental mode, in applications such as wireless communication. This configuration is beneficial when it comes to polarization and linking a transmitter and receiver. However in our application, we are primarily interested in irradiating the snow-covered sea ice; *i.e.*, getting the electromagnetic energy into

[4] In practice, the rectangular wall has a thickness; in that case, a and b represent inner dimensions.

Tab. 3.2: Initial OEW parameters to be used in HFSS simulations.

Parameter	Value
a	4.755 cm
b	2.215 cm
W_l	10 cm
F_l	11.07 mm
F_p	12.4 mm
ϵ_r	2.3

the domain of interest. We may be able to use these higher modes of the OEW if we are able to properly model the physics or use calibration techniques on the measurements. We opt for the latter of the two, which will be discussed in detail in Chapter 6.

The waveguide length dictates whether the modes have enough space to fully develop. The antenna is to have a low profile, so the length of 10 cm was chosen. The rule of thumb when designing the monopole feed into the cavity is $\frac{\lambda}{4}$ away from the back plate. This wavelength was calculated using the center frequency of 4 GHz. The length of the monopole is approximately halfway into the cavity. As well, the monopole is center positioned along the width of the OEW. The importance of these feed values are in minimizing the mismatch between the waveguide and the $50\ \Omega$ coaxial cable. These values are a starting point in the optimization process. Table 3.2 summarizes the initial parameters chosen for this rectangular waveguide.

3.5 HFSS Optimization

The rectangular OEW was modeled in HFSS using the parameters determined in Section 3.4. HFSS is a finite element electromagnetic solver for electromagnetic analysis. This software was used in determining the S_{11}, near-field distribution, and far-field patterns of our antenna.

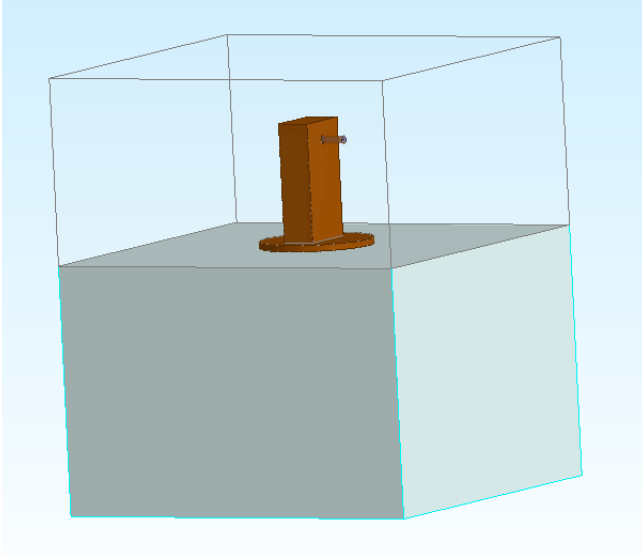

Fig. 3.3: HFSS model rendering of the OEW placed on top of a single snow layer.

Figure 3.3 shows the aperture of the OEW placed flush with a $30x30x20$ cm^3 snow layer. We chose snow having a permittivity of 2.3 and a bulk conductivity of 10^{-8} S/m. The remaining section surrounding the OEW is a $30 \times 30 \times 20$ cm^3 air box. The material outside the boundary of the system was an absorbing boundary condition box. That is, the signals do not reflect at the boundary.

In order to reduce computation time, the snow is modeled as a single-layered isotropic dielectric. Based on Table 3.1, a frequency sweep from 2 GHz to 6 GHz was performed. The S_{11} generated is shown in Figure 3.4. As can be seen, we have 2 bands, located at 3.75 GHz and 4.8 GHz. There is a local maximum between the 3.75 GHz and 4.8 GHz, which is slightly above the desired -10 dB. An attempt can be made to reduce this maximum below -10 dB by changing the parameters outlined in Section 3.4.noting that W_l, a, and b have already been fixed, we optimize $|S_{11}|$ over F_l and F_p.

The parameters F_l and F_p were optimized utilizing HFSS's parametric function. Initially, each parameter was varied above and below the original values, where the combinations are given in Table 3.3. The $|S_{11}|$ for each case are plotted in Figure 3.5.

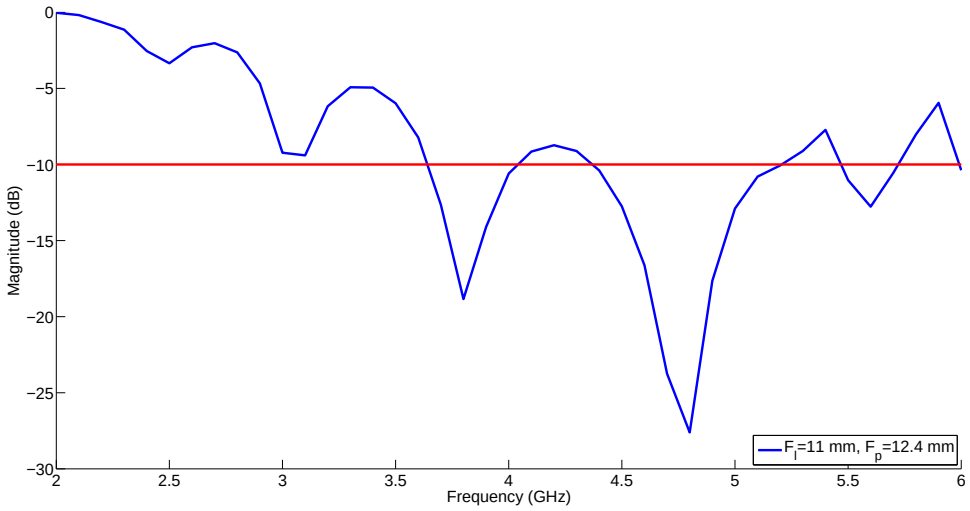

Fig. 3.4: $|S_{11}|$ of the OEW using the initial design parameters. The red line indicates the -10 dB line where any value below it is considered a band of the antenna.

Tab. 3.3: The test parameters used in the initial optimization of the OEW's $|S_{11}|$.

Test Number	F_l (cm)	F_p (mm)	Test Number	F_l (mm)	F_p (mm)
1	10	11.1	6	12	12.4
2	11	11.1	7	10	13.6
3	12	11.1	8	11	13.6
4	10	12.4	9	12	13.6
5	11	12.4			

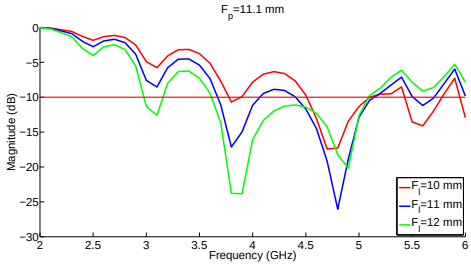

(a) $F_p = 11.1$ mm.

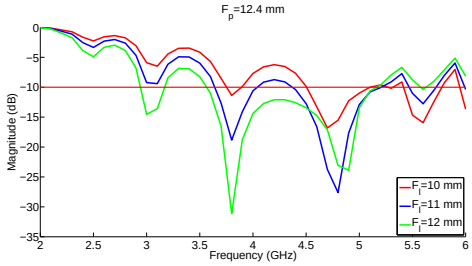

(b) $F_p = 12.4$ mm.

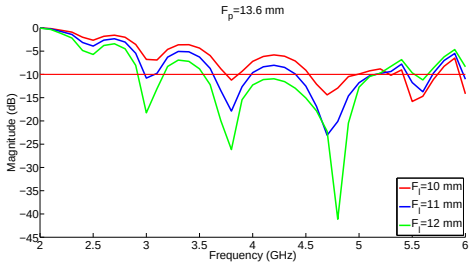

(c) $F_p = 13.6$ mm.

Fig. 3.5: $|S_{11}|$ for different probe feed parameters, given in Table 3.3.

From Figure 3.5(a)-(c), when $F_l = 12$ mm, the magnitude is lower within the desired bandwidth of 3 GHz to 5 GHz. In some cases, particularly in Figure 3.5(a), the magnitude is lower when $F_l = 10$ mm at frequencies above 5 GHz. However, maintaining bandwidth at the lower frequencies will allow for more penetration depth into the snow and sea ice which we think to be more beneficial to this research.

Figure 3.6 shows the $|S_{11}|$ when holding F_l at 12 mm. The bandwidth for each case are relatively similar to each other. The decision was made that $F_p = 13.6$ mm was an appropriate choice based on the slightly higher bandwidth, and the narrower peak between 3.75 GHz and 4.75 GHz.

There were a total of 15 subsequent tests performed, which the values are given in Table 3.4. Figure 3.7 presents the $|S_{11}|$ of a few of the trials. From these tests, test number 2 was selected as the final design. This test provided a more consistently low $|S_{11}|$ across the bandwidth. Specifically, the local maximum at 4.2 GHz was the lowest out of the tests. Table

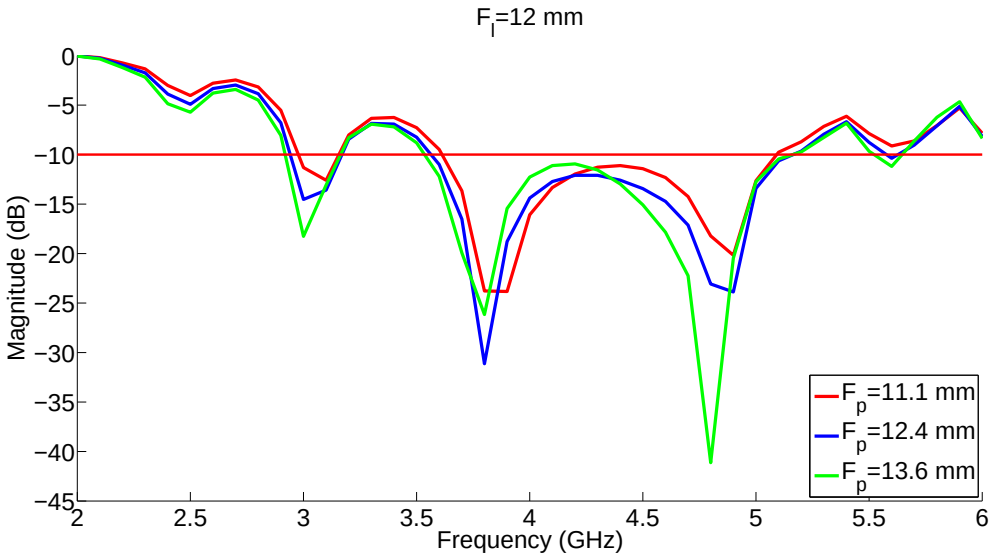

Fig. 3.6: S_{11} of the OEW when holding F_l constant (12 mm) and varying F_p.

Tab. 3.4: The test parameters used in the final optimization of the OEW's $|S_{11}|$.

Test Number	F_l	F_p	Test Number	F_l	F_p	Test Number	F_l	F_p
1	12.1	13.63	6	12.5	13.94	11	12.3	14.56
2	12.3	13.63	7	12.1	14.25	12	12.5	14.56
3	12.5	13.63	8	12.3	14.25	13	12.1	14.87
4	12.1	13.94	9	12.5	14.25	14	12.3	14.87
5	12.3	13.94	10	12.1	14.56	15	12.5	14.87

3.5 gives the final design parameters for the OEW. The next section will present simulations using these values.

Tab. 3.5: Final OEW parameters chosen after final HFSS optimization.

Parameter	Value
a	4.755 cm
b	2.215 cm
W_l	10 cm
F_l	12.3 mm
F_p	13.64 mm
ϵ_r	2.3

Finally, it should be noted that the proposed design is not based on exhaustive optimization. The main goal here was to have a radiator which can irradiate the region of interest at multiple frequencies so that the measured S_{11} can be used to infer some properties of the region.

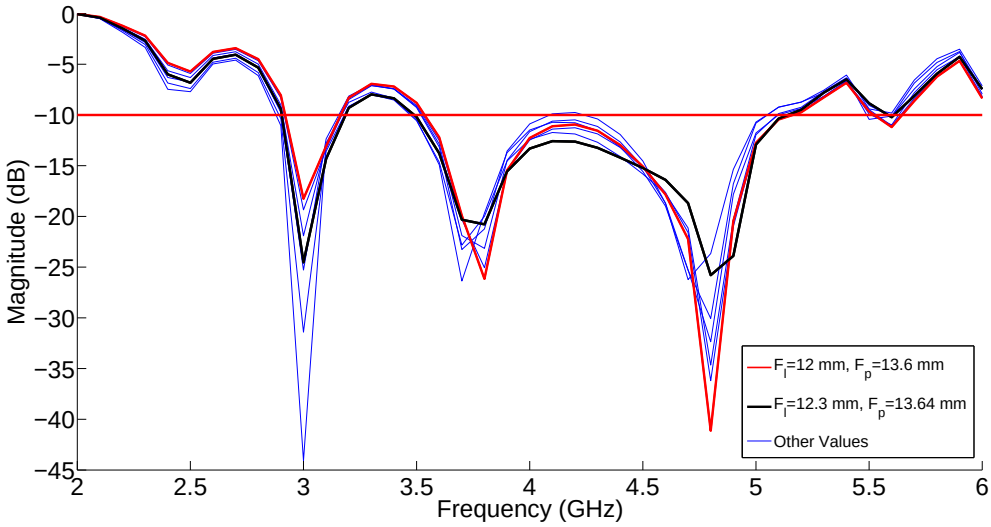

Fig. 3.7: Simulated $|S_{11}|$ for different feed parameters, given in Table 3.4.

As well, exhaustive optimization for a single scenario would not be practical since the antenna is to be placed on a material that has changing electrical properties (snow and sea ice). Herein, we designed the antenna to be placed on a snow layer. However, it was later decided to only look at the antenna placed on a sea ice layer in order to reduce the complexity of the system.

3.6 HFSS Simulated Results

This section will present $|S_{11}|$ when placed against different snow permittivities, sea ice, snow-covered sea ice, and free space. As well, cross-sections of the near-field distribution in free space, snow, and ice will be presented. Finally, the far-field pattern in free space will be shown.

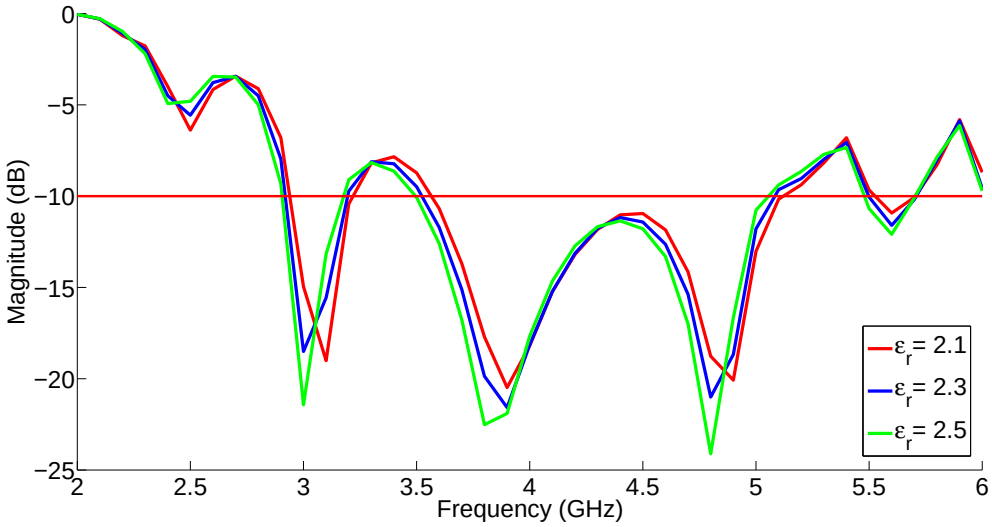

Fig. 3.8: The simulated $|S_{11}|$ of our OEW situated on snow cover for three different permittivities.

3.6.1 Simulated $|S_{11}|$ in Snow, Sea Ice, and Free Space

In the previous section, we optimized our antenna using only one snow permittivity. It is worthwhile verifying that a change in permittivity of the snow will not cause significant changes to the overall bandwidth of our OEW. However, we still want to observe small changes in the $|S_{11}|$ within the bandwidth. Figure 3.8 presents the $|S_{11}|$ of the OEW when placed against snow having a real permittivity of 2.1, 2.3, and 2.5 while keeping the same snow thickness (20 cm) and problem configuration as shown in Figure 3.3. The bulk conductivity in all three simulations remains as 10^{-8} S/m. As well, the setup for the simulation follows that of Section 3.5. We observe that the bandwidth is maintained for all three trials and that there are measurable changes to the $|S_{11}|$.

In practice, there will be times when the antenna is situated on sea ice with no snow cover. In fact, all of the experiments performed for this thesis were done on only sea ice. Since sea ice has a higher permittivity than snow, we expect to have a change in the bandwidth of the antenna. The $|S_{11}|$ of the OEW placed on (half space) sea ice layer having a permittivity of

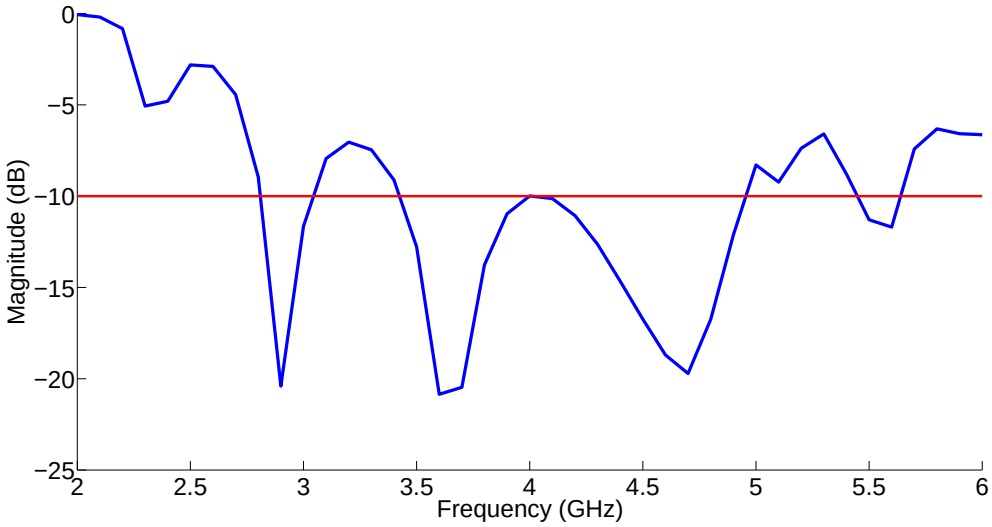

Fig. 3.9: HFSS simulation of the $|S_{11}|$ of the OEW placed on a sea ice layer.

3.8 and a bulk conductivity of 0.0135 S/m is given in Figure 3.9.

The results show an increase in the local maxima of the $|S_{11}|$ between 3 GHz and 5 GHz. The antenna was designed to couple with snow since it was assumed the antenna would be placed on more snow-covered sea ice than just sea ice. We now look at the $|S_{11}|$ for a snow layer on top of an ice layer.

Two simulations were performed for this configuration. In the first simulation, both layers were 5 cm thick, with the snow having a permittivity of 2.3, and the sea ice having a permittivity of 3.8. The bulk conductivity for the snow and sea ice were 10^{-8} S/m and 0.0135 S/m, respectively. The only change for the second experiment was modifying the snow thickness to 7.5 cm. The $|S_{11}|$ are shown in Figure 3.10. The two experiments appear very similar. This may be due to the lack of penetration depth, which will be later discussed at the end of this chapter based on the near-field distribution of the antenna.

Figure 3.11 shows the $|S_{11}|$ when placed on a snow layer, sea ice layer, and snow-covered sea ice. The snow layer (half space thickness) had a $\epsilon_r = 2.3$. The sea ice layer (half space thick-

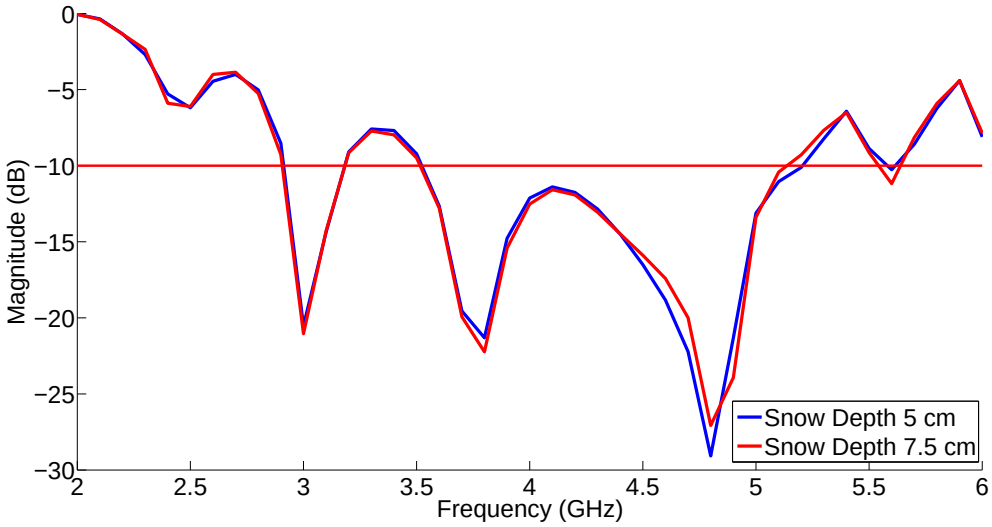

Fig. 3.10: HFSS simulation of the $|S_{11}|$ of the OEW placed on two snow-covered sea ice layers having 5 cm and 7.5 cm snow depths.

ness) had a permittivity of 3.8 and a bulk conductivity of 0.0135 S/m. The snow-covered sea ice had the same electrical properties as the other two tests, respectively. However, the snow thickness was 5 cm on top of a infinite half space of sea ice. As can be seen, the $|S_{11}|$ in all three cases still have frequency bands where the OEW is able to irradiate the medium. They also have differences between them that the inversion algorithm will look to utilize in reconstructing the complex permittivity profile.

The OEW situated in free space was the final $|S_{11}|$ simulation performed. This simulation helped determine the frequency range to be measured in the antenna test ranges, which will be discussed in Section 4.2. As expected, the bandwidth of the OEW in free space is significantly smaller than when the antenna is placed on either snow or sea ice. This result is primarily due to the mismatch between the UHMW plastic and air at the aperture of the OEW.

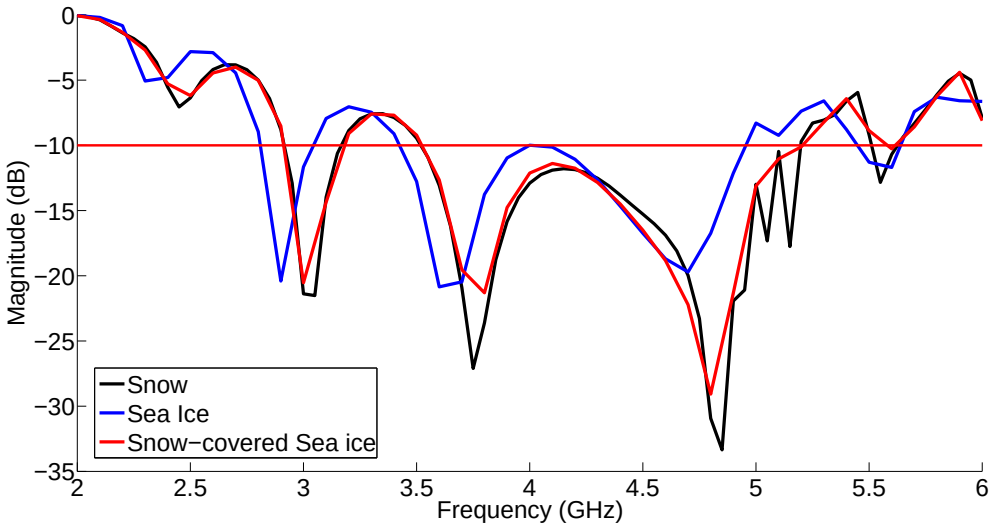

Fig. 3.11: HFSS simulation of the $|S_{11}|$ of the OEW placed on snow, sea ice, and snow-covered sea ice.

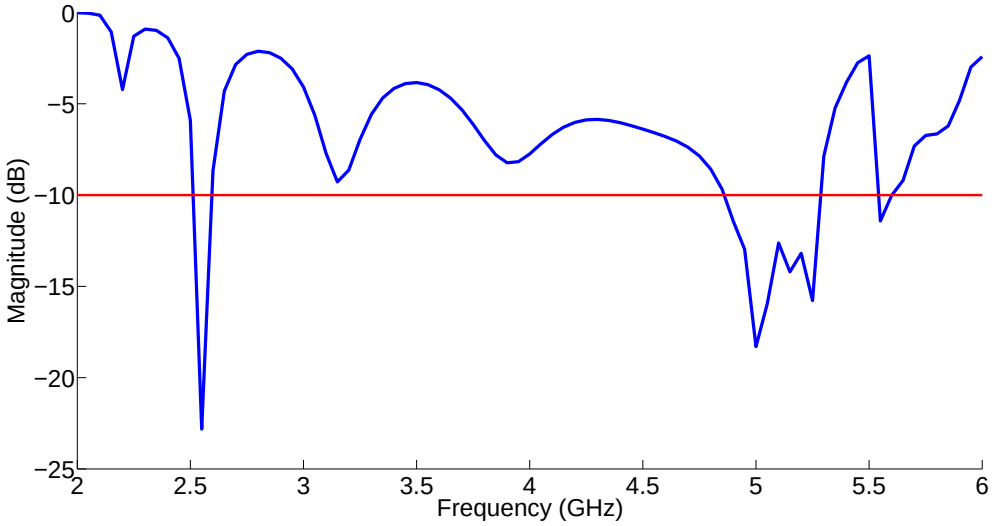

Fig. 3.12: HFSS simulation of the $|S_{11}|$ of the UHMW-filled OEW in free space.

3.6.2 Simulated Field Distributions in HFSS

This section presents the simulated near-field distributions of the OEW situated on sea ice and snow-covered sea ice. These fields give an approximation of the OEW's penetration capabilities. As well, they provide insight into how focused the OEW's energy is when illuminating the snow and sea ice. From Table 3.1, we speculate that the TE_{01} mode will not form due to the placement of the feed which is orthogonal to the electric field distribution. That is, if we consider b in Figure 3.2 is along the y-direction, and a is along the x-direction, then the TE_{01} electric field distribution polarization would be along a. If we consider a TE_{01} mode traveling through a rectangular waveguide and a feed orthogonal to the fields, then we would have no induced current on the feed. Since our system is linear, reciprocity theorem tells us that a current through the feed would not induce fields in the waveguide. What we are trying to show is that our electric fields propagating through our waveguide in the proposed frequency range are primarily polarized in the y-direction[5]. We chose to simulate the electric field distribution at 4.4 GHz to confirmed the dominant y-polarization in these simulations.

For ease of reading, we present only the E_y in the E-plane and H-plane; the fields are most dominant in this polarization. Figure 3.13 shows the E_y fields of the E- and H-plane in a sea ice layer. The sea ice layer had a permittivity of 3.8 and bulk conductivity of 0.0135 S/m. We observe a hot spot that extends from the aperture of the OEW to approximately 45 mm into the sea ice. As can be seen, the penetration seems to be more in the H-plane, which might be due to the fact that the size of the antenna ($a \approx 4.7$ cm) is larger in the H-plane than the size of the antenna ($b \approx 2.2$ cm) in the E-plane. Also, the E field at the aperture of the antenna in the fundamental mode is expected to have a cosine taper in the H-plane, which could explain the taper of E_y in the H-plane close to the surface ($z = 0$). On the other hand, the E field at the aperture of the antenna in the fundamental mode is expected to

[5] We consider the E-plane of the antenna to the be yz plane and its H-plane will be the xz plane.

be uniform, which could explain a relatively uniform E_y in the E-plane close to the surface ($z = 0$).

Figure 3.14 shows the E_y fields of the E- and H-plane in snow-covered sea ice. The snow layer was 5 cm thick, with a relative permittivity of 2.3 and bulk conductivity of 10^{-8} S/m. The sea ice layer had a relative permittivity of 3.8 and bulk conductivity of 0.0135 S/m. We observe in the H-plane the hot spot extending to approximately 50 mm, which corresponds to the snow/sea ice boundary. There is a smaller hot spot within the sea ice, located between 60 mm and 65 mm.

In both sea ice and snow-covered sea we have fields extending beyond 100 mm. However, it is unknown whether these fields will have significant impact on the measured $|S_{11}|$. As well, these simulations do not include the true microstructures of snow or sea ice. In practice, these differences may significantly reduce the observable penetration depth ($|S_{11}|$ sensitivity). Overall, we speculate that this OEW irradiates between 40 mm and 100 mm depending on the medium.

As will be noted in the future work, it is desired to have more sensitivity to deeper parts of the domain of interest. However, to this end, it is speculated that we need to use radiators with more focused near-field distributions. This is challenging since most antenna designs have been performed for far-field applications. Recently, some research groups have investigated the design of antennas for near-field applications including focused near-fields for imaging or wireless power transfer [43].

From a theoretical point of view, when the OEW irradiates the region of interest, this region will have induced contrast sources [44]. These contrast sources are related to the induced field inside the region of interest. These are, in fact, contrast sources that radiate back and we can use their signatures for performing imaging, remote sensing, or detection. Therefore,

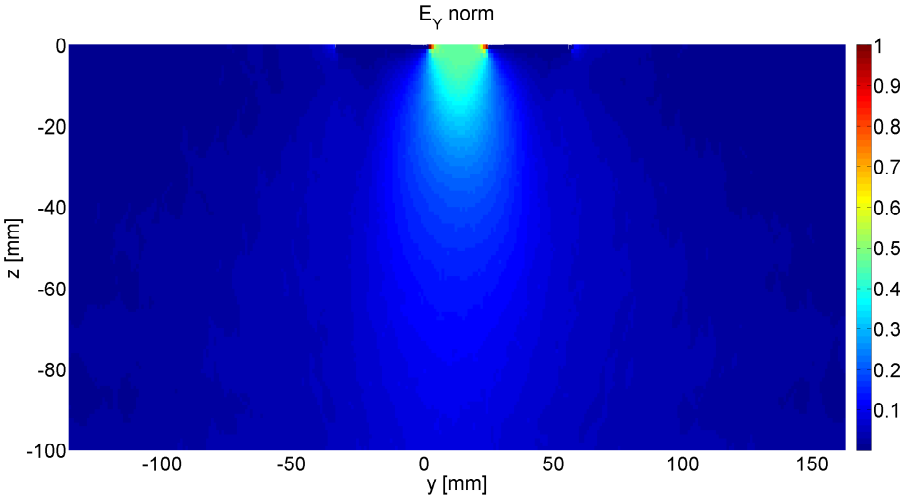

(a) E-plane.

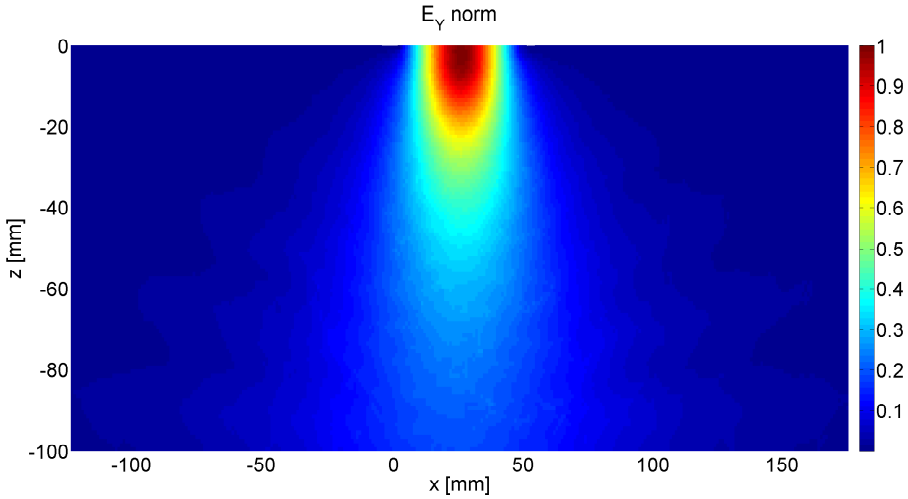

(b) H-plane.

Fig. 3.13: E_y polarized fields in the E-plane and H-plane of a sea ice layer. ($z = 0$ is the interface of air and sea ice layer. As z becomes more negative, we are further into the sea ice layer.)

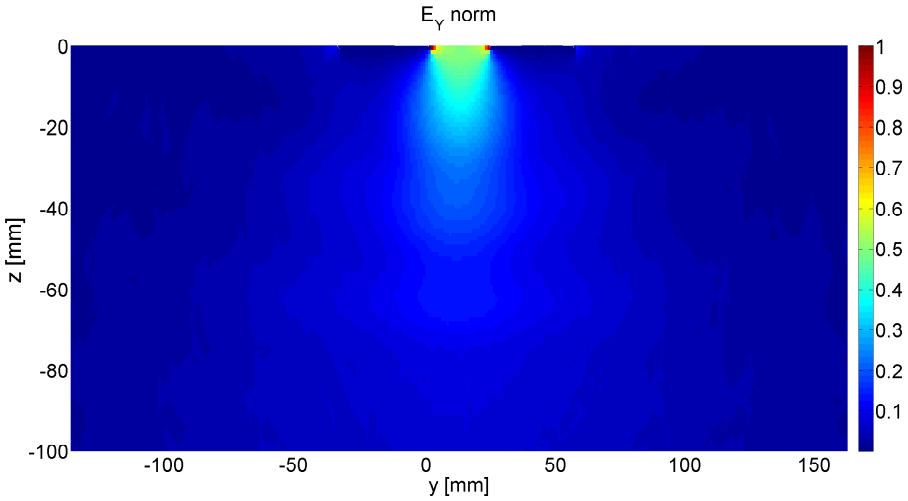

(a) E-plane.

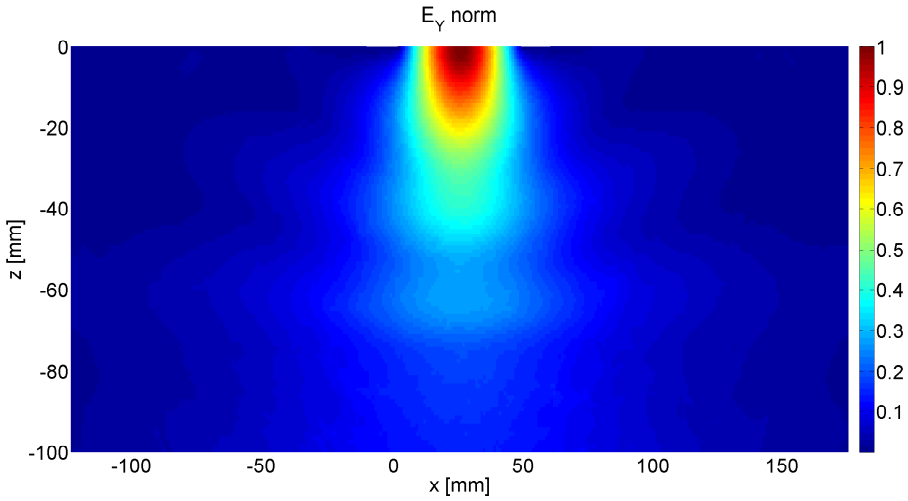

(b) H-plane.

Fig. 3.14: E_y polarized fields in the E-plane and H-plane of snow-covered sea ice.

to distinguish between the profile in Figure 3.13 and Figure 3.14, the necessary condition is to have different induced fields inside these two profiles. As can be seen by comparing the two, the induced fields (E_y) in these two profiles are different. Therefore, we have the necessary condition to perform remote sensing.

However, since field measurements inside the profiles would be destructive (placing an antenna or other sensor within the snow of ice), we generally do not want to use these internal fields for remote sensing. To this end, we rely on an external measurement, which in our case is $|S_{11}|$. Note that the $|S_{11}|$ has much less information as compared to fields inside the profiles since the $|S_{11}|$ is only a real number, whereas the field distribution inside the profiles contain many complex-valued data.

4

Antenna Fabrication and Testing

The rectangular OEW, shown in Figure 4.1 was fabricated at the ECE department's machine shop at the University of Manitoba. A copper wire soldered onto a female-female SMA adapter was used as the probe to excite the OEW and measure the received electromagnetic energy, shown in Figure 4.2. The circular flange was made of brass to prevent oxidation of the metal around the aperture. The rest of the body is made out of copper, where the UHMW plastic protects the inside of the waveguide from oxidizing. We first confirm the permittivity of the UHMW plastic, and the remaining sections look at the antenna's field distribution in free space and the effects temperature has on the antenna.

4.1 UHMW Polyethylene Permittivity Measurement

The UHMW plastic's permittivity over the frequency band was tested using the setup shown in Figure 4.4. A Agilent high precision dielectric probe was placed on top of a $20x20x2.5$ cm^3

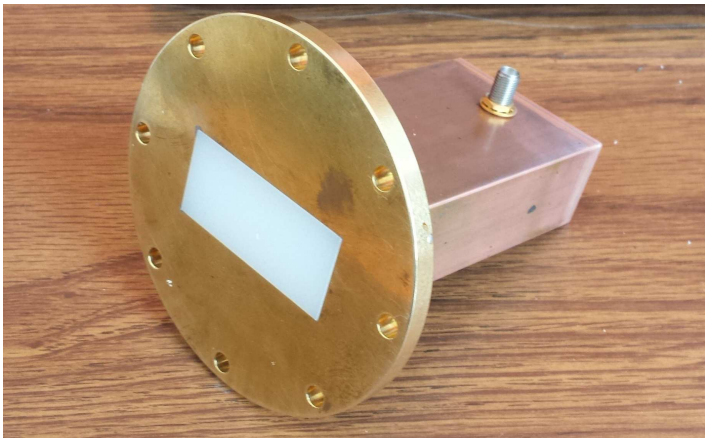

Fig. 4.1: The fabricated UHMW plastic filled OEW with brass flange.

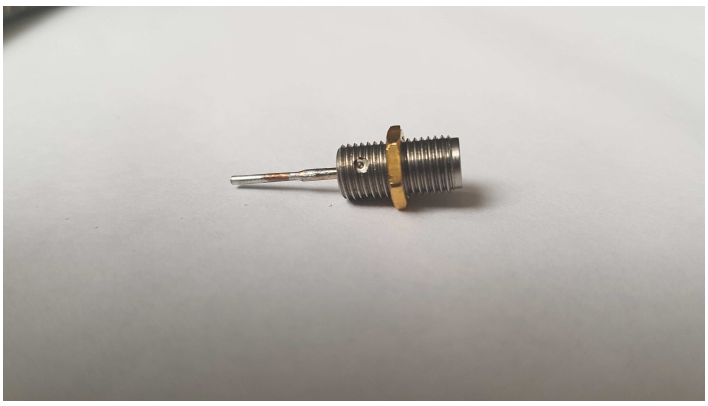

Fig. 4.2: The probe feed and connector used to connect the OEW and coaxial cable.

block of UHMW plastic. In our HFSS simulation, the plastic's permittivity was assumed constant, $\epsilon_r = 2.3$, over 3 GHz to 5 GHz. Initially, the high performance probe was calibrated using a probe short, open air, and deionized water. The probe was then placed flush with the surface of the UHMW plastic.

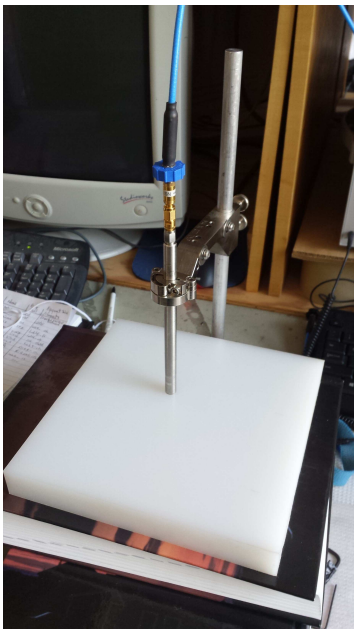

Fig. 4.3: Experimental setup for determining the complex permittivity of the UHMW plastic using a high performance probe.

According to [45], the plastic's complex permittivity is $\epsilon' \approx 2.289$ with negligible loss ($\epsilon'' \approx 0$) between 3 GHz and 5 GHz. The measured results are shown in Figure 4.4, which show an average ϵ' of 2.29 and ϵ'' of 0.12. The main challenge associated with this experiment was eliminating the air gap between the probe and plastic. An air gap would cause ϵ' to be close to the permittivity of air. As well, the UHMW plastic may not have been thick enough. Overall, the experiment showed that the effects of frequency on the permittivity of the UHMW plastic was minimal.

This experiment not only shows that our assumption regarding constant permittivity of the UHMW plastic was correct, but also demonstrates the concept of indirect measurement of

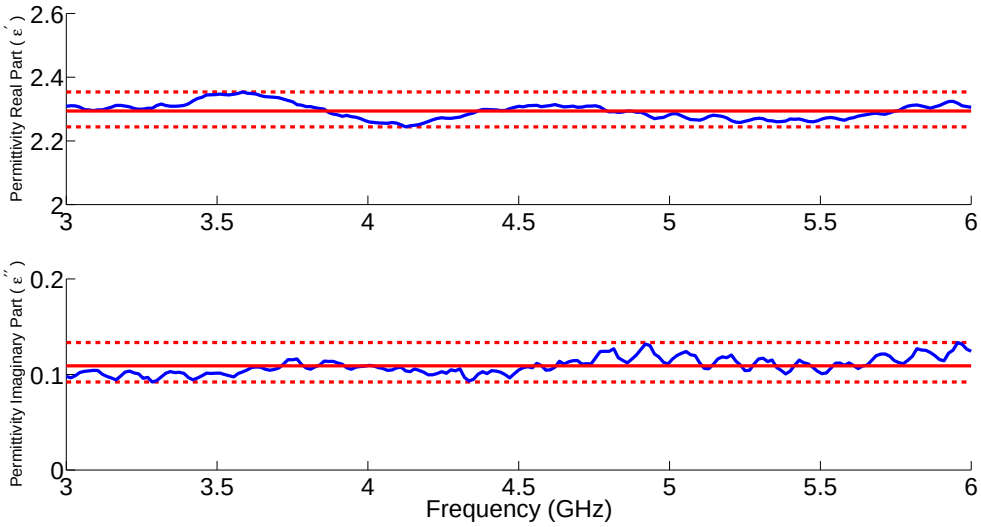

Fig. 4.4: The complex permittivity of the UHMW plastic used to fill the OEW. The dashed red lines indicate the minimum and maximum values, the solid red line represents the average value across the frequency range, and the blue line are the measured values.

permittivity, which is similar to the concept being investigated in this thesis. This can be explained as follows. This commercial dielectric measurement system indirectly measures the complex permittivity through the impedance of the material. That is, the material under test could be considered the load of a transmission line. The system is first calibrated to accurately model the probe. The permittivity of the material is then determined by software based on the magnitude and phase of the reflected signal.

4.2 Antenna Test Range Measurements

This section presents measurements using a compact antenna test (CATR) and a spherical near-field range (SNFR). Antenna test ranges are used in the characterization of antenna parameters such as gain, radiation pattern, beamwidth, and polarization. The important information measured were the SNFR near-field electric fields and the CATR far-field gain. These results are used to verify simulated far-field patterns. However, they do not directly

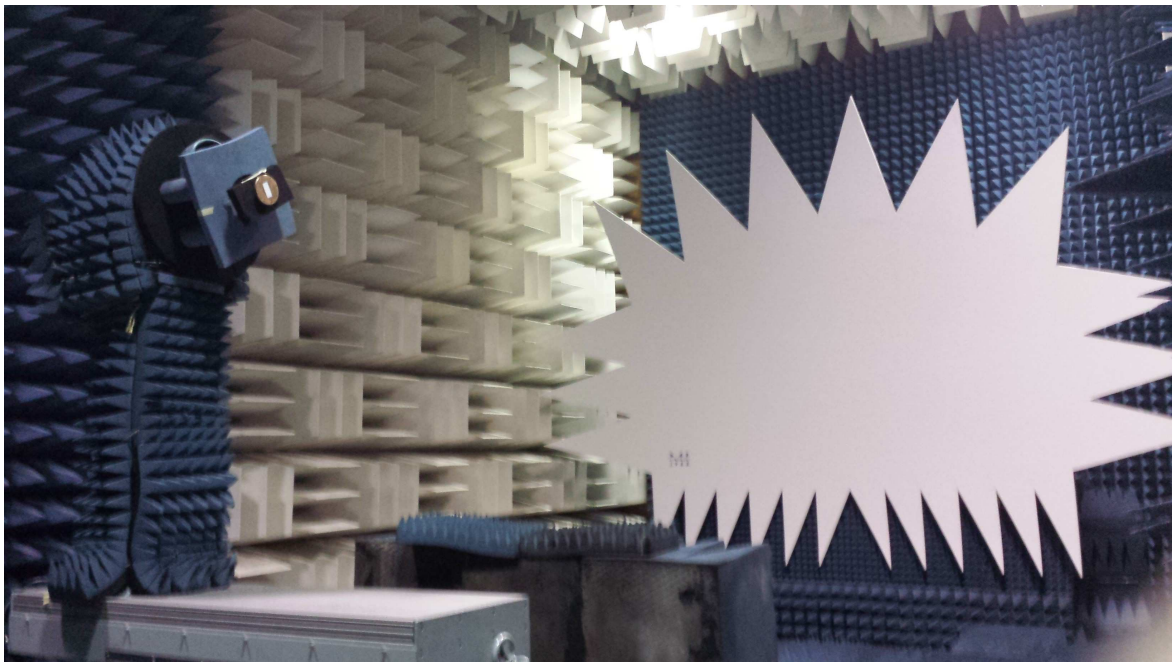

Fig. 4.5: Experimental setup of the OEW in a compact antenna test range having a serrated edge reflector. This system is housed in an anechoic chamber covered with radio frequency absorbers to simulate free space conditions.

correspond to how the antenna propagates into snow or sea ice, since these measurements were done in free space.

Both experiments were performed in anechoic chambers located at the University of Manitoba's antennas lab. Figure 4.5 shows the setup for the CATR. The system operates by a feed illuminating a serrated edge reflector. This reflector reflects the signal towards the antenna under test (AUT). At the AUT, the electromagnetic waves theoretically form into a plane wave, since the reflector can be viewed as a device that converts spherical waves of the feed to plane waves. Since our antenna is composed of all linear components, the reciprocity theorem tells us that the receiving and transmitting pattern of the AUT is the same [41]. The boom that the antenna is attached to rotates in order to collect field measurements at different angles. The results of this experiment will be shown at the end of this section, juxtaposed with simulation and the SNFR measured gain.

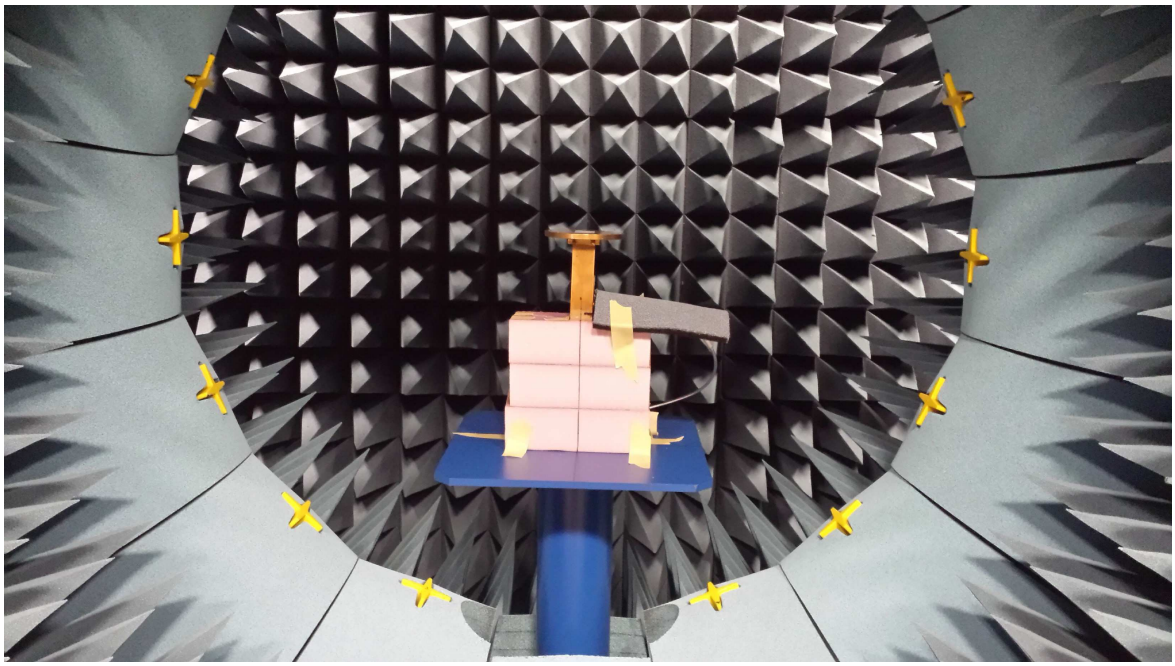

Fig. 4.6: The SNFR setup for measuring the near-field of the OEW. Absorber material is used to reduce measurement errors due to the connecting coaxial cable.

The difference between the CATR and the SNFR is in which the far-field pattern is determined. CATR directly measures this pattern, whereas the SNFR measures the near-field of the antenna and then performs a near-field to far-field transformation in order to obtain the far-field pattern. The SNFR setup is shown in Figure 4.6, where the antenna is situated on top of foam in order to place the aperture of the antenna in the center of the system. The yellow crosses are the probes that measure the two orthogonal polarizations of the antenna. The antenna platform rotates in order to collect the near-field data over a spherical surface.

The far-field patterns for both systems were measured from 4.9 GHz to 5.2 GHz in increments of 100 MHz. We present the co- and cross-polarized far-field pattern for the E- and H-planes of the OEW. The E-plane corresponds to fields directed along the short dimension of the antenna, b, and the H-plane is in the direction of a. Herein, we present these measurements for 5 GHz, shown in Figure 4.7.

At 5 GHz, the measurements from both systems are near simulations. At angles further

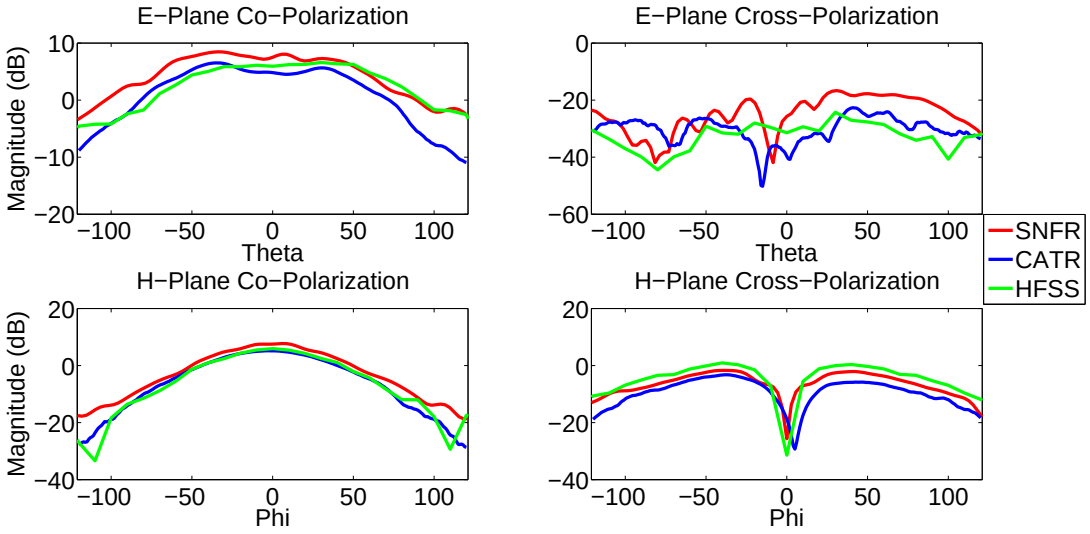

Fig. 4.7: The co-polarization (left) and cross-polarization (right) of the E- and H-plane at a frequency of 5 GHz. Theta and Phi denote the elevation and azimuth angles in spherical coordinates)

away from the center there is more error in the measurements for CATR, primarily due to the deteriorating plane wave characteristics of the incoming signal. The measured E-plane cross-polarized pattern of the three measurements are different due to the limiting factors of the noise floor for each systems. Typical CATR systems have a ± 1 dB error in the gain measurement which accounts for the small discrepancy between the systems. As well, we speculate that errors arise from the gain calibration in the CATR and SNFR.

4.3 Equipment and Measurement Technique

This section's purpose is to establish the equipment setup and measurement methods used for all cold lab and subsequent field experiments. The OEW operates in a monostatic configuration where it acts as both a transmitter and receiver. A VNA (Agilent FieldFox N9916A) connected via a type K coaxial cable is used to power the OEW. The equipment necessary for measurements is shown in Figure 4.8. The VNA is placed in an insulated box which allows the VNA to operate within its specified operating temperatures. Only one port of

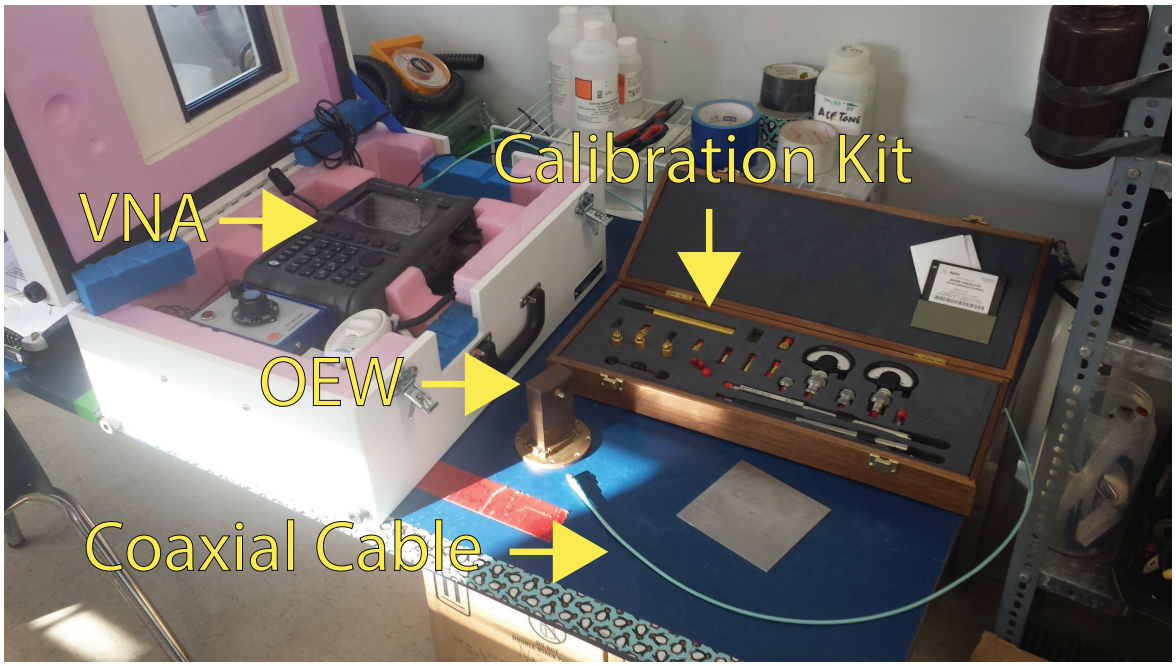

Fig. 4.8: Equipment used for experiments include a VNA, OEW, type K coaxial cable, and a calibration kit. Note, the VNA has been placed in an insulated box in order to operate at room temperature.

the VNA is required. The calibration kit (Agilent 85052B) is necessary in order to measure accurate power readings at the coaxial cable/OEW interface. The steps to performing the measurement are as follows.

1. Turn on the VNA and allow sufficient time for the system to stabilize. From experience, the RF port temperature settles at $55°C$.

2. The VNA can be setup to the required settings while waiting for the system to warm up. These settings include the start and stop frequency, number of points, and IF bandwidth. The IF bandwidth was selected as 1 KHz. The smaller the IF bandwith, the more accurate the measurement; however, the measurement speed becomes slower the smaller the IF bandwidth.

3. Calibration must be performed prior to measurements. The open-short-load method is used to calibrate the system. Ideally, the setup is placed at the measurement location

and is not moved once calibration has started. To perform the calibration, we follow the VNA's on-screen instructions. Calibration can be verified afterwards by examining the S_{11} when the open, short, or matched load is connected, which should be $1\angle 0^{\circ}$, $1\angle 180^{\circ}$, and $0\angle 0^{\circ}$ across the entire frequency range, respectively.

4. Connect the OEW to the coaxial cable. The user is now ready to take an S_{11} measurement.

A setting that was not extensively tested was the VNA's power level output. The VNA outputs -15 dBm by default. Future experiments could look at the potential use of a power amplifier in order to achieve further penetration depth. However, more power may run the risk of melting the snow/sea ice directly under the OEW. Before performing experiments on sea ice, it was crucial to look at the effects low temperature has on our measurement system, and calibration technique.

4.4 Temperature Effects on Antenna and Calibration

The effects of low temperature on the antenna and calibration are important due to changing physical properties when transitioning from warm to cold temperatures. Metal physical properties do not change much with respect to low temperature. However, plastics can become brittle and/or shrink. The latter could potentially allow oxygen and salts to seep into the waveguide and alter the electrical properties of the antenna. According to the data sheet, the UHMW plastic's permittivity should not be affected by temperatures below $0^{\circ}C$ [46]. In the cold laboratories located at the CEOS, two experiments were conducted. In each experiment we measured the $|S_{11}|$ of our antenna in free space. Both tests involved varying the temperature from $-10^{\circ}C$ to $-20^{\circ}C$ in $2.5^{\circ}C$ intervals. The temperature was then raised back to $-10^{\circ}C$. This second set of measurements are used to distinguish between

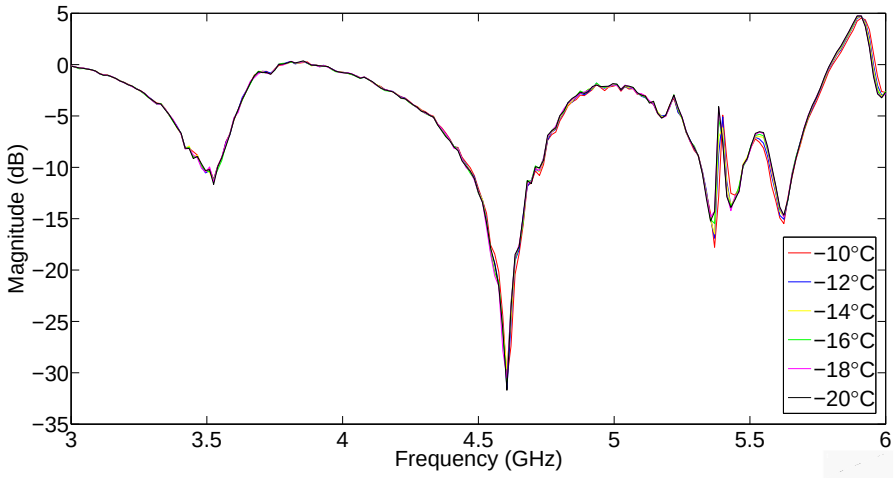

Fig. 4.9: $|S_{11}|$ of the OEW in free space when the system is calibrated at $-10°C$.

temperature dependence and calibration drift. At each temperature, we allowed the system temperatures to settle for twenty minutes before taking measurements. The only difference between the two experiments was the temperature at which calibration of the system occurred. Initially, we calibrated the system at $-10°C$, the results are given in Figure 4.9. As can be seen, at certain frequencies the reflection coefficient is greater than 0 dB, which means more power is received than what the VNA transmitted. This observation would indicate the VNA was not calibrated correctly since there were no other sources present.

Afterward, we then calibrated our system at room temperature ($20°C$) and repeated the experiment. The results are given in Figure 4.10. As we can see, the reflection coefficients from 3 GHz to 6 GHz are below 0 dB. We did not see any noticeable calibration/system drift.

From these results, we conclude that calibration should be done at room temperature. This poses a problem when your measurements are to be performed in an Arctic environment where the temperature is below freezing. To this end, we decided to calibrate the system at room temperature, and then move the system to the measurement location. This movement causes error in the measured S_{11} with respect to both magnitude and phase. A change in

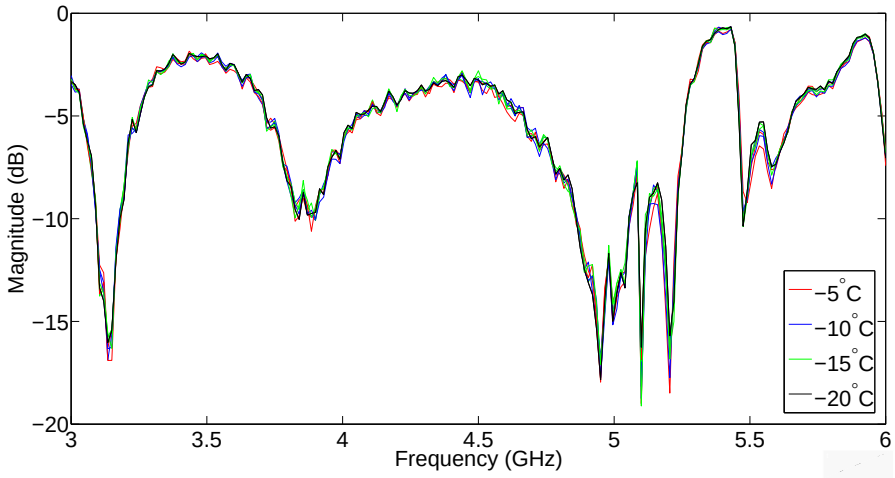

Fig. 4.10: $|S_{11}|$ of the OEW in free space when the system is calibrated at $20°C$.

temperature can affect the connection between components which can drastically alter measurements. As will be explained later, we use a calibration factor in our inversion technique. Therefore, if this change in temperature affects these connections in a similar fashion, we potentially could factor out this error through calibrating our data[1].

[1] Calibrating our system refers to factoring out the effects of the cable. In essence, we are performing measurements as if the antenna is hooked directly up to the VNA. Calibration of our data is a completely different concept that applies a filter on our experimental measurements to better relate to our forward model in the inversion algorithm.

5

Sea Ice Data Collection

This chapter focuses on the collection of experimental S_{11} data, primarily at SERF, using the OEW antenna and test setup outlined in Section 4.3. SERF is an Arctic mesocosm located at the University of Manitoba. At this location there is an outdoor sea water pool (60 feet long, 30 feet wide, and 8 feet deep. There is a movable roof to control ice growth and snow cover, and is equipped with a variety of sensors and instruments. Before an experiment begins, a heated glycol pump is used to warm the water to ensure there is no ice present on the surface. The pumps are then turned off to allow the formation of ice.

Time-series S_{11} measurements of sea ice were collected at SERF in 2015 and 2016. As well, supplementary physical samples of the ice cores were collected. These physical samples were used to determine the salinity and temperature profile of the sea ice. As will be proposed and explained later, these physical measurements and the S_{11} measurements can be used together to calibrate the reconstruction algorithm in an attempt to predict sea ice growth based on future S_{11} measurements. The last section of this chapter study the antenna's sen-

sitivity to variation in the sea ice thickness, salinity, and temperature. These experiments were conducted in the cold laboratories located at the CEOS.

5.1 SERF 2015 and 2016

Between February 12$^{\text{th}}$ to February 21$^{\text{st}}$, 2015, S_{11} data of sea ice growth at SERF were collected. The sea ice was grown under calm conditions, shown in Figure 5.1, with no snow cover. The roof of the enclosure was on throughout the entire experiment. We began testing when the ice was 24 cm thick. On the final day, the ice thickness was 35 cm. The timing of the samples were once per day at approximately 2:00 pm. Each sample consisted of an S_{11} measurement, followed by a physical extraction of the core at the same location. Since we were taking physical samples, subsequent measurements were performed nearby to previous days' measurements. We were able to do this since we observed the ice sheet thickness and structure were relatively consistent across the pool, with the ice being slightly thicker (1 cm to 2 cm) along the edges. We now describe how each sample was performed in more detail.

Based on the observations of Section 4.4, VNA was calibrated inside (room temperature) before moving the system to the sea ice surface, shown in Figure 5.2. We placed the VNA on a sheet of wood in order to further protect the VNA. To minimize the effect of movements and also to investigate a more affordable measurement system, we only considered the magnitude of our measurements since the phase is highly sensitive to cable movement, and also phaseless (magnitude-only) measurements can reduce the cost of a potential future system by allowing the use of a power meter for measurements. A thin layer of water was observed between the OEW and ice surface. We believe this is due to the OEW acting as a heat sink due to its high thermal conductivity. We collected $|S_{11}|$ measurements of the sea ice between 3 GHz and 6 GHz. Figure 5.3 shows the magnitude of the S_{11} for the first four

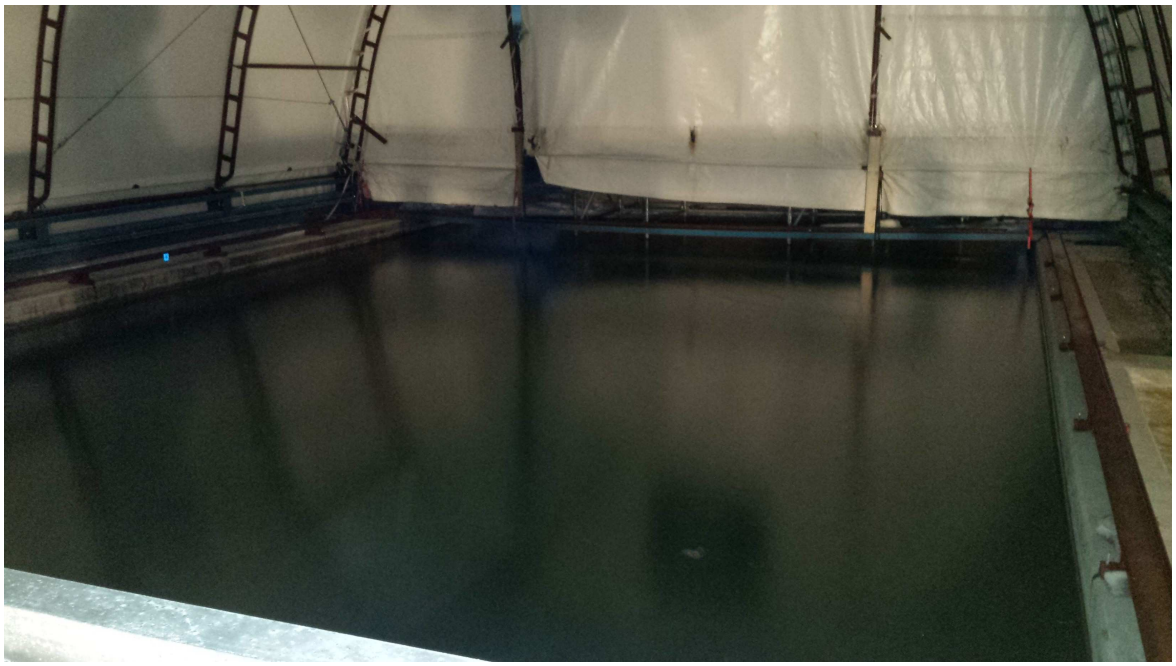

Fig. 5.1: The ice surface grown at SERF under a closed canopy during February, 2015.

days of measurements. We observed that our measurements between these days show differences in the magnitude. It is these differences that we will look to exploit in our inversion algorithm. As the ice thickness is assumed greater than the penetration depth of our antenna, we speculate the temperature and salinity of the upper layers to be the major contribution to these differences. We will explore the antenna's sensitivity to thickness, temperature, and salinity at the end of this chapter.

Using a 10 cm diameter ice corer, a physical sample was then extracted upon collecting the S_{11} measurement. The thickness of the ice core was measured, followed by the temperature. Using a drill, holes were drilled in the extracted core, pictured in Figure 5.4 (right side), at 2.5 cm or 5 cm intervals along the ice core's vertical dimension. The temperature was then measured at these intervals by inserting a temperature probe into the drilled holes. Next, the core was sliced into sections, at the same intervals as the temperature, and sealed in plastic bags. At the end of the experiment, the sections were melted and the bulk salinity measured using a conductivity probe. The results for the thickness, bulk temperature and

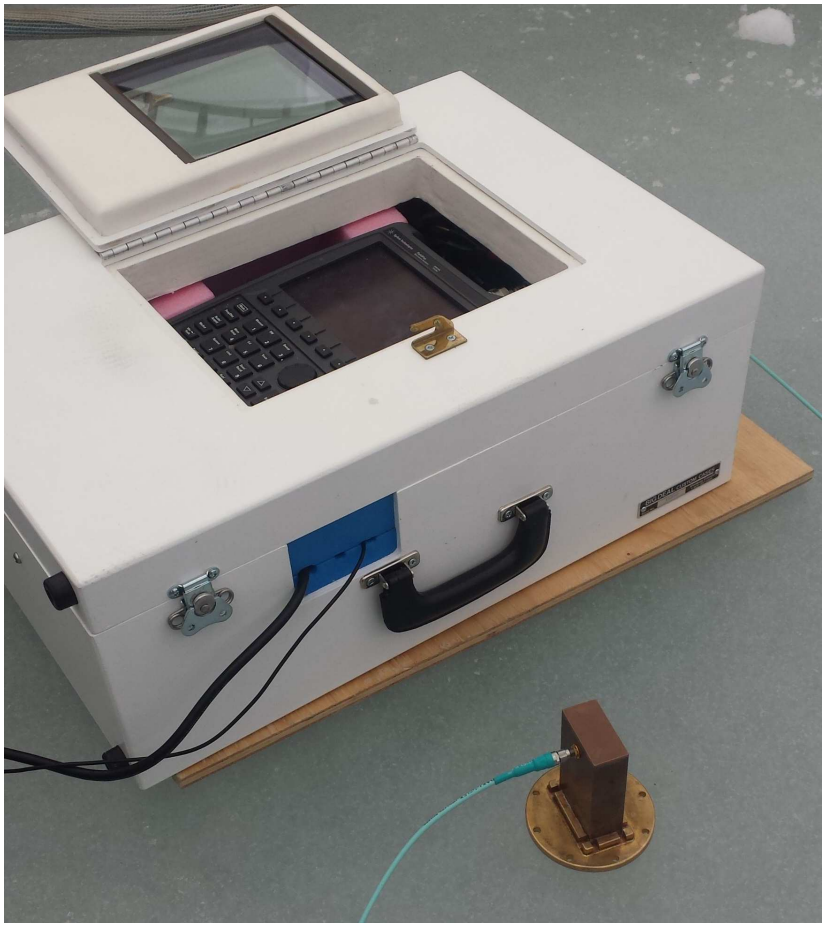

Fig. 5.2: The VNA and OEW situated on the sea ice surface at SERF 2015.

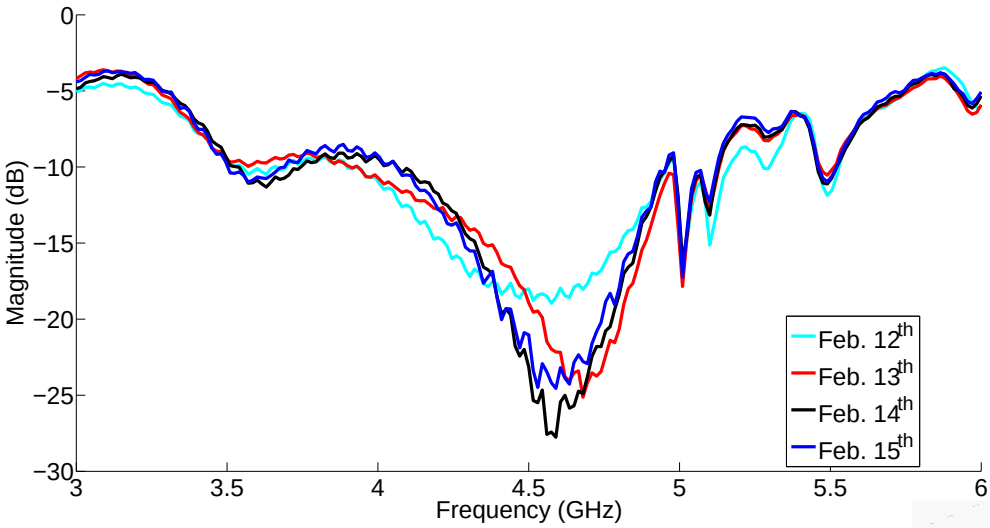

Fig. 5.3: The $|S_{11}|$ measurements collected at SERF 2015 during the first four days.

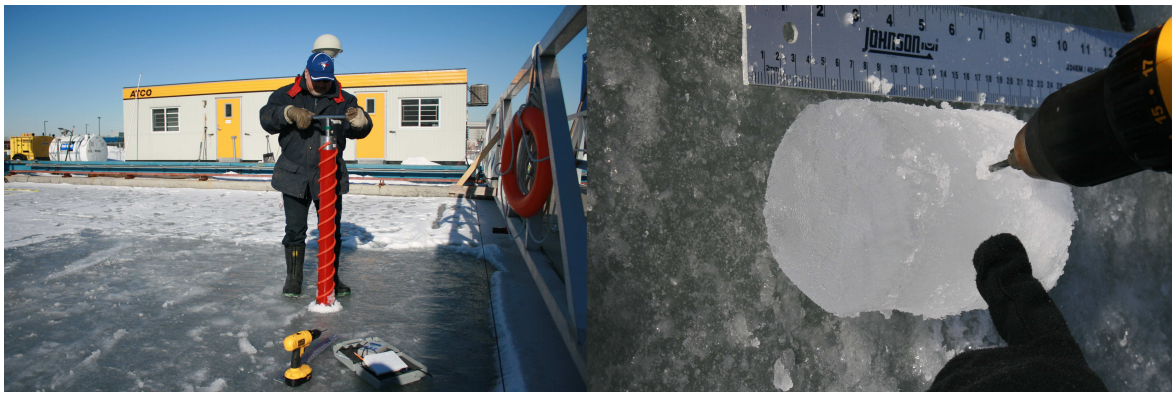

Fig. 5.4: An example of ice core extraction (left) and temperature measurements (right).

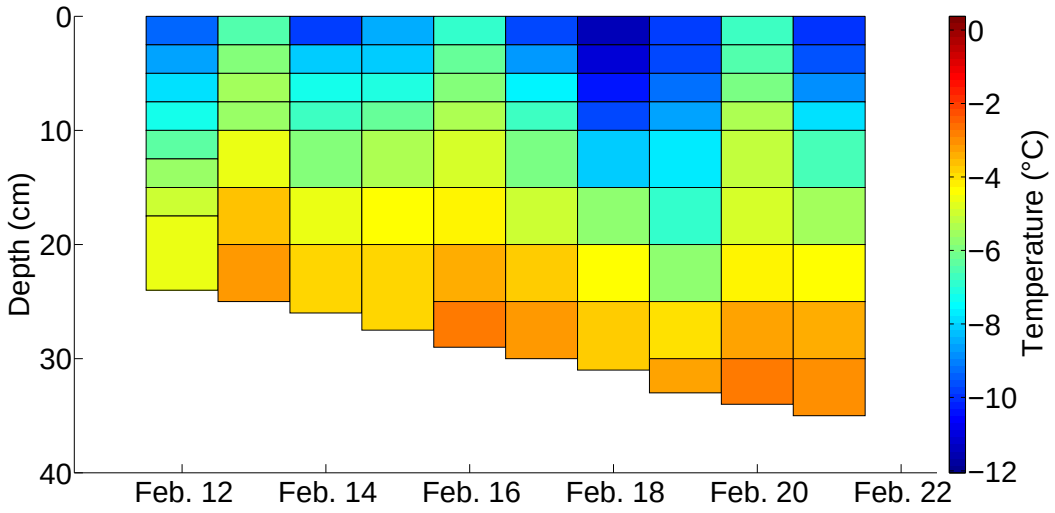

Fig. 5.5: Temporal temperature profile of the sea ice at SERF 2015.

bulk salinity are given in Figure 5.5 and Figure 5.6, respectively. The temperature follows a linear downwards gradient from colder to warmer with respect to depth. As well, the salinity profile for each day follows the predicted C-shape.

We also collected a series of S_{11} measurements the following year in 2016 from February 12^{th} to February 18^{th}. The goal of this experiment was to observe the effects spatial variations have on our measurements. That is, we collected measurements at ten positions on the ice per day within a 1m^2 area. This way we could observe if the OEW was sensitive to variation in the brine pockets and structure of the surface layer. Unfortunately during these

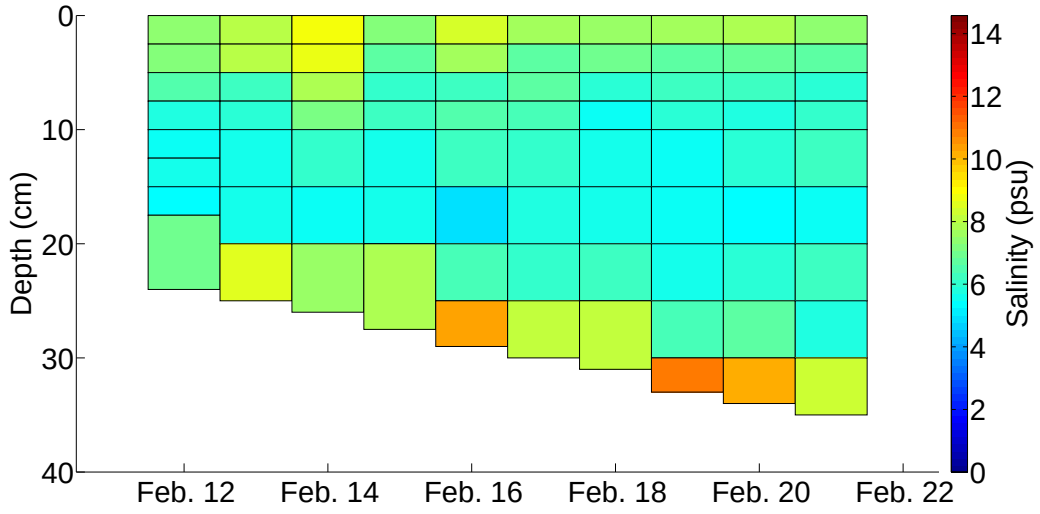

Fig. 5.6: Temporal salinity profile of the sea ice at SERF 2015.

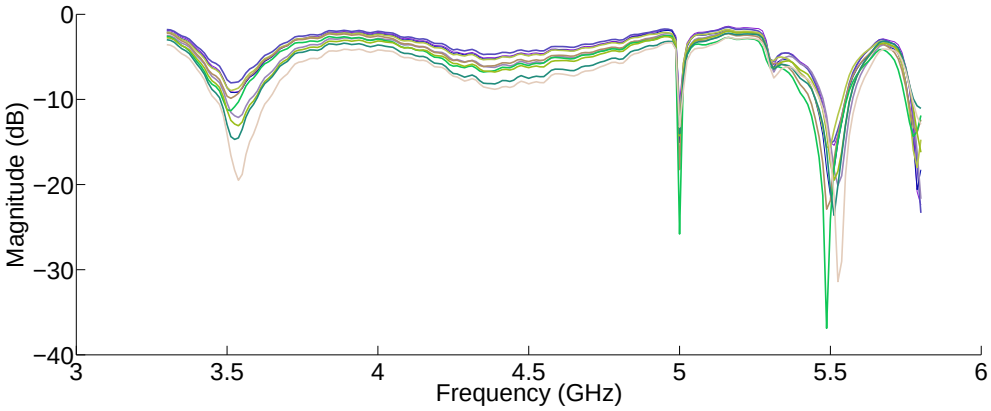

Fig. 5.7: $|S_{11}|$ measurements on a wet sea ice surface for February 18$^{\text{th}}$, 2016.

measurements, warm temperatures[1] and direct sunlight caused a wet surface layer on top of the sea ice. Due to this wet surface, the OEW was unable to penetrate into the ice layer. To this end, the S_{11} measurements collected were in effect seeing a half space of sea water. In Figure 5.7, we observe the OEW having a large $|S_{11}|$ with a very low bandwidth. (It should be noted that the challenge associated with having a highly conductive wet surface/slush layer also affects other high frequency active sensors such as scatterometers.)

[1] five out of the seven days had temperatures close to or above $0°C$

5.2 Antenna Sensitivity to Sea Ice Properties

This section looks at the effects sea ice salinity, temperature, and thickness have on the OEW's measured $|S_{11}|$. As mentioned previously, these properties affect the complex permittivity profile of the sea ice, which in turn should be reflected in the measured $|S_{11}|$. In addition, we look to observe the effects the randomness of the brine inclusions have on the antenna's measurements. This section presents mainly qualitative and speculative observations as it is fairly difficult to isolate the effects of each geophysical property of the sea ice.

We performed a series of experiments to look at the effects different ice properties have on our measured $|S_{11}|$. These experiments were conducted in the cold lab located in CEOS. Four insulated plastic containers were built, shown in Figure 5.8, in order to grow artificial sea ice. These containers were half filled with water with different salinities: 0, 5, 10, and 15 psu. The containers were filled halfway in order to prevent cracking due to ice expansion. The total depth of the water in each container was 18 cm. This experiment was performed three times, with the only difference being the ambient air temperature at which the ice grew: -15, -10, and $-5°C$.

Before proceeding with the experiments it was worthwhile to look at the theoretical effects temperature and salinity have on the complex permittivity of sea ice. In Figure 5.9, we calculated the theoretical permittivity of sea ice based on the Polder van/de loor dielectric mixing model for a frequency of 4 GHz (center frequency of our antenna) [14]. At this frequency, we note that at a temperature of $-15°C$ there should not be a significant difference in the complex permittivity between the 5 psu and the 15 psu container. However, we expect a significant difference in the complex permittivity when the temperature is $-5°C$.

Fig. 5.8: Four insulated containers used to grow ice from water having different salinity. The containers were approximately 60 cm in diameter, with a water depth of 18 cm. This experiment was performed at a cold laboratory located in CEOS.

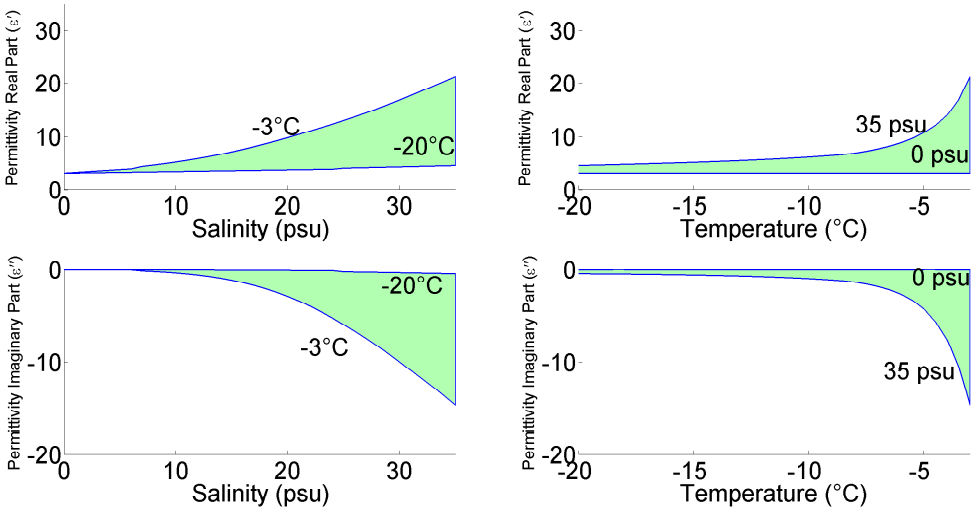

Fig. 5.9: Complex permittivity range (light green area) based on the Polder van/de loor mixing model at 4 GHz. The left column gives the complex permittivity range from $-20°C$ to $-3°C$ for salinity from 0 psu to 35 psu. The right column gives the complex permittivity range from 0 psu to 35 psu for temperatures from $-20°C$ to $-3°C$.

5.2.1 Ice Growth at $-15^{\circ}C$ and $-10^{\circ}C$

We began our cold room experiment by allowing the containers to freeze at an ambient temperature of $-15^{\circ}C$. In this experiment we let the ice grow undisturbed for four days. This allowed the ice to grow thicker than our antenna's predicted penetration depth. Therefore we could determine if different salinity at this low temperature would have any effect on our measurements.

On the fifth day we collected ten $|S_{11}|$ measurements as well as one surface temperature for each container. Afterwards, we drilled a small hole in the ice in each container to measure the thickness. Figure 5.10 shows the location of these ten measurements. At each location two orthogonal measurements were taken. That is, we rotated our antenna 90° in order to observe the effects of the antenna orientation. We did not observe any noticeable difference in the measurement with regards to rotating the antenna. As well, we did not notice any considerable differences in the measurements with respect to spatial variation (measurements at different locations in the container).

We then compared the $|S_{11}|$ measurements between the four containers and observed that three of the four containers had results relatively close to one another. However, the container with the 15 psu water had a brine skim along the surface, resulting in similar observations to SERF 2016 measurements. As predicted, based on the dielectric mixing model, we observed no significant difference in our antenna measurement at this low temperature. The surface temperatures of each container was roughly $-11^{\circ}C$. Figure 5.11 shows the $|S_{11}|$ measurements of the 5 psu and the 10 psu container.

We then repeated this experiment, but changed the ambient temperature to $-10^{\circ}C$. The results once again showed that when the ice thickness was greater than the estimated penetration depth, the $|S_{11}|$ were the same for the containers. We also note that the measurements

Fig. 5.10: The $|S_{11}|$ measurement locations. At each location two measurements were taken orthogonal to one another.

were the same for the two different temperatures, an example is shown in Figure 5.12. So far, we have observed that the salinity does not appear to affect our antenna measurements when the temperature is below $-10°C$ if the thickness of the ice is greater than the expected penetration depth. However, we do not know the exact salinity of the ice, only the starting salinity of the water. In our final experiment at $-5°C$ we extract a core from each container to show the salinity of the ice is different.

Although these experiments do not include varying thickness values, we expect the antenna's $|S_{11}|$ to become more sensitive to changes of salinity values as the thickness of the ice decreases and the water below becomes more "visible" to the antenna. This can be explained as follows. For smaller thicknesses of ice, the water layer becomes more "visible" to irradiating electromagnetic waves, therefore we will have multiple reflections in the ice layer due to the discontinuity at the ice/water interface. Having more reflections in the ice layer may emphasize smaller changes in the complex permittivity of the ice and therefore may have a greater effect on the S_{11} of the antenna.

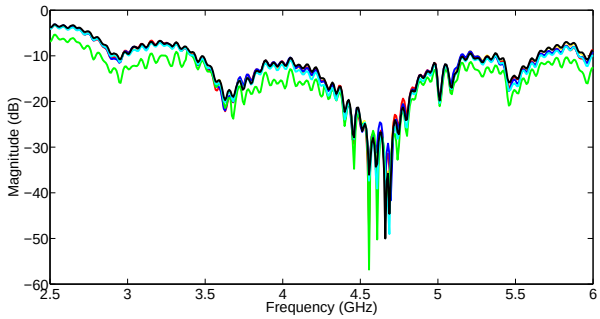

(a) 5 psu

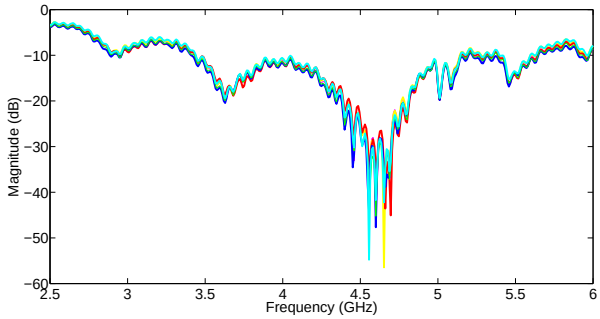

(b) 10 psu

Fig. 5.11: A comparison of the $|S_{11}|$ measurement between the container having 5 psu and 10 psu. The lines on each plot represent the measurements at different locations within the respective container. As can be seen, the $|S_{11}|$ in both are similar. The thickness of the ice in both are greater than the expected penetration depth of the antenna.

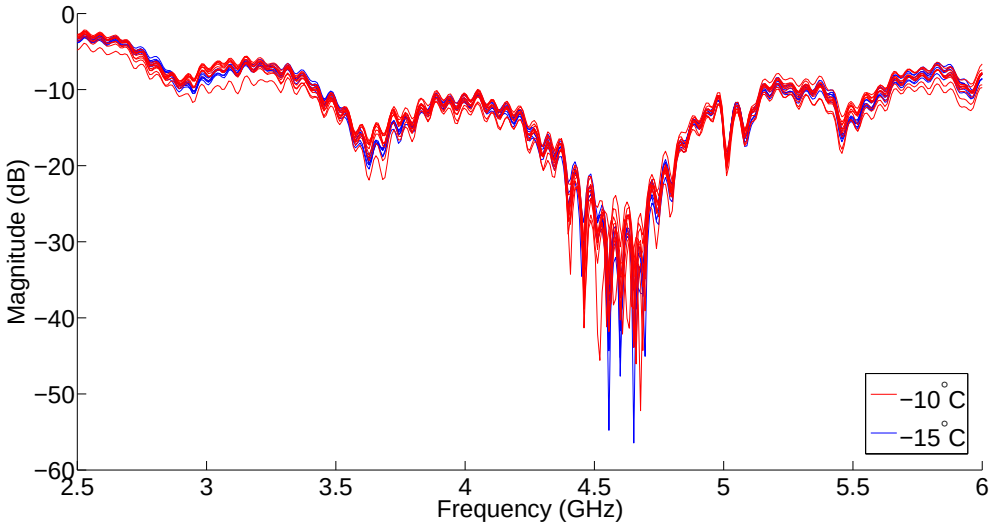

Fig. 5.12: The $|S_{11}|$ measurement of the 10 psu container for $-10°C$ and $-15°C$.

5.2.2 Ice Growth at $-5°C$

The final cold lab experiment was performed at $-5°C$. With this phase we collected time series $|S_{11}|$ measurements over four days. The first set of measurements were taken one day into this experiment on June 7$^{\text{th}}$. At the time, only three of the four containers had ice thick enough to support the antenna. As with the previous experiments, ten measurements were taken per tank. There were not noticeable differences within each container. However, we observed significant changes in the $|S_{11}|$ measurements between the three containers, as shown in Figure 5.13. At the time of the measurements, the thicknesses of the ice were 2 cm, 1.4 cm, and 1 cm from lowest to highest salinity containers respectively. The temperature of the ice surface in each container was approximately $-1°C$. If we focus on the 0 and 5 psu containers, Figure 5.9 shows that the change in permittivity is within ± 1 at this temperature and low salinity values. From this, we can speculate that the "compression" of our bandpasses in the $|S_{11}|$ are primarily caused by the different thicknesses. We note that the 10 psu container would have a larger permittivity than the other two containers. Over the following three days, we observe the $|S_{11}|$ in each container converging to the same values

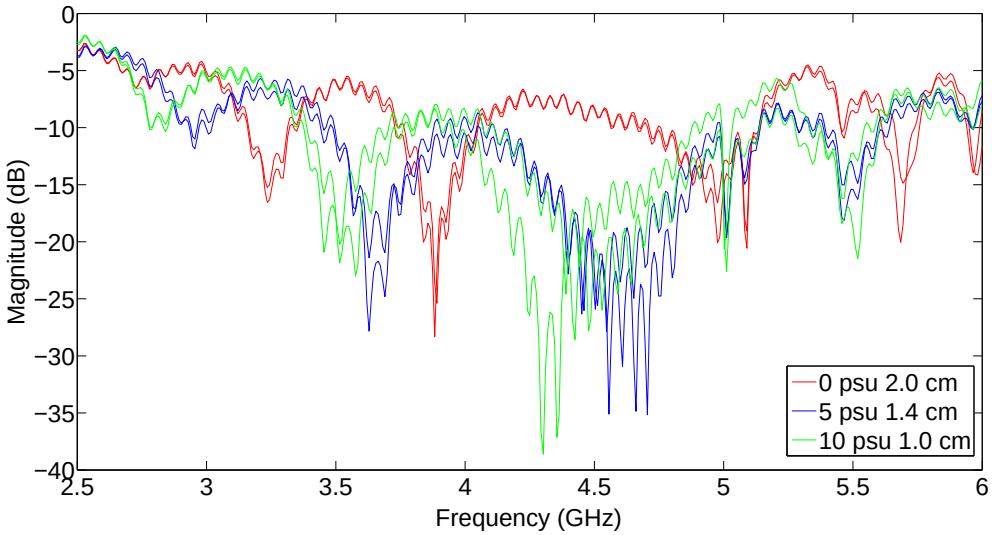

Fig. 5.13: The $|S_{11}|$ measurement between the 0 psu to 10 psu containers on June 7$^{\text{th}}$, 2016.

as the thickness becomes greater than the penetration depth, the final day's results are shown in Figure 5.14. On the final day, we collected two 5×5 cm^2 rectangular ice cores in order measure the salinity of the ice. We found the average ice core salinity in the different containers to be 0 psu, 2.05 psu, 4 psu, and 4.7 psu. It should be noted that the water in the saline ice still moved freely throughout the ice layer. During collection, some of this encapsulated water drained from the core, thus reducing the brine content of the ice.

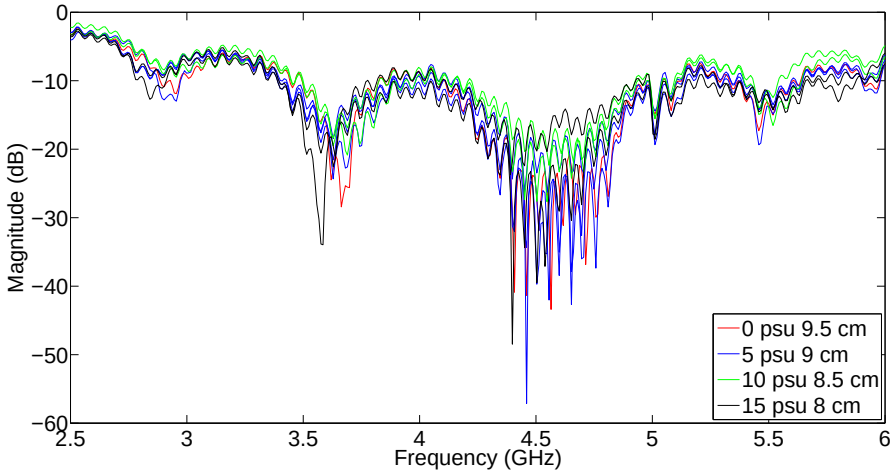

Fig. 5.14: The $|S_{11}|$ measurement between the 0 psu to 15 psu containers on June 10$^{\text{th}}$.

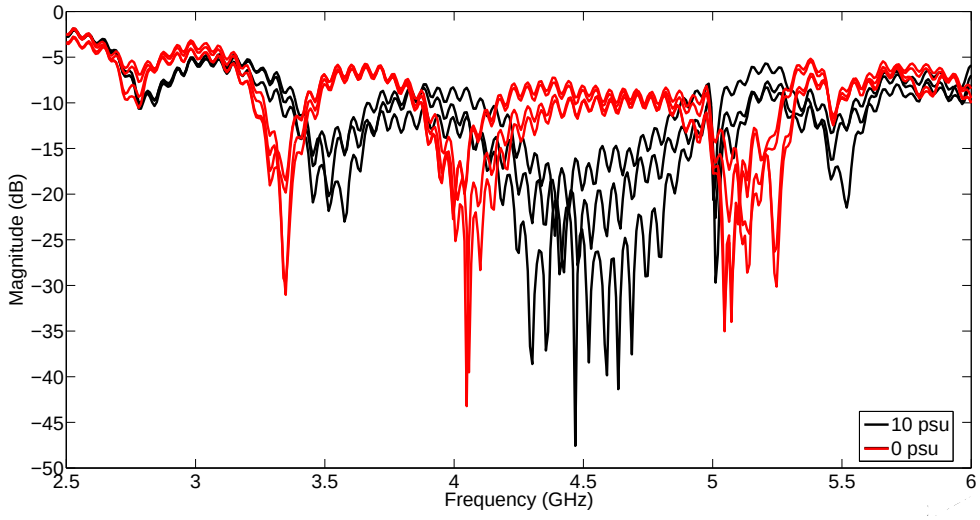

Fig. 5.15: The $|S_{11}|$ measurements of the 0 psu container and the 10 psu container when they had a thickness of 1 cm and similar temperatures of approximately $-1^{\circ}\ C$. These results give evidence that the antenna may be more sensitive to salinity variation when the thickness is sufficiently low.

Overall, from these experiments we have observed our antenna to not be sensitive to the temperature and salinity of the sea ice within most of the measured ranges of this experiment. Rather, the thickness is what drives noticeable effects on our antenna measurements (up to the penetration depth of the antenna). However, Figure 5.15 shows the $|S_{11}|$ measurements of the 0 psu and 10 psu containers when the thickness was 1 cm and the temperature approximately $-1^{\circ}\ C$. There appears to be differences between the two containers, giving reason to believe the antenna may be sensitive to salinity when the thickness is sufficiently thin and the temperature is above $-5^{\circ}\ C$. We end this section by presenting the time series $|S_{11}|$ measurements of the pure water tank, shown in Figure 5.16. This figure clearly demonstrates the effects thickness has on the antenna.

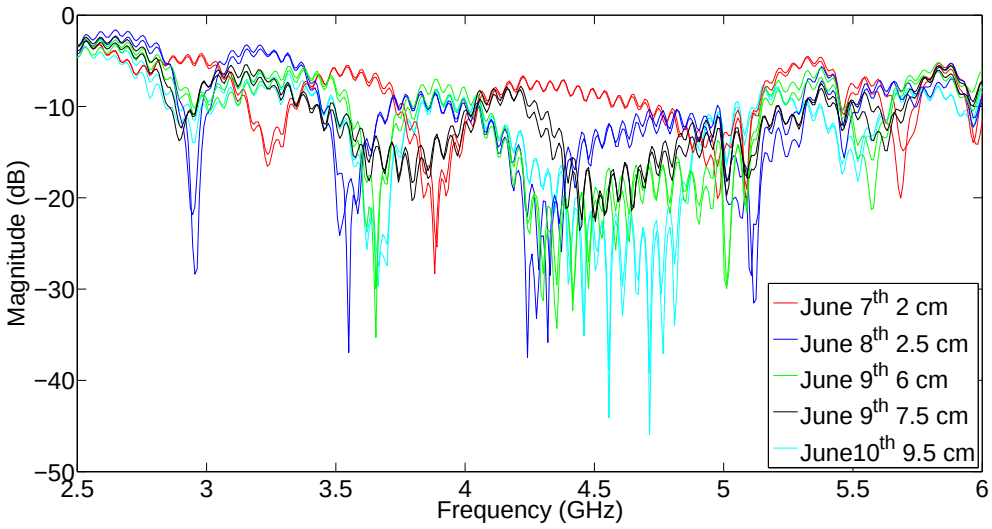

Fig. 5.16: The time series $|S_{11}|$ measurements of the 0 psu container from June 7^{th} to June 10^{th}.

6

Data Processing and Forward Solver

The importance of this chapter is to process the measured data into usable information for evaluating the inversion algorithm. Since we need to verify that our inversion method produces adequate results, we require a validation set of data. That is, we require a known set of χ with their associated S_{11} data. For this research, our model parameters are given by

$$\chi = [\ \boldsymbol{\epsilon}'\ \ \boldsymbol{\epsilon}''\ \ l\ ] \tag{6.1}$$

where $\boldsymbol{\epsilon}'$ and $\boldsymbol{\epsilon}''$ make up the complex permittivity of each ice layer (real and imaginary parts), and l is the thickness for each sea ice layer. If there is more than one layers, $\boldsymbol{\epsilon}'$, $\boldsymbol{\epsilon}''$, and l will be vectors of appropriate size. Therefore, we generate a set of χ^{true}, based on our physical samples, to be used to verify our model.

After creating our validation set of data, this chapter will present a transmission line based forward solver used for a single and multi-layered medium. This forward solver does not

fully represent the true physical nature of our system. Therefore, a calibration technique is introduced in an attempt to relate the transmission line model with the true physical model.

6.1 Dielectric Profile of SERF Measurements

The information collected at SERF in 2015 included salinity profile, temperature profile, thickness, and multi-frequency S_{11} measurements of sea ice. Using the equations from Section 2.2.3, the complex permittivity of the sea ice was calculated for the full frequency range based on the measured salinity and temperature values. The spherical inclusion equations were used based on observations of the extracted ice cores. The calculated time-series complex permittivities of the sea ice layers are given in Figure 6.1.

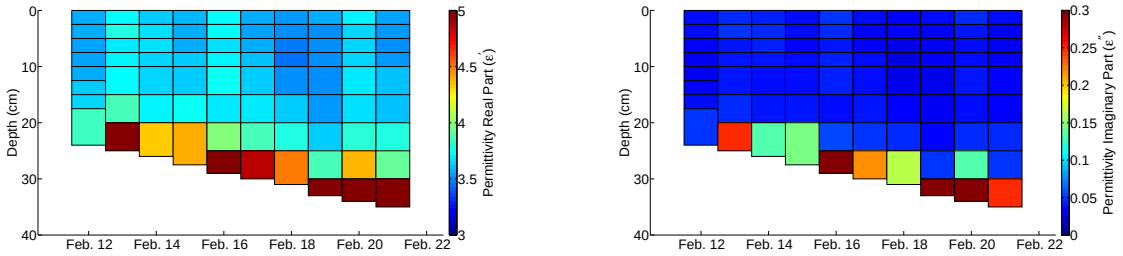

(a) (b)

Fig. 6.1: The time-series complex permittivity and thickness of sea ice at SERF 2015.

We observe that ϵ'' was relatively low and constant over time in the upper layers as opposed to the bottom layers. This is due to the the warmer temperatures at the bottom of the ice and the fact that the sea water permeates into the bottom layers replenishing brine content. The real part, ϵ', follows this same trend as ϵ''. However, the surface temperature causes more temporal variation.

The model can handle arbitrary number of layers. However, as the number of layers in-

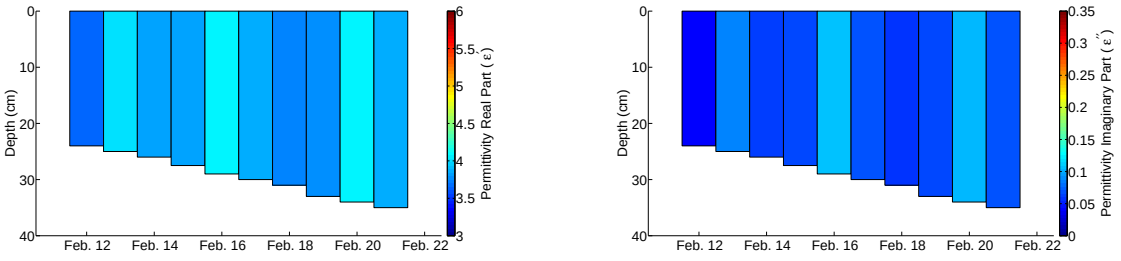

(a) (b)

Fig. 6.2: Modified single layer time-series complex permittivity and thickness of sea ice at SERF 2015.

creases, the number of unknown model parameters will increase. Given the limited measured data points, we have to limit the number of layers. Therefore, in this thesis we consider a single and three layered model for our inversion algorithm. When developing a reconstruction method, it is important to know whether or not the method converges to the correct parameters. To this end, we needed to generate the true model parameters for a single layer and three-layered medium, shown in Figure 6.2 and Figure 6.3. To do this, we calculated bulk complex permittivities based on the the raw permittivity measurements. For the three-layered model, each layer is assumed to have equal thickness so as to reduce the number of unknowns. It should be noted that actual sea ice is not necessarily a layered medium, with each layer having a homogeneous complex permittivity. In fact, there are typically no distinct boundaries between layers, as the permittivity transitions continuously throughout the profile. The fact that we represent an actual sea ice as a single-layer or three-layered medium can be considered as one method of parameterizing the actual medium. Regarding the usefulness of a single layer model, it should be noted that in a recent work, we have considered the sea ice as a single layer (half space), and reconstructed its effective complex permittivity. This was used as a binary detection strategy for the presence or absence of oil spills in the sea ice profile [47].

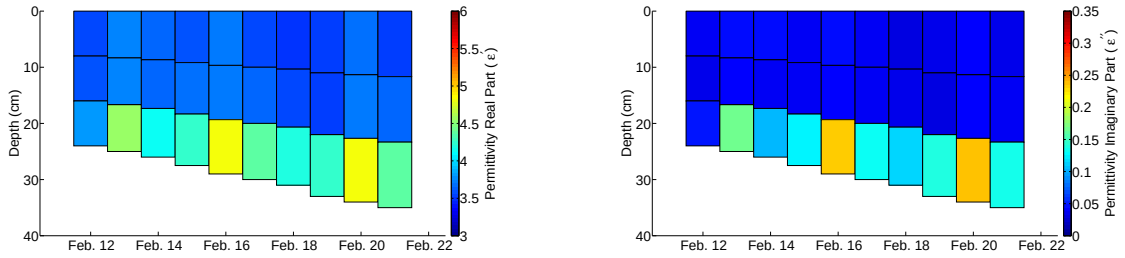

(a) (b)

Fig. 6.3: Modified three-layer time-series complex permittivity and thickness of sea ice at SERF 2015.

6.2 Transmission Line Based Forward Solver

As noted above, sea ice may be modeled as a multi-layered lossy dielectric. In our forward solver, we model each layer as a transmission line having a complex characteristic impedance, $\eta(\epsilon', \epsilon'')$, as shown in Figure 6.4[1]. The antenna is the source of energy for this system, and herin is modeled by a voltage source with an impedance of Z_g, which will be explored in Chapter 7. The load terminating the last layer, Z_w, is the sea water beneath the sea ice. Using the center frequency of 4 GHz, The complex permittivity of the sea water is taken as $60 - j40$, based on values from Figure 2.3.[2] Although the framework has the

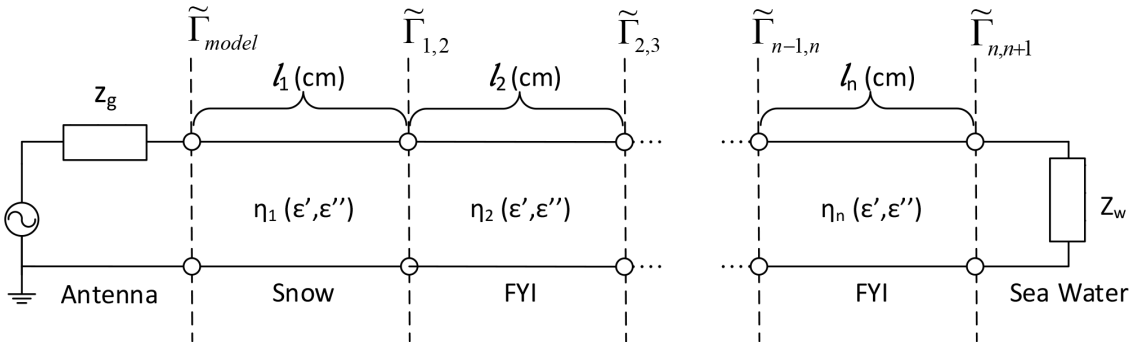

Fig. 6.4: Transmission line model of an antenna situated on snow-covered FYI.

[1] This model has the potential to accommodate snow layers situated on top of the sea ice.

[2] The complex permittivity of sea water does vary with frequency. However, by selecting a single value we reduce the computation cost per iteration. As well, the sea water permittivity is much higher than the sea ice causing a large reflection (almost like an open load). The effects of a slight change in the sea water complex permittivity are taken to be negligible.

potential to be applied to different forms of sea ice, we only consider FYI in this thesis. We further assume that the FYI is isotropic. The assumption of isotropy is based on the brine and air inclusions being randomly orientated in the medium. If the inclusions were not random, then a tensor of permittivities would be needed. Of course, the model presented in Figure 6.4 assumes that the antenna, in terms of $|S_{11}|$, "sees" the water layer. If the antenna does not see the water layer, due to increased thickness or attenuation, then we can consider the transmission line to be terminated with a half space of ice.

The relationship between χ and the generalized Fresnel reflection coefficient $\widetilde{\Gamma}_{model}$ will now be formulated. In a transmission line setting, the generalized Fresnel reflection coefficient at a boundary can be found as [18]

$$\widetilde{\Gamma}_{i,i+1} = \frac{\Gamma_{i,i+1} + \widetilde{\Gamma}_{i+1,i+2} e^{-2j\gamma_{i+1} l_{i+1}}}{1 + \Gamma_{i,i+1} \widetilde{\Gamma}_{i+1,i+2} e^{-2j\gamma_{i+1} l_{i+1}}} \tag{6.2}$$

where $\widetilde{\Gamma}_{i,i+1}$ is composed of the Fresnel reflection coefficient $\Gamma_{i,i+1}$ at the boundary and the generalized Fresnel reflection coefficient $\widetilde{\Gamma}_{i+1,i+2}$ at the subsequent boundary. This function states that the reflection at a boundary is also dependent on the reflection at the next boundary. The equation (6.2) can be called recursively for a multi-layered material with the reflection at the load (sea water or half space) being the stopping criteria. Since there is no subsequent layer, the total reflection at the load is assumed to have only an initial reflection. That is, the waves that transmit into the sea water do not reflect back. The Fresnel reflection coefficient at a boundary is defined by

$$\Gamma_{i,i+1} = \frac{\eta_{i+1} - \eta_i}{\eta_{i+1} + \eta_i} \tag{6.3}$$

where η, defined by (2.11), is the characteristic impedance of the material on either side of the boundary.

6.3 Cost Function and Modeling Error

The cost function compares the measured data, S_{11}, and modeled reflection coefficient $\widetilde{\Gamma}^{mod}$. The cost function is given by

$$C(\chi) = \sum_{n=1}^{nf} W_n \cdot \frac{\left| |S_{11,n}| - |\widetilde{\Gamma}_n^{mod}(\chi_n)| \right|^2}{|S_{11,n}|^2} \tag{6.4}$$

where nf is the number of frequency measurements, $S_{11,n}$ is the measured S_{11} at the nth frequency, W_n is a weighting function, and $\widetilde{\Gamma}_n^{mod}(\chi)$ is the the reflection coefficient found from the forward model at the nth frequency due to the predicted unknown parameters χ. In this thesis, we investigated different weighting functions. However, none of them yielded better results than $W = 1$. It should be noted that in a co-resident multi-sensor system, some sensors might collect more informative data about the region of interest. In that case, a more sophisticated choice of W_n can be very useful. However, we deal with a single sensor system, therefore the choice of $W_n = 1$ may be sufficient.

We now discuss the challenges associated with optimizing this cost function. The main challenge is the discrepancy between the actual wave propagation within the sea ice and the simplified model (transmission line) used in our forward solver. This discrepancy is often referred to as the modeling error. The presence of modeling error in the optimization results in not converging to an appropriate solution. (In the next section, we discuss how to alleviate this modeling error using data calibration techniques.) Herein, we elaborate on the disadvantages of a full-wave forward solver for our system. To this end, let's assume a full-wave forward solver is to be used. In addition to being computationally expensive, the use of a full-wave forward solver increases the number of unknowns to be reconstructed. For example, if a full-wave forward solver is to be used, we need to reconstruct for the three components of the electric field as well as the complex permittivity at different locations

within the domain of interest. This increase in the number of unknowns require more data collection so as to maintain a reasonable balance between the number of known and unknown quantities. However, the increase in the number of measured data is not trivial for Arctic remote sensing applications. For example, in our system, it is not feasible to collect the electric field measurements within the sea ice; we are restricted to only a single position directly above the domain of interest. Last but not least, herein, we consider phaseless data. The inversion of phaseless data is often more complicated than amplitude-and-phase data and makes the problem more nonlinear [48].

6.4 Data Calibration

This remainder of this section looks to address the inherent discrepancy between the measured and modeled $\widetilde{\Gamma}$ and to propose a way to link the two. The largest source of error is caused by modeling a near field measurement with a transmission line approach.

The transmission line model is based on plane wave interactions within a layered media. This means that we do not consider the electric fields polarized in the direction of wave propagation. However, in Section 3.6.2, the OEW's near-field was simulated when placed on snow-covered sea ice. The results, shown in Figure 6.5, demonstrate the presence of E-fields in the direction of propagation. The snow/ice boundary is easily identifiable at 7.5 cm from the normal component of the E-field. Therefore, the presence of the normal E-field in the actual propagation, and its absence in the transmission line model, is a source of modeling error.

We attempt to address this modeling error by using a calibration factor. The purpose of this calibration factor is to convert measured $\widetilde{\Gamma}$ data into our modeled $\widetilde{\Gamma}$. Assume we want to

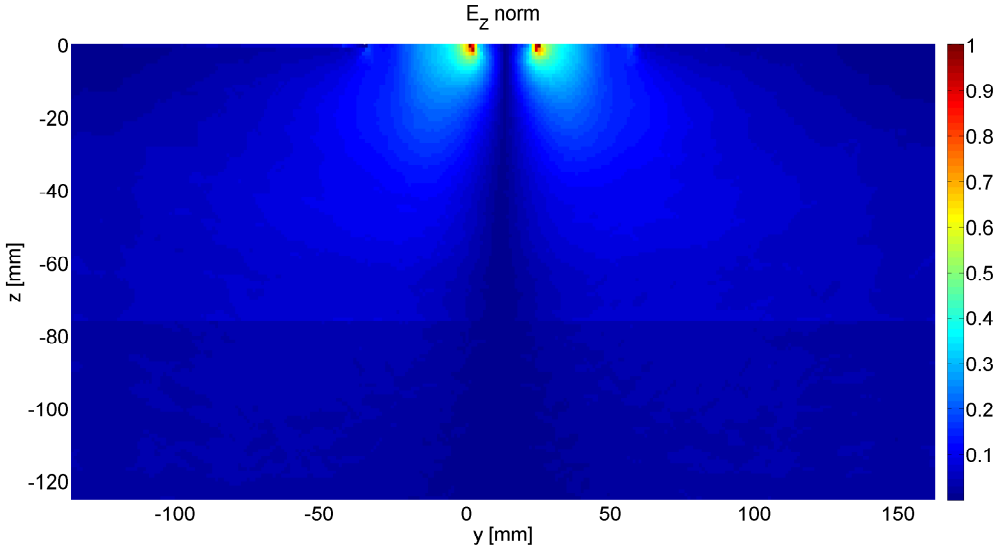

Fig. 6.5: HFSS simulation of the E_z component in the E-plane when placed on snow-covered sea ice. The transmission line model inherently neglects these fields.

minimize the following L^2-norm data misfit cost function,

$$\min_{wrt\,\chi} \parallel P(\chi^g) - T(\chi) \parallel \tag{6.5}$$

where P is the true relationship between model parameters and the measured data, and T is our transmission line based forward solver operator that takes χ and outputs the simulated data. As well, χ^g are the true model parameters and χ are an arbitrary set of model parameters. We want to minimize (6.5), with the resulting χ to be equal to χ^g. However, P is an unknown complex operator and is a different operator than T, due to the modeling errors. This difference would cause $T(\chi)$ to optimize to $P(\chi^g)$, not necessarily resulting in χ approaching χ^g. In order to better relate the true model to the predicted model, so as to reduce the modeling error, we propose to minimize the following cost function instead of (6.5)

$$\min_{wrt\,\chi} \parallel P(\chi^g)\frac{T(\chi^{cal})}{P(\chi^{cal})} - T(\chi) \parallel \tag{6.6}$$

where χ^{cal} is a known calibration object and $P(\chi^{cal})$ is the corresponding measured data

collected from this known object. In addition, $T(\chi^{cal})$, is the simulated data due to this known object based on the transmission line model. Now, assuming that the calibration object is similar to the actual unknown χ, we can understand how (6.6) can help us alleviate the modeling error. To this end, for simplicity, let's assume the limit of $\chi^{cal} \rightarrow \chi^{g}$. In that case, $P(\chi^{g})$ will be canceled by $P(\chi^{cal})$, and (6.6) simplifies to

$$\min_{wrt\ \chi} \parallel T(\chi^{g}) - T(\chi) \parallel . \tag{6.7}$$

It is obvious that the solution of (6.7) is $\chi = \chi^{cal}$. However, since we have chosen $\chi^{cal} \rightarrow \chi^{g}$, the solution will be in fact $\chi = \chi^{g}$, *i.e.*, χ converges to the true solution. In practice, since χ^{g} is unknown, it is not possible to ensure that χ^{cal} is close to χ^{g}. In such cases, we need to do our best to choose a χ^{cal} that is sufficiently close to χ^{g}. This process has the potential to alleviate the modeling error. The above procedure is inspired by the scattered field calibration technique, which is used in microwave tomography [49].

For our application we have an advantage for choosing χ^{cal}. Since we are performing time-series measurements, and have the potential for high temporal resolution (time interval between two successive measurements are small), it is expected that χ does not vary substantially between two successive measurements. For example, the SERF 2015 time series profile of the ice do not substantially change between the two days. The largest change in the properties is the thickness (1 cm to 2 cm growth). To this end, we can start by physical sampling at a given time, and use this physical sample as the calibration object to calibrate the $|S_{11}|$ data in subsequent measurements.

Finally, it should be noted that other simpler forms of calibration techniques can also be investigated and utilized for this application. In addition to a point to point calibration described above, we can look towards using key indicators or features between successive

measurements to reconstruct χ. For example, for applications in which the complex permittivity of the region of interest does not vary much, the main valley (resonance) of the $|S_{11}|$ measurements can serve as this key indicator. In such cases, calibration factors such as the ratio of the main resonance frequency in the simulated model corresponding to χ^{cal} to that of the measured data collected from χ^{cal} can be investigated.

7

Inversion Results

The final component for this research is developing an inversion algorithm to solve for the complex permittivity of sea ice given a set of measured $|S_{11}|$. We begin by developing a single and three-layered inversion solution to a given set of simulated S_{11}[1], with no modeling errors. That is, the forward solver discussed in Chapter 6 was used to generate the data. Noise will then be added to the simulated data to observe the effects it has on our solutions. Afterwards, we will utilize a calibration technique to reduce the modeling error between the forward solver and measurements collected from SERF 2015. The results of this calibration factor will be discussed.

We begin this chapter by presenting a more detailed flow chart of the inversion process, shown in Figure 7.1. In our method we use a time series approach in order to develop our initial model parameter states. In practice, at the time of antenna deployment, a physical

[1] These transmission line models are capable of using both the magnitude and phase of the S_{11}. However, as previously discussed, we consider inversion of phaseless data since phaseless data is more robust, more affordable to collect, and we also think our phase measurements are not reliable.

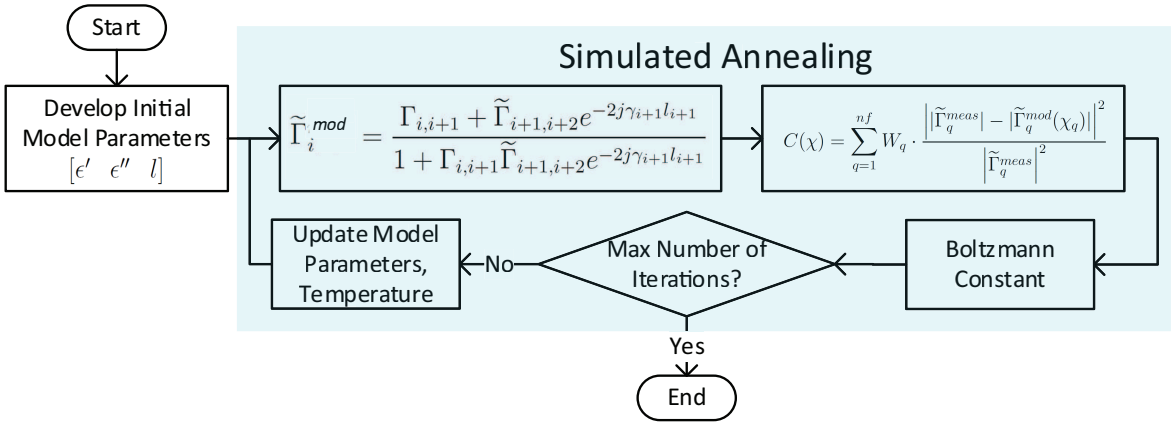

Fig. 7.1: A flowchart of the iterative inversion method. After choosing initial model parameters, we calculate our response from our transmission line model, determine the error (cost), and then update our parameters using simulated annealing.

sample will be taken nearby in order to determine our initially known set of complex permittivities. In addition, an $|S_{11}|$ measurement would be performed which would be used in the calibration technique. We use the transmission line based forward solver and a normalized cost function for all algorithms developed in this chapter. A weighted normalized cost function will be discussed when inverting the SERF 2015 data.

Simulated annealing is the global optimization technique developed to traverse the nonlinear search space of our forward solver. We explore different cooling schedules and their effect on our solution. How we update and perturb our model parameters will also be discussed.

Finally, the proposed algorithm is intended to run for a large number of iterations. Therefore, each iteration should not take a long time to complete. A huge time sink would be to calculate the complex permittivity at each frequency for every iteration. One method to eliminate this problem is to use a single complex permittivity for all frequencies.

The solution we came up with was to create a set of ratios that could be applied to a single frequency in order to create the complex permittivity at all frequencies between 3 GHz and

6 GHz. Using the equations from Section 2.2.3.2, the complex permittivities were calculated for different salinity (4 psu to 12 psu) and temperatures ($-12^{\circ}C$ to $-3^{\circ}C$) between 3 GHz and 6 GHz. We then divide the values by the initial value at 3 GHz. Figure 7.2 shows the ratios found for ten different configurations of temperature and salinity. As can be seen, the complex permittivities follow a distinct trend regardless of initial temperature and salinity values. Therefore, we can use the average ratio values in our algorithm to reduce computation time per iteration. In addition, this is even more important to increase the number of data points as compared to the number of unknowns. If we consider χ at each frequency to be completely independent, performing multiple-frequency measurements will not be useful. Based on this, we can always have one set of main unknowns at the initial frequency, say 3 GHz.

The unknown parameters at other frequencies will be related to the unknowns at this initial frequency through an operator, say $\mathcal{L}_q$, which takes the unknown parameters at that specific frequency and then transforms it to the unknown parameters at the qth frequency. Figure 7.2 is essentially the representation of this operator. Therefore, the cost function shown in Figure 7.1, can be written as

$$C(\chi) = \sum_{q=1}^{nf} W_q \cdot \frac{\left| |\widetilde{\Gamma}_q^{meas}| - |\widetilde{\Gamma}_q^{mod}(\mathcal{L}_q(\chi))| \right|^2}{\left| \widetilde{\Gamma}_q^{meas} \right|^2} \tag{7.1}$$

where χ represents the unknown parameters at one specific frequency. Of course, for $q = 1$, $\mathcal{L}_q$ will be the identity operator; *i.e.*, $\mathcal{L}_q \equiv \mathcal{I}$.

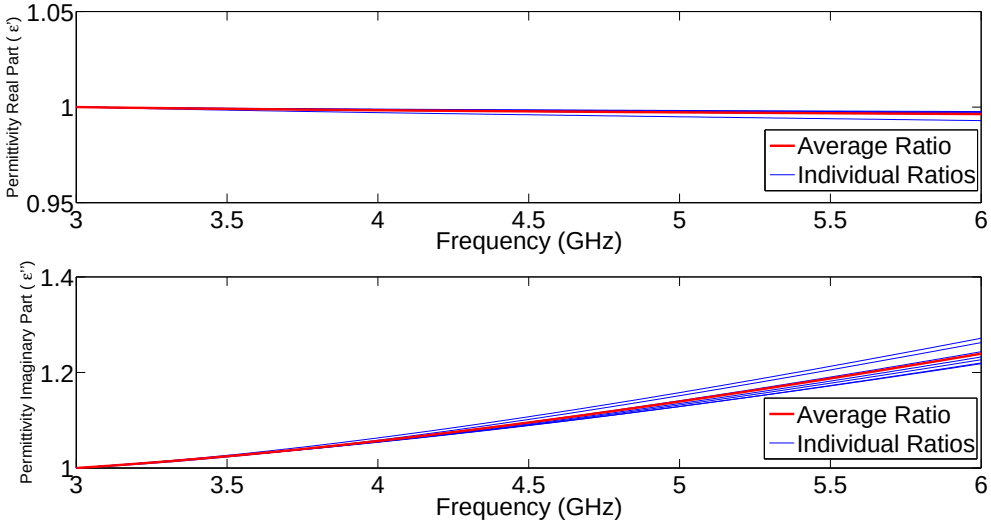

Fig. 7.2: Frequency dependence of sea ice complex permittivity for multiple configurations of temperature and salinity.

7.1 Synthetic Data Inversion

This section discusses and presents inversion results from our single and three layer model using noiseless and noisy synthetic data. We begin by developing inversion algorithms capable of reconstructing the complex permittivity and thickness of a single layer and three layer of sea ice based on synthetic multi-frequency $|S_{11}|$ data from 3 GHz to 6 GHz. This data is related to our model parameters by our transmission line model. To be comparable to the VNA measurements, the frequency step size is 15 MHz, resulting in 201 datum. The cost function used is given in (7.1). It is important to note that our cost function for a single or three layer model is still highly non-linear with many local minima. To this end, a directive search is considered rather than an exhaustive search.

Now that we have identified our problem and relevant information, we look to construct a global optimization algorithm capable of reconstructing these profiles. When creating a method it is important to note what level of accuracy or error we deem acceptable. We are using a model that does not accurately describe the true physics of the system. Our true set

of model parameters are based on physical samples. These physical samples have a degree of error to them. As well, we collect bulk measurements, when we know that the sea ice has a continuous profile. Finally, we use empirical formulas to relate the physical properties of the sea ice to the complex permittivity. Just from these observations, we can expect some inaccuracy within our solution. Since we are reconstructing a time series profile of sea ice growth, if our solution follows the general trend of the true values, we label it as a success at this initial stage in algorithm development. With this being said, we still want to generate a solution as close to the true model parameters within a reasonable computation time.

We can consider the complex permittivity profile of sea ice at each point in time to require its own independent inversion. That is, we do not consider any algorithm that simultaneously utilizes more than one temporal measurement, *e.g.*, curve smoothing or interpolating of the final trend line. However, for each individual inversion, we use the previous time's solution as the initial model parameters (except the first measurement). As well, we use our knowledge and observations of ice growth to reduce the search space and to determine the amount of perturbation per iteration. In other words, our inversion algorithm simultaneously invert the muli-frequency data at a given time to reconstruct the respective χ. Then, this reconstructed χ is used as the initial guess for the inversion algorithm to invert the multi-frequency data at the next time step.

7.1.1 Single Layer Algorithm

In this section, we present results for the single layer algorithm using noiseless and noisy synthetic data. In this model, our three model parameters are thickness, the real part of permittivity, and the imaginary part of permittivity.

The first stage of our inversion development did not consider noise associated with the true

Tab. 7.1: Simulated annealing parameters for a single layer noiseless inversion.

Parameter	Value
N	250
L	100
P_s	0.5
P_f	10^{-2}
R	10

data. For our simulated annealing algorithm, we utilized the cooling schedule outlined in Section 2.3.5.2. The free parameters we controlled included N, L, P_s, P_f, and R. The values we ultimately chose are given in Table 7.1. We note here that we found that the value of Z_g in our forward solver model did not make our algorithm perform better or worse. Therefore we chose a standard $50\ \Omega$ value for its impedance.

From testing, we found that we produced the best results when we had a high number of resets, R. As well, it allowed us to keep the number of temperature, and equilibrium iterations low. We experimented with a low number of resets and a higher number of N and L (1500 and 250, respectively) and found the results not as consistent. That is, we observed that the algorithm would not find a reasonable solution sometimes. As well, we tried even larger values (10000 and 2000) which resulted in slightly more accurate solutions, but the computation time was long (hours) whereas the final values resulted in under a minute per temporal measurement.

When we reset our cooling schedule, T, N, and L reset, making it easier to jump out of local minima. As well, at the time of each reset, we choose our initial model parameters to be equal to the absolute best solution from the previous cooling schedule. That way we retain information from previous resets. There are two sets of model parameters stored: the absolute best solution (lowest cost) and the currently accepted solution (we don't want to start each iteration at the best solution in order to avoid stagnation). Now with each reset, we keep the same start and finish temperatures. However, the probability of keeping a worse

solution at the start of the first iteration compared to the tenth will not be the same. This is due to the running average of accepted cost values that is kept track of in the Boltzmann Constant.

The last aspect of our algorithm that we will mention is the adaptive perturbation method used. Simply speaking, we use a Monte Carlo approach by randomly varying the parameters. We do this by adding or subtracting a random value from the currently accepted model parameter. The amount of this value decreases proportional to R. We decrease the amount of perturbation as the algorithm progresses in order to reduce the number of wasted iterations. Since we are only optimizing three parameters, we varied all three in each iteration. In the three layer model we do not vary every parameter. It is important to note that we do not set a boundary limitation on any of the parameters; there is potential for parameters to approach infinity.

The results for a noiseless set of data for a single layer of sea ice are presented in Figure 7.3 to Figure 7.5. These results are based on an average of three trial runs. As can be seen, for all three parameters the algorithm is able to follow the general trend of the true parameters.

Afterwards, we added noise to our simulated data in order to see if the algorithm could produce similar results. In addition, the presence of noise is also important in alleviating the effect of the so-called inverse crime when the same model is used for data generation and data inversion. The noise we added to the data is given by

$$d_{noise} = d + \frac{N_s}{\sqrt{2}} \cdot max(d) \cdot Rand \tag{7.2}$$

where d is the true simulated data, N_s is the level of noise selected, and $Rand$ is a random number between -1 and 1. We chose a value of 0.5 for N_s. Figure 7.6 shows an example of

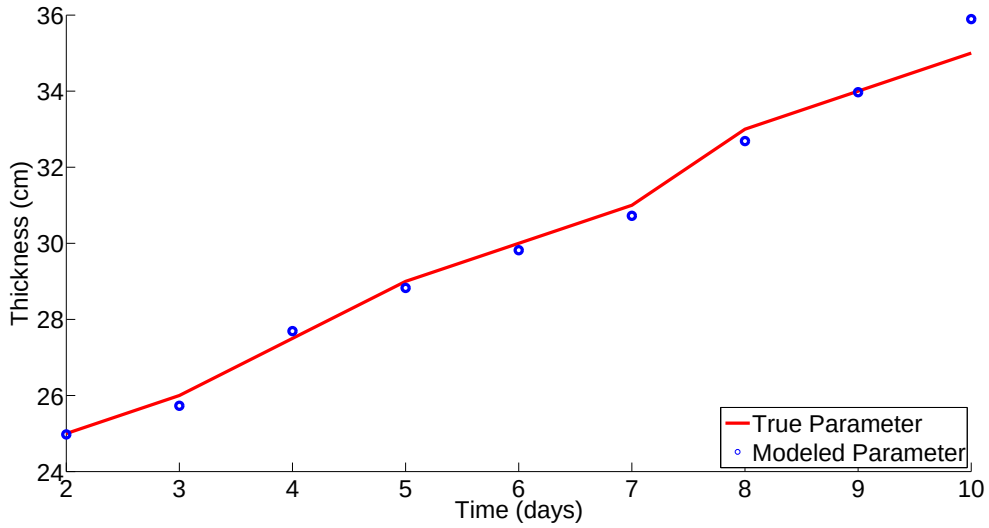

Fig. 7.3: The one layer simulated annealing results of the time series thickness using simulated data. The solid line show the true parameter, and the circles represent the reconstructed (modeled) ones.

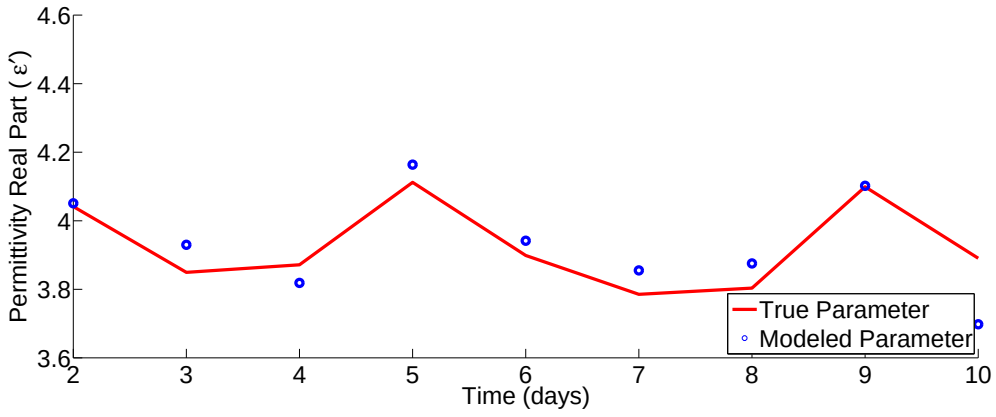

Fig. 7.4: The one layer simulated annealing results of the time series real part of permittivity using simulated data.

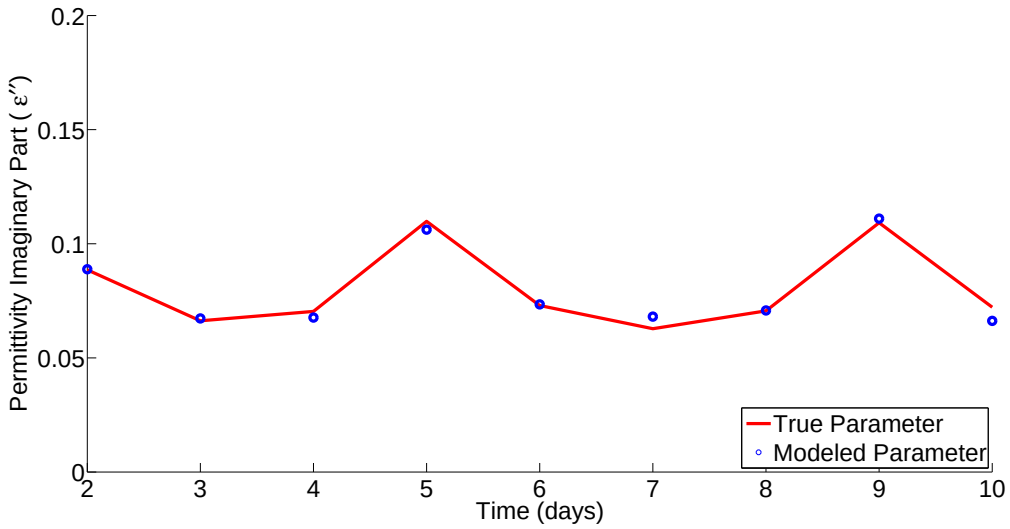

Fig. 7.5: The one layer simulated annealing results of the time series imaginary part of permittivity using simulated data.

the noise overlayed on a signal, represented by the red line. The green represents the output of our initial model parameters (taken from the inversion result for the previous day) and the blue line is the output of the final model parameters. We see that the predicted response is close to the simulated response. Since our simulated response and predicted response are based on the same forward solver, this is a good indication the algorithm is able to handle some noise to the data. The time series results are given in Figure 7.7 to Figure 7.9. These are average values of three different trials. It seems that the error in the reconstructed thickness corresponds to the error in the real part of the permittivity. For example, when in day 4, the reconstructed thickness is over-estimated, the reconstructed real part of the permittivity is under-estimated to compensate for the reconstructed thickness value. On the other hand, in days 6 and 7, when the thickness value is under-estimated, the reconstructed real part of permittivity is over-estimated. This can be explained by noting the non-uniqueness of the solution for this problem. The next step in the algorithm development is adding more layers, thus increasing the number of unknowns.

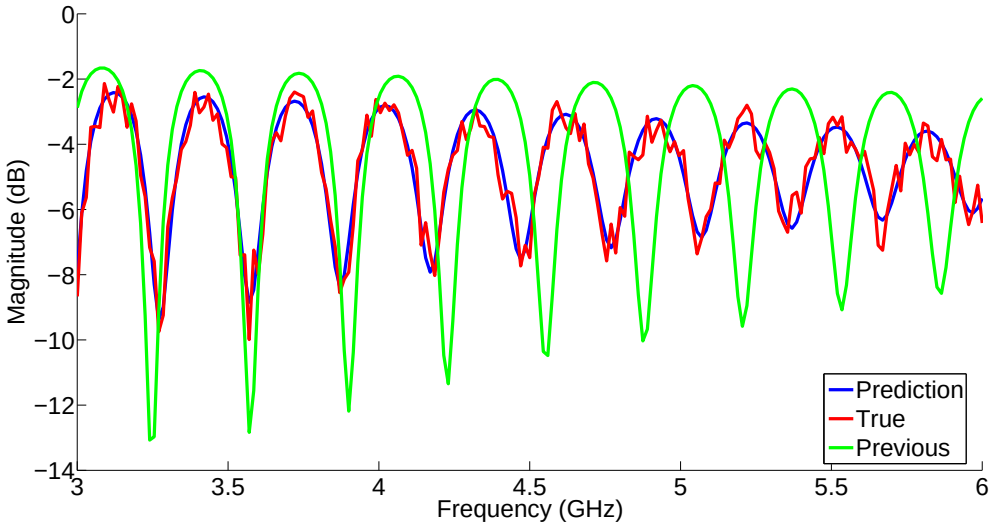

Fig. 7.6: The data (reflection coefficient) for a single layer algorithm. The green, red, and blue lines represents the previous day data, the current day's true simulated noisy data, and the predicted data for the current day, respectively.

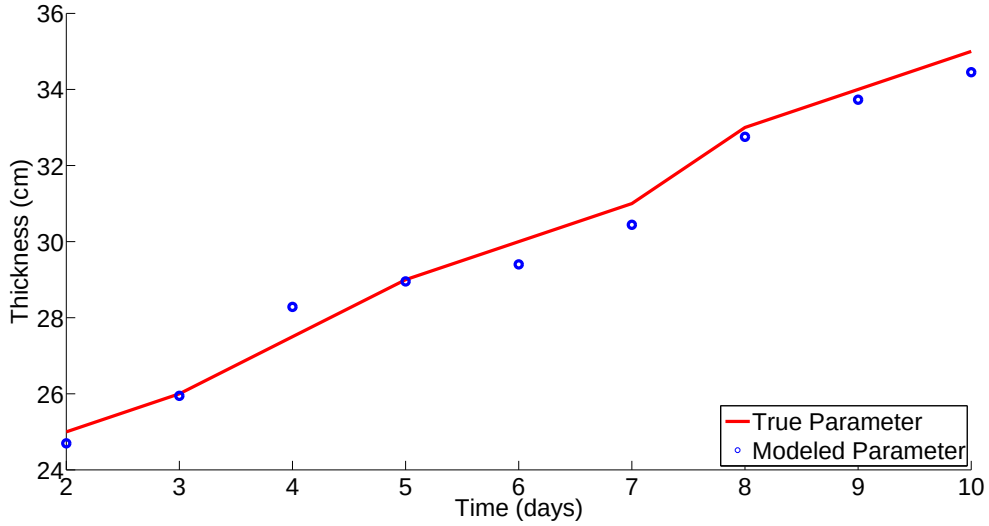

Fig. 7.7: The one layer simulated annealing results of the time series thickness using noisy simulated data.

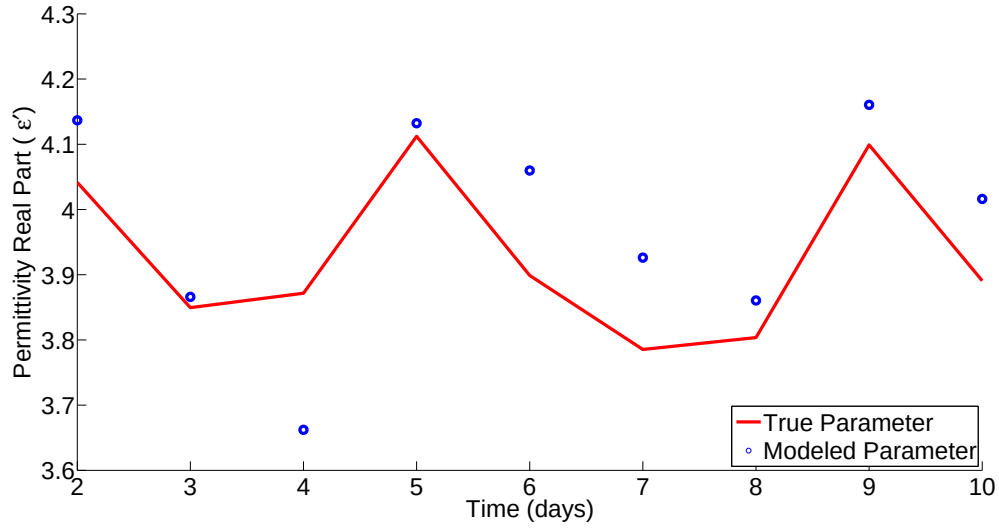

Fig. 7.8: The one layer simulated annealing results of the time series real part of permittivity using noisy simulated data.

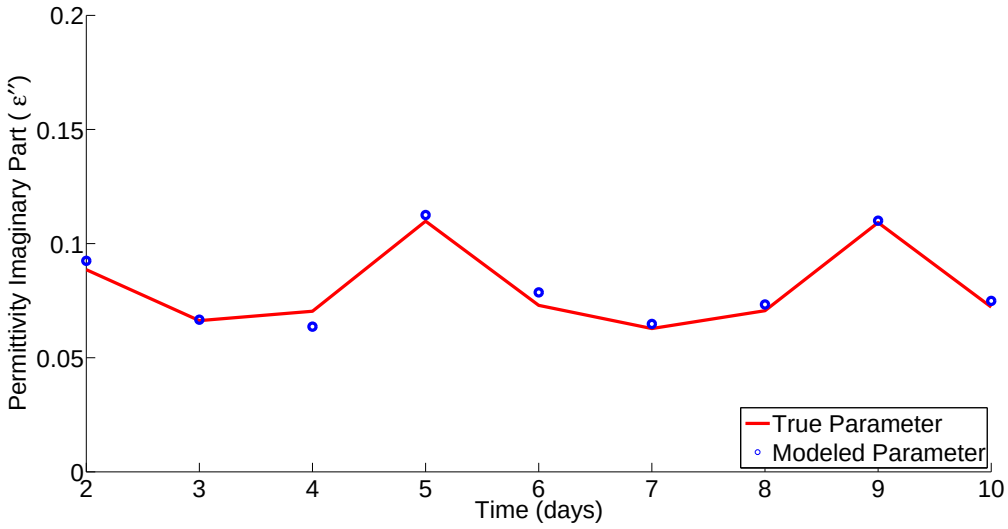

Fig. 7.9: The one layer simulated annealing results of the time series imaginary part of permittivity using noisy simulated data.

Tab. 7.2: Simulated annealing parameters for a three layer noiseless inversion.

Parameter	Value
N	150
L	50
P_s	0.5
P_f	10^{-2}
R	10
N_L	3

7.1.2 Three Layer Algorithm

The three layer algorithm is a modification of the one layer algorithm. That is, the simulated annealing algorithm has the same cooling schedule structure and performs the same tasks at each reset. Before proceeding, we remind the reader that we divide our ice into three equally thick sections. (This can be regarded as prior information used by the algorithm.) Therefore, we have only total thickness, and the complex permittivity values for each layer as the unknown model parameters. In the three layer model we therefore have seven unknowns. There were modifications made to the values of our free parameters and the way in which the perturbation occurs. The values we chose for our simulated annealing three layer algorithm are given in Table 7.2. (The values used in Table 7.1 could also be used; however, this will result in more computation time.)

We introduce a new variable, N_L, into our three layer model which indicates the number of layers we are reconstructing (three in this model). Simulated annealing typically relies on small perturbations of the model parameters. This variable is used to reduce the number of model parameters we update each iteration. For each R, we actually run through the cooling schedule three times. Initially, we vary all parameters, then reduce it to the two upper layers, and finally just the top layer is varied on the third run through. Within each cycle, we give the algorithm a random chance to modify an additional layer in order to avoid stagnation.

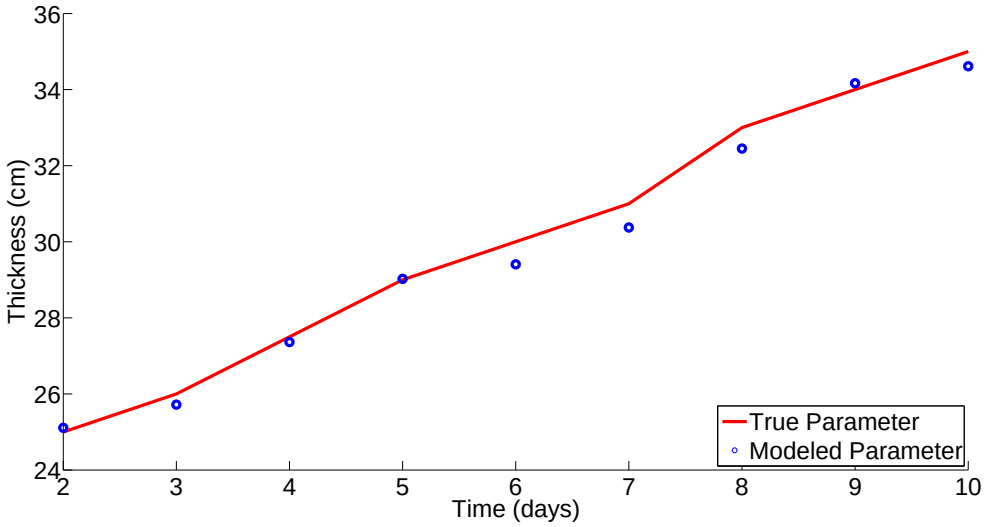

Fig. 7.10: The three layer simulated annealing results of the time series (total) thickness using noiseless simulated data.

For the noiseless case, Figure 7.10 to Figure 7.12 present the results for this algorithm. The run time for each day was approximately one minute. As we can see, the algorithm appears to follow the true values for all parameters.

We now use the same amount of noise as the noise introduced in the noisy single layer results for this three-layer example. The inversion algorithm is capable of generating reasonable results if we let the simulated annealing to run for more iterations. The values chosen for this example are given in Table 7.3. We observed that an increase in N and L gave better results than having more resets. The time series results for our model parameters are given in Figure 7.13 to Figure 7.15. As we can see, error in the reconstructed model parameters is higher than the noiseless case. However, we still follow the general trend of each model parameter. Our results are stable; we do not have any parameters approaching infinity.

Before proceeding with the final synthetic data test, we note that we had tried using a larger number of layers. What we found was that the increase in unknown model parameters caused the algorithm to not converge. Simulated annealing works well with a large number of model

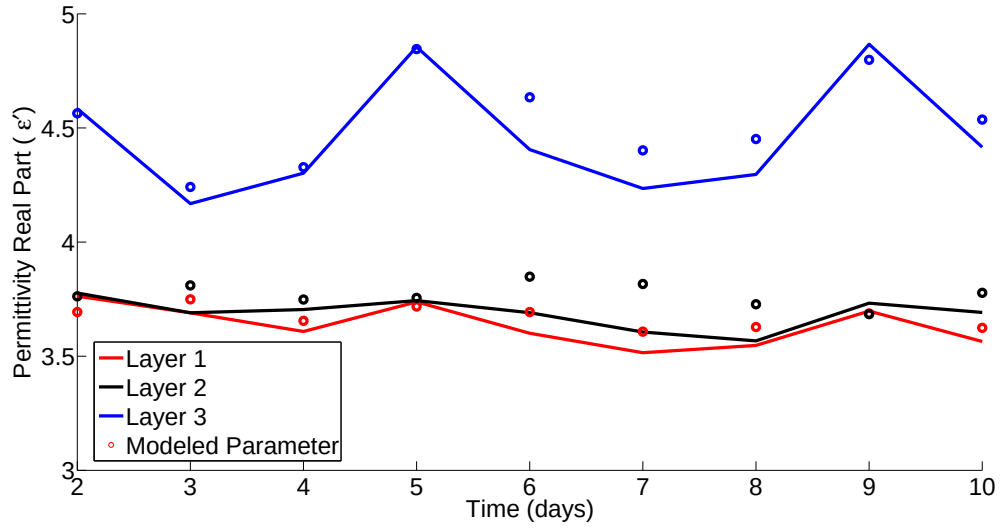

Fig. 7.11: The three layer simulated annealing results of the time series real part of permittivities using noiseless simulated data.

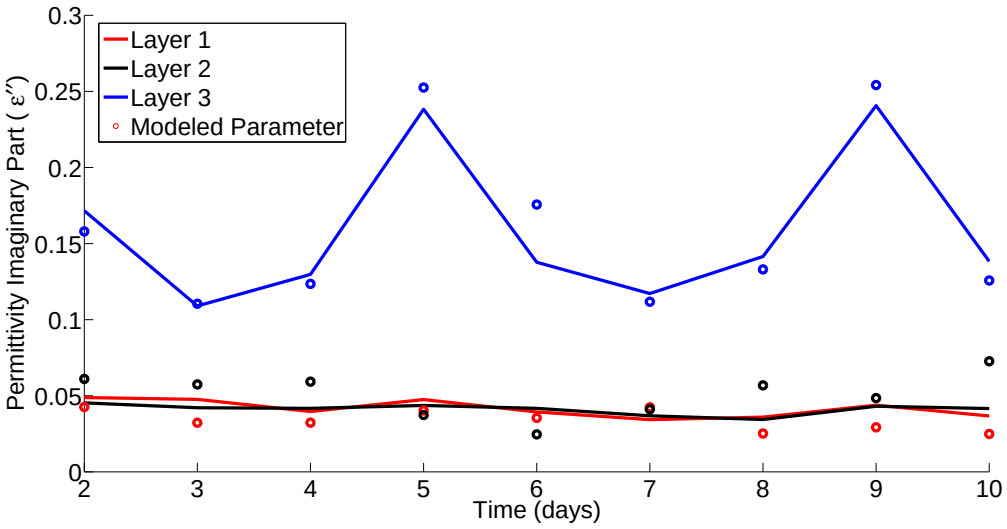

Fig. 7.12: The three layer simulated annealing results of the time series imaginary part of permittivities using noiseless simulated data.

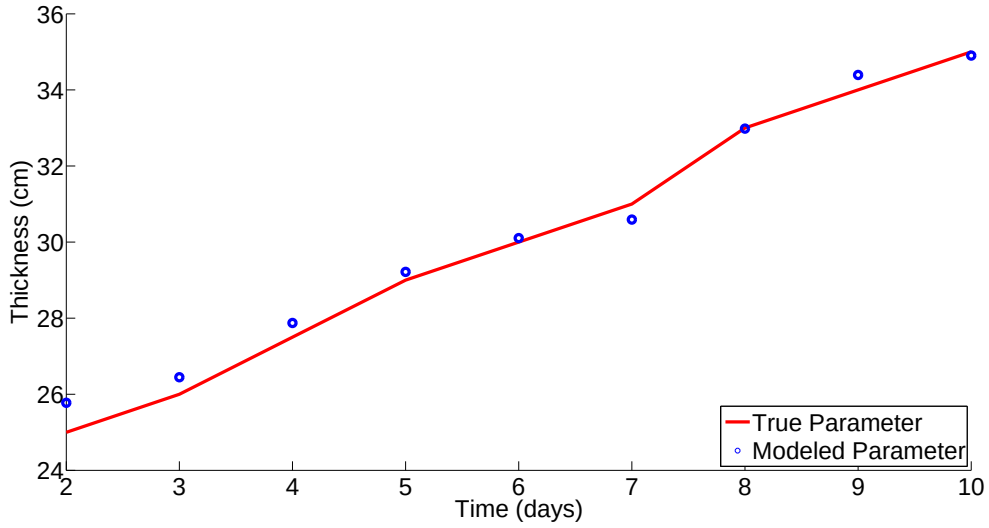

Fig. 7.13: The three layer simulated annealing results of the time series thickness using noisy simulated data.

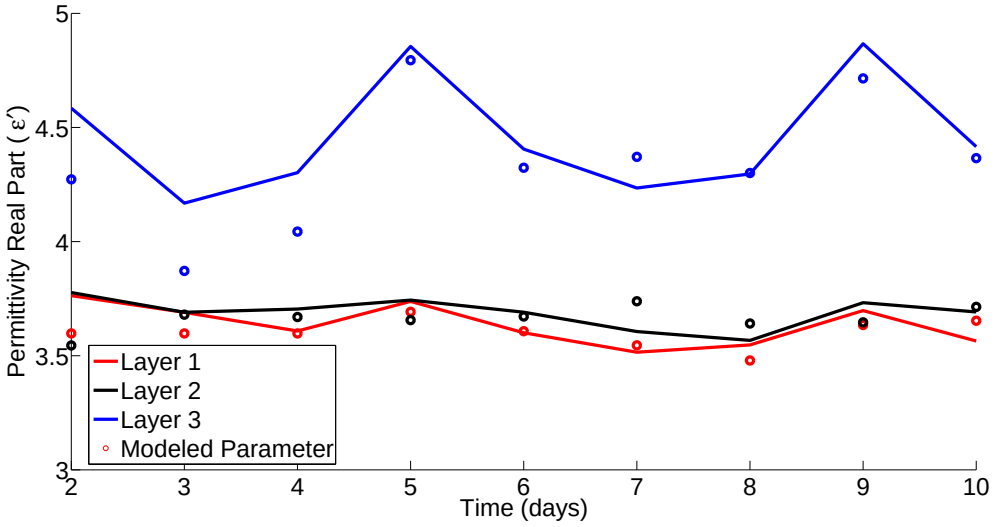

Fig. 7.14: The three layer simulated annealing results of the time series real part of permittivities using noisy simulated data.

Tab. 7.3: Simulated annealing parameters for a three layer noisy inversion.

Parameter	Value
N	500
L	100
P_s	0.4
P_f	10^{-2}
R	5
N_L	3

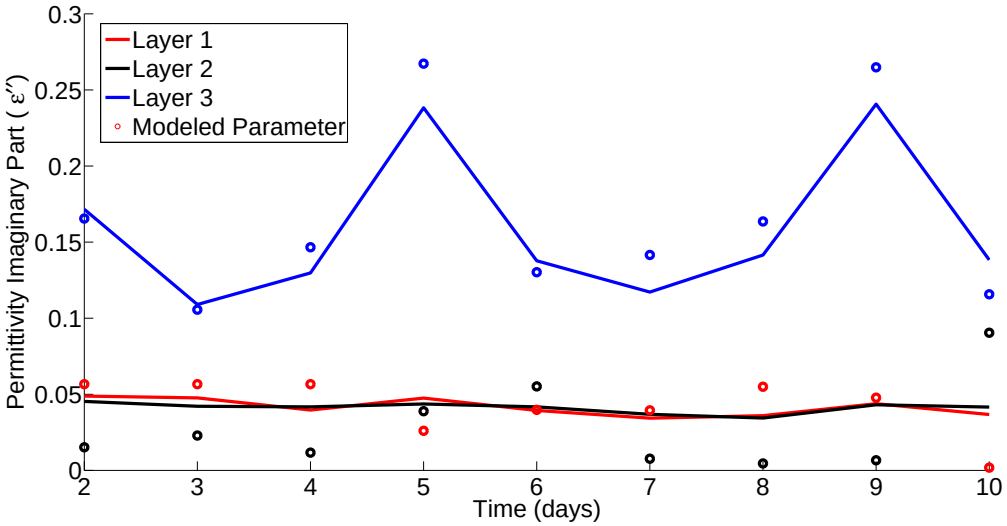

Fig. 7.15: The three layer simulated annealing results of the time series imaginary part of permittivities using noisy simulated data.

parameters in combinatorial problems. However, with this continuous value problem[2] we find that an impractical number of iterations would be required to be effective.

7.1.3 Single Layer Algorithm using Three Layer Data

In this section, we look to see how the single layer algorithm performs when given three layer synthetic data constructed using the forward solver. The three layer synthetic data is composed of three equally thick layers with very similar permittivities. The permittivities

[2] The unknown model parameters are not limited to discrete sets of values.

Tab. 7.4: Simulated annealing parameters for a single layer inversion of three layer synthetic data.

Parameter	Value
N	500
L	100
P_s	0.4
P_f	10^{-2}
R	10

are chosen relatively close to limit the effects caused by the reflections at the boundaries, since we know the single layer algorithm does not consider these reflections. The purpose of this section is to determine if our algorithm is capable of finding the effective permittivity of the three layers. In addition, to some extent, this example demonstrates a sea ice profile in which the permittivity has continuous variations, but does not have actual distinctive layers. The other advantage of this example is that the forward solver used to generate the synthetic data assumes three layers, and therefore, it is not identical to the one-layer forward solver used in the inversion algorithm.

For this simulation, we generated seven ice profiles with increasing thickness (to emulate a growth cycle of sea ice). The difference in the real part of permittivity between the three layers was approximately 1 and 0.01 in the imaginary part of the permittivity. WE performed a time series reconstruction of the complex permittivity of these three layer profiles to see if our algorithm could follow successive predictions. We used the free parameters in Table 7.4, and the results of this test are given in Figure 7.16 to Figure 7.18. The true parameter shown on the figures for the permittivities is the average value of the three layers. From these figures, we observe that our algorithm follows the general trend for all three model parameters.

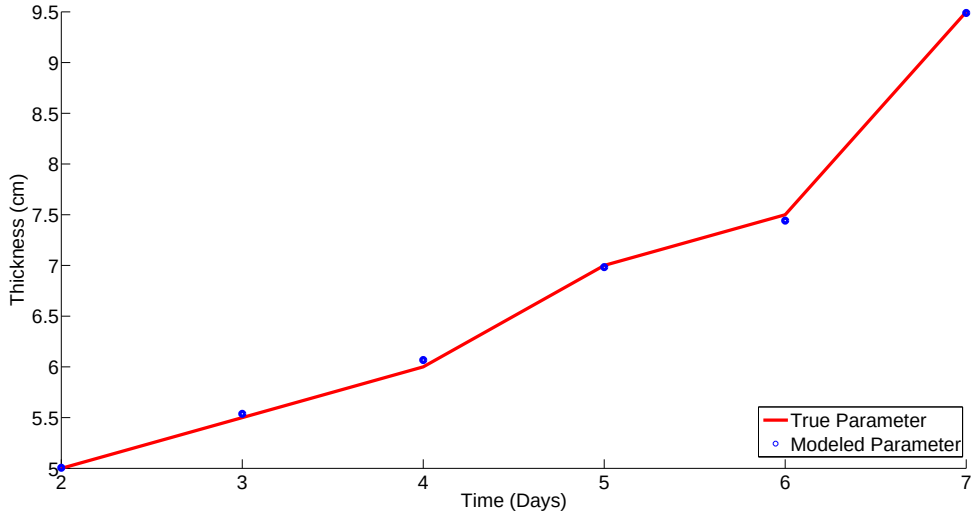

Fig. 7.16: The single layer simulated annealing results of the time series thickness using three layer synthetic data.

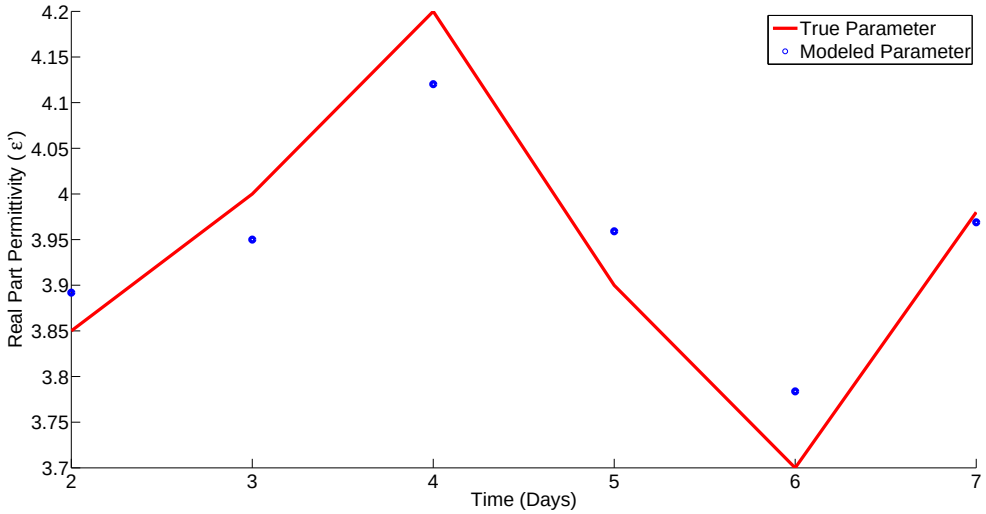

Fig. 7.17: The single layer simulated annealing results of the time series real part of permittivity using three layer synthetic data.

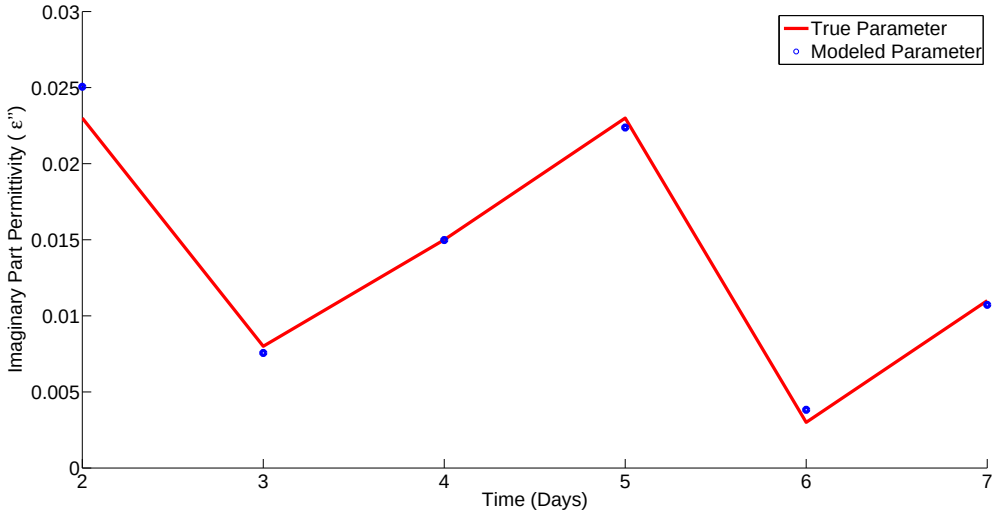

Fig. 7.18: The single layer simulated annealing results of the time series imaginary part of permittivity using three layer synthetic data.

7.2 Experimental Data Inversion

In this section, we implement our calibration factor on our measurements, and attempt to reconstruct the complex permittivity profile. The measurements we are inverting are those of SERF 2015. As shown in Section 5.2, we observed that our antenna was not sensitive beyond 10 cm (SERF 2015 experiments started at 24 cm). Therefore, using the single layer or three layer algorithm would not be practical as the antenna does not see the sea water. That is, if we modeled our physical system as a transmission line, our terminating load would not be sea water. In essence, the antenna sees a half space of sea ice, consisting of the first few centimeters of the sea ice. Therefore, we look to invert for the complex permittivity of ice grown at SERF 2015 assuming we have a half space[3]. It should be noted that this issue was also observed in our recent oil in sea ice experiment in which the inversion of radar cross section data was performed assuming a rough half space region of interest with a homogeneous complex permittivity profile [47].

[3] Consequently, the forward solver used in the inversion algorithm will only use a standard Fresnel reflection coefficient instead of the generalized one.

Before proceeding with our profile reconstruction, we note here that we had useable data for only the first four days. To this end, we will reconstruct the complex permittivity profile for these days. In addition, the complex permittivities do not vary drastically within this time frame. Therefore, we explore two calibrations in an attempt to reduce bias in reconstruction[4]. The first calibration uses the first day of the SERF 2015 measurements, and the second calibration uses the $|S_{11}|$ measurements of our antenna when placed against a UHMW plastic. (Of course, based on the calibration technique, it is expected that the closer the calibration object is to the unknown object, the more successful the data calibration will be.)

Using the technique outlined in Section 6.4, we generate our calibration factor based on the forward solver approximation and the true $|S_{11}|$ measurements of the first day. (That is, the calibration factor will be the ratio of the generated data by the forward solver due to the known calibration object to the measured data taken from the calibration object.) We then apply this calibration factor to all future measurements. The reconstruction method follows the same cooling schedule as the single layer algorithm, with slightly different free parameters given in Table 7.5. The results of the time series complex permittivity profile reconstruction are shown in Figure 7.19 and Figure 7.20. From these plots, the reconstructed profile is similar to the true profile. However, we do not have enough variation in the true parameters and not enough measurements to conclude that this method is reliable when using experimental data. That being said, the reconstruction results still follow the general trend of the true parameters.

To test the proposed method using a calibration object whose complex permittivity is different than that of sea ice, we decided to use a slab of UHMW plastic ($\epsilon_r = 2.3$) as the calibration object. Therefore, measurements were taken from this dielectric slab, and also

[4] If our starting model parameters are close to the true model parameters, the algorithm may give us reasonable results without actually effectively searching the search space of our cost function.

Tab. 7.5: Simulated annealing parameters for experimental data when using SERF calibration object.

Parameter	Value
N	1000
L	100
P_s	0.4
P_f	10^{-2}
R	2

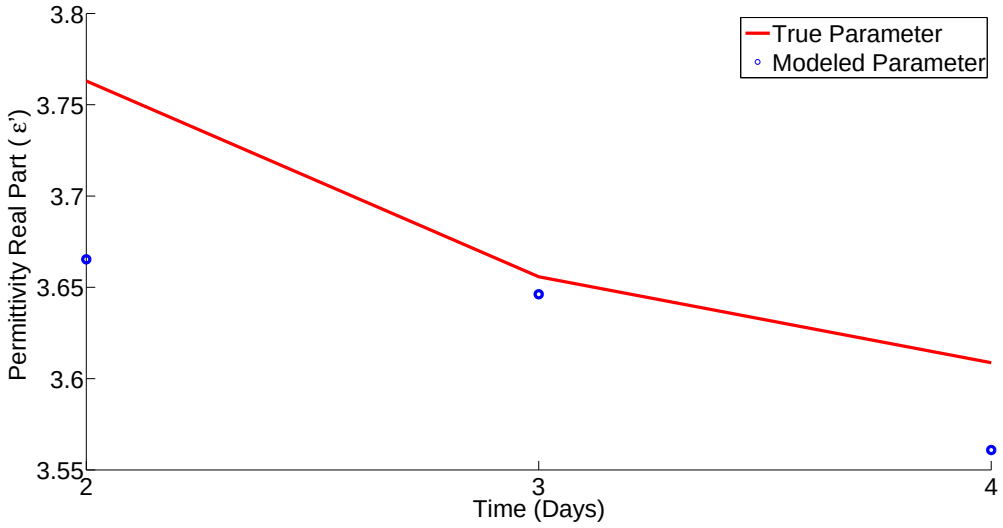

Fig. 7.19: The reconstructed time series profile of the surface permittivity (real part) using the initial measurement in the calibration factor.

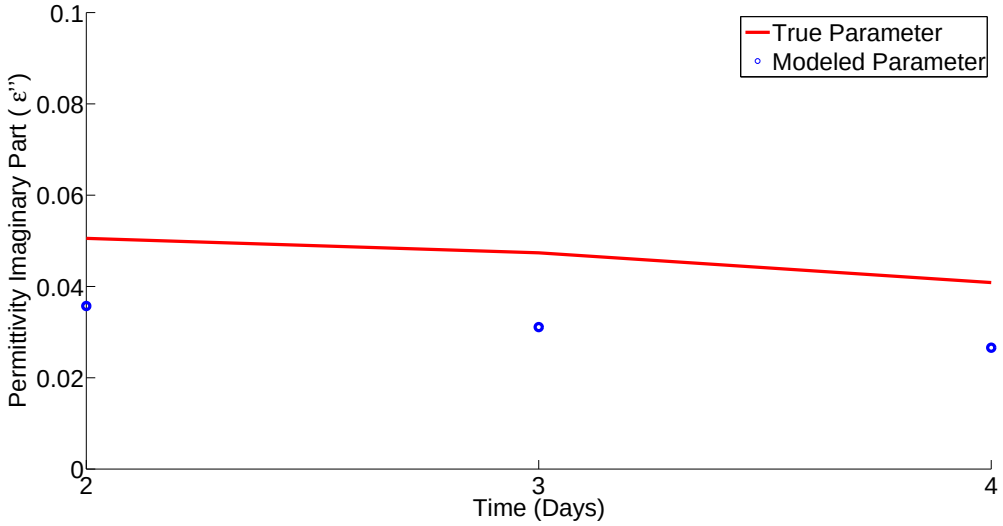

Fig. 7.20: The reconstructed time series profile of the surface permittivity (imaginary part) using the initial measurement in the calibration factor.

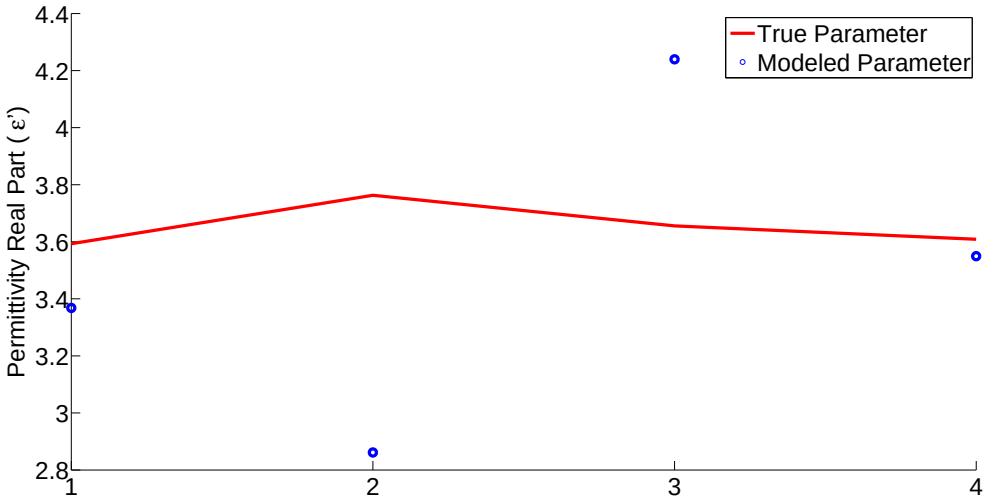

Fig. 7.21: The reconstructed time series profile of the surface permittivity (real part) using a measurement of a UHMW plastic as the calibration object.

the forward solver (assuming a half space region) was utilized to generate the synthetic data. The ratio of this synthetic data to the measured data was then used as the calibration factor to calibrate our SERF 2015 experiments. This enables us to see if our calibration technique still holds with a larger change in permittivity. The inversion results are presented in Figure 7.21 and Figure 7.22. (Note that we have now also included the first day of measurements since it is not being used for calibration.) From these figures, we can see that the reconstructed profile is worse than when using a calibration factor determined from the first day's measurement. This is to be expected as the profile used for calibration is fairly different compared to the profile we are attempting to reconstruct. It should also be noted that the other reason that the inversion using the dielectric slab calibration is worse than the inversion using the first day's SERF measurement calibration may lie in the fact that the dielectric slab was lossless, whereas the unknown profile is a lossy profile.

For the results presented in this section, we have shown that our inversion algorithm is capable of following the general trend of our model parameters when given simulated data that is both noiseless and noisy. With regards to measured data, we see there is potential to

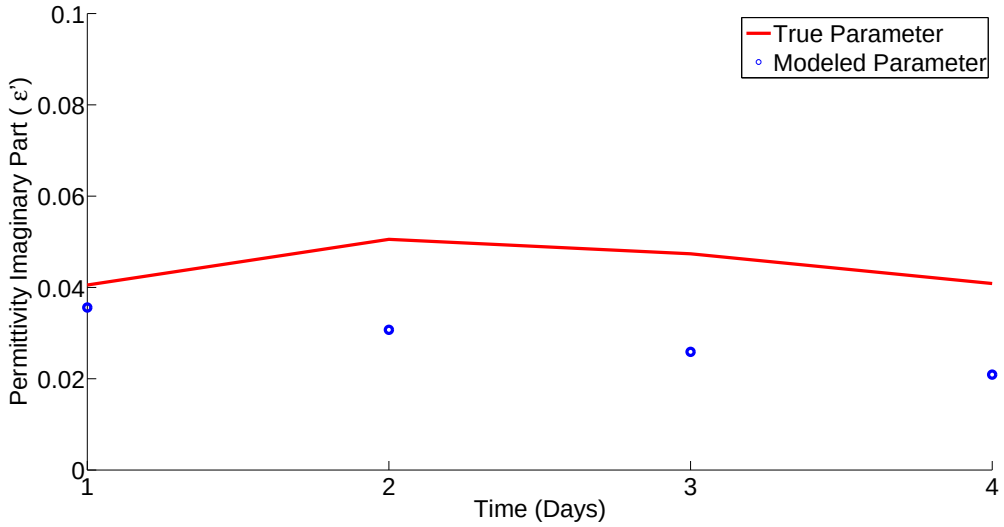

Fig. 7.22: The reconstructed time series profile of the surface permittivity (imaginary part) using a measurement of a UHMW plastic as the calibration object.

this method if successful calibration can be performed. We note that our measured data is fairly limited and that the next step would be collecting further measurements with a larger variation in complex permittivity and thickness values.

8

Conclusion

This thesis addressed an electromagnetic inversion problem in which external active microwave measurements are to be used to infer some internal properties of the region of interest. To this end, a surface based OEW was designed, and fabricated with the intent of irradiating first year sea ice to collect $|S_{11}|$ measurements. From these measurements, the time-series complex permittivity profile of the sea ice was to be reconstructed using the proposed inversion algorithm. This profile is important, as it provides information about key geophysical properties of sea ice. The main advantage of this approach is that it could potentially be utilized as a network of sensors monitoring local properties and regional properties of the Arctic. This could be, for example, important in sensitive areas in which oil spills might happen.

For simplicity of the system, we decided to use a multi-frequency phaseless approach without spatial or angular variations in our measurements. This definitely reduced the information content of the measured data; however, the antenna can be stationary on the region of

interest. To this end, the antenna was designed to have frequency bands where the magnitude of the reflected voltage ratio was less than -10 dB. This would indicate power being transmitted into the sea ice layer. To alleviate the challenges with having accurate phase measurements and also to make the proposed method more cost efficient, we decided to only consider the magnitude of the measured data; *i.e.*, we utilized phaseless data. (This approach will then only require a power meter.) Once measured data are collected, it needed to be processed by an inversion algorithm to reconstruct the desired unknowns. The proposed inversion algorithm consisted of a global optimization technique known as simulated annealing in conjunction with a transmission line based forward solver. This inversion algorithm is iterative, and minimize the data misfit cost function which represents the discrepancy between the measured data and the simulated data. One of the challenges in this approach was to properly link the simulation model to the actual physics. Inspired by microwave tomography calibration techniques, a calibration process was proposed to alleviate this discrepancy.

We first validated our inversion algorithm using noiseless and noisy simulated data. The reconstructed profiles followed the general trend of the true time-series profiles. We then looked towards reconstructing our profile based on actual measurements. To this end, we performed measurements during 2015 and 2016 in the sea ice environmental facility at the University of Manitoba. Herein, we collected antenna measurements as well as performed physical sampling of the sea ice. From our physical samples, we determined the salinity, temperature, and thickness of the ice layers of SERF 2015. Using dielectric mixing models, we determined the complex permittivity profile of the sea ice. This data was used in creating and analyzing the validity of our inversion algorithm. In addition, we performed cold lab experiments to gauge the sensitivity of our antenna to the geophysical properties of sea ice. We found that our antenna's sensitivity was fairly weak in regards to the salinity and temperature of the sea ice. The OEW was most sensitive to the thickness of the sea ice up until the sea ice became thicker than a certain depth. We also found out that this technique

would only work in winter during the freezing cycle, as melting causes high conductive surface layers of water that prevent the antenna from penetrating into the ice at all. Regarding experimental data inversion, only a few days of SERF 2015 measurements were useable for the inversion; much more experimental work is needed to evaluate this approach. Based on our limited data set, we presented preliminary experimental reconstruction results for this approach. From these results, there is potential of being able to monitor the diurnal effects on the surface layers of the sea ice.

For future work, the following four directions are suggested. First, the main data collection challenge that we had was the limited sensitivity of the antenna to deeper parts of the region of interest. Therefore, an enhanced design for the antenna element is recommended. However, it should be noted that the antenna is to work in its near-field zone. Thus, it is speculated that the antenna should exhibit a focused near-field distribution to be more sensitive to deeper parts of the region of interest. That is, we would have the opportunity to monitor other convective processes that occur near the bottom of the ice. Second, the idea behind the proposed inversion process is not limited to the choice of simulated annealing, and the transmission line based forward solver. Other optimization techniques and more realistic forward solvers can be investigated for this approach. In particular, more realistic forward solvers could be very useful; however, a more complicated forward solver may result in more unknowns to be reconstructed. Third, novel data calibration techniques should be investigated to better link the forward solver to the actual wave propagation in the region of interest. Last but not least, more extensive measured data sets need to be used to evaluate this technique, and optimize its different components: antenna, forward solver, calibration technique, and optimization algorithm. The challenge in doing so lies in the fact that these components are linked together, and affect each other. Thus, they should be ideally considered together.

APPENDIX

A

Dielectric Mixing Model Calculations

In this appendix, the dielectric mixing models of sea water, sea ice, and snow are presented in full. The derivation of these models are from [14].

A.1 Sea Water Empirical Dielectric Model

The empirical dielectric model for sea water used in this thesis is based off of previous models [20]. The new model parameters were interpolated using sea water permittivity data sets collected by Ellison (1996, 1997, and 2003) and Stogryn (1996) [19, 21, 22, 23]. The complex permittivity of sea water is a function of frequency (GHz), temperature ($^{\circ}C$), and salinity (psu) given by:

$$\begin{aligned}\epsilon_w(f,T,S) =& \frac{\epsilon_{ws}(T,S)-\epsilon_{w1}(T,S)}{1-j2\pi f\tau_{w1}(T,S)} + \frac{\epsilon_{w1}(T,S)-\epsilon_{w\infty}(T,S)}{1-j2\pi f\tau_{w2}(T,S)} \\ &+ \epsilon_{\infty}(T,S) + j\frac{\sigma_i}{2\pi\epsilon_0 f},\end{aligned} \tag{A.1}$$

where ϵ_0 is the permittivity of free space, ϵ_{ws} is the static permittivity, ϵ_∞ is considered as a fitting parameter, f is the frequency, τ is the relaxation time constants of the polar molecules, and σ_i is the ionic conductivity. ϵ_{ws} and ϵ_{w1} are given by:

$$\epsilon_{ws}(T,S) = 87.85306e^{-0.00456992T - a_1 S - a_2 S^2 - a_3 ST}, \tag{A.2}$$

$$\epsilon_{w1}(T,S) = a_4 e^{-a_5 T - a_6 S - a_7 ST}. \tag{A.3}$$

The relaxation time constant relates to a frequency dependent phenomenon where the dielectric loss increases due to dipole relaxation [24]. Dipole relaxation time is the time delay in molecular polarization with respect to a changing electric field. The polar molecules are unable to reach equilibrium (re-orientate) as frequency increases. This inability results in higher losses due to the molecules rotating against the electric field. However, the losses caused by polarization decrease as frequency further increases due to molecules not having enough time to even begin to rotate.

In the double-Debye model, there are two relaxation time constants which are influenced by the salinity and temperature of the sea water. The relationship between τ, S, and T are:

$$\tau_{w1}(T,S) = (a_8 + a_9 S)e^{\frac{a_{10}}{T+a_{11}}}\ \texttt{ns}, \tag{A.4}$$

$$\tau_{w2}(T,S) = (a_{12} + a_{13} S)e^{\frac{a_{14}}{T+a_{15}}}\ \texttt{ns}. \tag{A.5}$$

As well,$\epsilon_{w\infty}$ and $\sigma_i(T,S)$ are given by:

$$\epsilon_{w\infty}(T,S) = a_{16} + a_{17}T + a_{18}S, \tag{A.6}$$

$$\sigma_i(T,S) = \sigma(T,35) \cdot P(S) \cdot Q(T,S), \tag{A.7}$$

where the parameters of $\sigma_i(T, S)$ are:

$$\begin{aligned}\sigma(T, 35) = 2.903602 + 8.607 \cdot 10^{-2}\, T + 4.738817 \cdot 10^{-4}\, T^2 \\ -2.991 \cdot 10^{-6}\, T^3 + 4.3041 \cdot 10^{-9}\, T^4,\end{aligned} \tag{A.8}$$

$$P(S) = S\frac{37.5109 + 5.45216S + 0.014409S^2}{1004.75 + 182.283S + S^2}, \tag{A.9}$$

$$Q(T, S) = 1 + \frac{\alpha_0(S) \cdot (T - 15)}{T - \alpha_1(S)}, \tag{A.10}$$

where the parameters of $Q(T, S)$ are determined by:

$$\alpha_0(S) = \frac{6.9431 + 3.2841S - 0.099486S^2}{84.85 + 69.024S + S^2}, \tag{A.11}$$

$$\alpha_1(S) = 49.843 - 0.2276S + 0.00198S^2. \tag{A.12}$$

The table below lists the a values of Equations (A.2 to A.6). These values are only valid over the following ranges:

$$0°\text{C} \leq T \leq 30°\text{C}, \quad 0 \text{ psu} \leq S \leq 40 \text{ psu}, \quad 0 \text{ GHz} \leq f \leq 1000 \text{ GHz}$$

These formulas were determined through experimental data inclusive to these ranges. Therefore, the error is unknown outside of these conditions. However, the use of these formulas outside these ranges have been used [20]. This thesis uses the following ranges:

$$T = -1.8°\text{C}, \quad S = 32.54 \text{ psu}, \quad 3 \text{ GHz} \leq f \leq 6 \text{ GHz}$$

Tab. A.1: Values of a used in the empirical dielectric modeling of sea water.

$a_1 = 0.46606917E-2$
$a_2 = -0.26087876E-4$
$a_3 = -0.63926782E-5$
$a_4 = 0.63000075E+1$
$a_5 = 0.26242021E-2$
$a_6 = -0.42984155E-2$
$a_7 = 0.34414691E-4$
$a_8 = 0.17667420E-3$
$a_9 = -0.20491560E-6$
$a_{10} = 0.58366888E+3$
$a_{11} = 0.12684992E+3$
$a_{12} = 0.69227972E-4$
$a_{13} = 0.38957681E-6$
$a_{14} = 0.30742330E+3$
$a_{15} = 0.12634992E+3$
$a_{16} = 0.37245044E+1$
$a_{17} = 0.92609781E-2$
$a_{18} = -0.26093754E-1$

A.2 Sea Ice Empirical Dielectric Model

The model used in computing the complex permittivity of sea ice, ϵ_{si}, is a function of the following parameters:

- Complex permittivity of pure ice, ϵ_i.
- Complex permittivity of brine inclusions, ϵ_b.
- Brine volume fraction, v_b.
- The shape and orientation of the brine inclusions.

ϵ_{si} is also a function of the ice temperature T and the ice salinity S_i. The Polder-van Santen/de Loor formulas are used to determine the effective permittivity of the sea ice based on

the brine inclusions' shape. The inclusion shapes considered are circular disc, spherical, and needles; the orientation is assumed random. The resulting complex effective permittivity is based on the host material and the inclusion material where the equations are:

$$\epsilon_{si} = \epsilon_i + \frac{v_b}{3}(\epsilon_b - \epsilon_i)\left(2 + \frac{\epsilon^\star}{\epsilon_b}\right) \quad \text{(Circular Disc)}, \tag{A.13a}$$

$$\epsilon_{si} = \epsilon_i + 3v_b\epsilon^\star\frac{\epsilon_b - \epsilon_i}{\epsilon_b + 2\epsilon^\star} \quad \text{(Spherical)}, \tag{A.13b}$$

$$\epsilon_{si} = \epsilon_i + v_b\frac{(\epsilon_b - \epsilon_i)(5\epsilon^\star + \epsilon_b)}{3(\epsilon_b + \epsilon^\star)} \quad \text{(Needle)}, \tag{A.13c}$$

where $\epsilon^\star$ is an effective permittivity for the region surrounding an inclusion. If the inclusion volume fraction is small, we assume $\epsilon^\star = \epsilon_i$. If the volume fraction of the inclusions is larger, the model assumes $\epsilon^\star = \epsilon_{si}$. The empirical formulas for ϵ_i, ϵ_b, and v_b are given in the following sections.

A.2.1 Permittivity of Pure Ice

Pure ice, ϵ_i, is assumed the host material of sea ice. The relaxation frequencies of pure ice is in the KHz region, where the relaxation frequencies of liquid water is in the microwave region. Since this thesis utilizes microwave frequencies, the model is of the form:

$$\epsilon_i' \approx \epsilon_{i\infty}, \tag{A.14}$$

$$\epsilon_i'' \approx \frac{\epsilon_{i0} - \epsilon_{i\infty}}{2\pi f\tau_i}, \tag{A.15}$$

where ϵ_i' can be assumed independent of frequency from 10 MHz to 300 GHz. A weak temperature dependence was exhibited in a study [50]. This resulted in the following empirical

formula:

$$\begin{aligned}\epsilon_i' =& 3.1884 + 9.1 \times 10^{-4} T \\ & -40^\circ C \leq T \leq 0^\circ C,\end{aligned} \tag{A.16}$$

Pure ice has an infrared absorption spectrum that varies with frequency. Equation (A.15) can be redefined by the following equation [51]:

$$\epsilon_i'' = \frac{\alpha_0}{f} + \beta_0 f, \tag{A.17}$$

where α_0 and β_0 are defined by:

$$\alpha_0 = (0.00504 + 0.0062\theta) \cdot exp(-22.1\theta) GHz, \tag{A.18}$$

$$\begin{aligned}\beta_0 =& \frac{B_1}{T_K} \frac{exp(b/T_K)}{[exp(b/T_K) - 1]^2} + B_2 f^2 \\ & + exp[-9.963 + 0.0372(T_K - 273.16)] GHz,\end{aligned} \tag{A.19}$$

where $\theta = \frac{300}{T_K} - 1$ (T_K in K), $B_1 = 0.0207$ K/GHz, $b = 335$K, and $B_2 = 1.16 \times 10^{-11}$ GHz^{-3}.

A.2.2 Permittivity of Brine

Liquid brine is another name for saline or sea water. Therefore, the same expressions as A.1 can be used. However, two modifications must be made to in order to find brine salinity [20]. The first modification relates to the dependence brine salinity has to temperature. As the temperature of sea ice varies, the size of the brine inclusions change due to freezing or melting of the ice. This change in size alters the brine's salt concentration. The salinity of

brine in sea ice can be determined using the following empirical formulas:

$$\begin{aligned} S_b =& 1.725 - 18.756T - 0.3964T^2, \\ & -8.2^\circ C \leq T \leq -2^\circ C; \end{aligned} \tag{A.20}$$

$$\begin{aligned} S_b =& 57.041 - 9.929T - 0.16204T^2 - 0.002396T^3, \\ & -22.9^\circ C \leq T \leq -8.2^\circ C; \end{aligned} \tag{A.21}$$

$$\begin{aligned} S_b =& 242.94 + 1.5299T + 0.0429T^2, \\ & -36.8^\circ C \leq T \leq -22.9^\circ C; \end{aligned} \tag{A.22}$$

$$\begin{aligned} S_b =& 508.18 + 14.535T + 0.2018T^2, \\ & -43.2^\circ C \leq T \leq -36.8^\circ C. \end{aligned} \tag{A.23}$$

Secondly, the formulas in A.1 are only valid for salinity of ≤ 40 psu. The following formulas cover the range $0 \leq S \leq 157$ psu:

$$\epsilon_b' = \epsilon_{w\infty} + \frac{\epsilon_{b0} - \epsilon_{w\infty}}{1 + (2\pi f \tau_b)^2}, \tag{A.24}$$

$$\epsilon_b'' = (2\pi f \tau_b) \frac{(\epsilon_{b0} - \epsilon_{w\infty})}{1 + (2\pi f \tau_b)^2} + \frac{\sigma_b}{2\pi f \epsilon_0}, \tag{A.25}$$

where $\epsilon_{w\infty} = 4.9$,

$$\epsilon_{b0}(T, N_b) = \epsilon_{b0}(T, 0)\, a_1(N_b), \tag{A.26}$$

$$\tau_b(T, N_b) = \tau_b(T, 0)\, b_1(T, N_b), \tag{A.27}$$

$$\sigma_b(T, N_b) = \sigma_b(25, N_b)\, c_1(\Delta, N_b). \tag{A.28}$$

The previous functions are determined by the following:

$$\begin{aligned}\epsilon_{b0}(T,0) =& 88.045 - 0.4147T + 6.295 \times 10^{-4}T^2 \\ &+ 1.075 \times 10^{-5}T^3,\end{aligned} \tag{A.29}$$

$$\begin{aligned}a_1(N_b) =& 1.0 - 0.255N_b + 5.15 \times 10^{-2}N_b^2 \\ &- 6.89 \times 10^{-3}N_b^3,\end{aligned} \tag{A.30}$$

$$\begin{aligned}2\pi\tau_b(T,0) =& 1.1109 \times 10^{-10} - 3.824 \times 10^{-12}T \\ &+ 6.938 \times 10^{-14}T^2 - 5.096 \times 10^{-16}T^3,\end{aligned} \tag{A.31}$$

$$\begin{aligned}b_1(T,N_b) =& 1.0 + 0.146 \times 10^{-2}TN_b - 4.89 \times 10^{-2}N_b \\ &- 2.97 \times 10^{-2}N_b^2 + 5.64 \times 10^{-3}N_b^3,\end{aligned} \tag{A.32}$$

$$\begin{aligned}\sigma_b(25,N_b) =& N_b(10.39 - 2.378N_b + 0.683N_b^2 \\ &- 0.135N_b^3 + 1.01 \times 10^{-2}N_b^4),\end{aligned} \tag{A.33}$$

$$\begin{aligned}c_1(\Delta,N_b) =& 1.0 - 1.96 \times 10^{-2}\Delta + 8.08 \times 10^{-5}\Delta^2 \\ &- N_b\Delta[3.02 \times 10^{-5} + 3.92 \times 10^{-5}\Delta \\ &+ N_b(1.72 \times 10^{-5} - 6.58 \times 10^{-6}\Delta)],\end{aligned} \tag{A.34}$$

where $\Delta = (25 - T)$ in $^\circ C$.

$$\begin{aligned}N_b =& S_b(1.707 \times 10^{-2} + 1.205 \times 10^{-5}S_b \\ &+ 4.058 \times 10^{-9}S_b^2).\end{aligned} \tag{A.35}$$

A.2.3 Brine Volume Fraction

The brine volume fraction in sea ice is determined by the salinity of the ice and brine, given by:

$$v_b = \frac{S_i}{S_b}\frac{\rho_i}{\rho_b}, \tag{A.36}$$

where ρ_i and ρ_b are the density of ice and brine, respectively. An empirical expression exists for the volume fraction of brine and is determined by:

$$\begin{aligned} v_b =& 10^{-3} S_i \left(-\frac{49.185}{T} + 0.0532 \right), \\ & -22.9^{\circ}C \leq T \leq -0.5^{\circ}C, \end{aligned} \tag{A.37}$$

A.3 Snow Empirical Dielectric Model

The dielectric properties of snow can be divided into two categories, (1) dry snow, and (2) wet snow. Dry and wet snow are a mixture of ice and air, but wet snow additionally contains free water. The following sections will give the derivation the complex permittivity of both cases.

A.3.1 Permittivity of Dry Snow

Dry snow is a mixture of ice and air. The Dry snow permittivity ϵ_{ds} is dependent on ice permittivity ϵ_i, air permittivity ϵ_{air}, and the ice volume factor v_i. The volume fraction is related to the snow density p_s by the following equation:

$$v_i = \frac{\rho_s}{0.9167} \ g/cm^3, \tag{A.38}$$

where 0.9167 g/cm^3 is the density of pure ice. The following approximations are made for ϵ_r and ϵ_{air}:

- ϵ_{air} is considered the host in the mixing model.
- ϵ_i is considered the inclusion in the mixing model.
- $\epsilon_{air} = 1$

The mixing model used for dry snow is the Tinga-Voss-Blossey (TVB) formula for spherical inclusions, given by Equation (A.39). The difference between TVB and the Polder-van Santen/de Loor formulas are the way in which the host material surrounds the inclusions. In the TVB formulas, the ellipsoid inclusions are surrounded by an outer ellipsoid representing the host material. Whereas, in the latter models, the ellipsoid inclusions are surrounded completely by the host material, or ellipsoid host material is surrounded by the inclusions.

$$\epsilon_{ds} = \epsilon_{air} + \frac{3v_i\epsilon_{air}(\epsilon_i - \epsilon_{air})}{(2\epsilon_{air} + \epsilon_i) - v_i(\epsilon_i - \epsilon_{air})}, \tag{A.39}$$

which reduces to the following:

$$\epsilon_{ds} = 1 + \frac{3v_i(\epsilon_i - 1)}{(2 + \epsilon_i) - v_i(\epsilon_i - 1}). \tag{A.40}$$

According to Section A.2.1, ϵ_i' is frequency independent at microwave bands and has a small temperature dependence. As well, $\epsilon_i'' \ll \epsilon_i'$. Using the simplification of $\epsilon_i = 3.17$ in (A.40) results in:

$$\epsilon_{ds}' \approx \frac{1 + 0.84v_i}{1 - 0.42v_i}. \tag{A.41}$$

The loss factor ϵ_{ds}'' is derived in[52] and is given in Equation (A.42).

$$\epsilon''_{ds} = \frac{9 v_i \epsilon''_i}{[(2+v_i) + \epsilon'_i(1-v_i)]^2} \tag{A.42}$$

When setting $\epsilon'_i = 3.17$, the equation simplifies to:

$$\epsilon''_{ds} = \frac{0.34 v_i \epsilon''_i}{(1-0.42 v_i)^2} \tag{A.43}$$

A.3.2 Permittivity of Wet Snow

$$\epsilon'_{ws} = A + \frac{B m_v^x}{1+(f/f_0)^2}, \tag{A.44}$$

$$\epsilon''_{ws} = \frac{C(f/f_0) m_v^x}{1+(f/f_0)^2}, \tag{A.45}$$

$$A = A_1(1.0 + 1.83\rho_s + 0.02 m_v^{1.015}) + B_1, \tag{A.46}$$

$$B = 0.073 A_1, \tag{A.47}$$

$$C = 0.073 A_2, \tag{A.48}$$

$$x = 1.31, \tag{A.49}$$

$$f_0 = 9.07\ GHz, \tag{A.50}$$

$$A_1 = 0.78 + 0.03f - 0.58 \times 10^{-3} f^2, \tag{A.51}$$

$$A_2 = 0.97 - 0.39f \times 10^{-2} + 0.39 \times 10^{-3} f^2, \tag{A.52}$$

$$B_1 = 0.31 - 0.05f + 0.87 \times 10^{-3} f^2, \tag{A.53}$$

where f is in GHz.

Bibliography

[1] (2016) All about sea ice. Online. National Snow and Ice Data Center. [Online]. Available: http://nsidc.org/cryosphere/seaice/index.html

[2] M. Shokr and N. Sinha, *Sea Ice: Physics and Remote Sensing*. John Wiley & Sons, American Geophysical Union, 2015.

[3] J. Fattahi and D. Spinello, "Sensing linear viscoelastic constitutive parameters with a timoshenko beam on a multi-layer foundation: Modeling and simulation," *Sensing and Bio-Sensing Research*, 2015.

[4] P. Mojabi, N. Firoozy, N. Bayat, T. Brown, C. Narendra, P. Mojabi, C. Niu, T. Tiede, T. Neusitzer, X. Li, I. Jeffrey, J. LoVetri, and D. Barber, "Electromagnetic inversion for biomedical imaging, antenna characterization, and sea ice remote sensing applications," in *2016 URSI Asia-Pacific Radio Science Conference (URSI AP-RASC)*, Aug 2016, pp. 586–589.

[5] J. Stroeve, M. M. Holland, W. Meier, T. Scambos, and M. Serreze, "Arctic sea ice decline: Faster than forecast," *Geophysical Research Letters*, vol. 34, no. 9, pp. n/a–n/a, 2007, l09501. [Online]. Available: http://dx.doi.org/10.1029/2007GL029703

[6] W. S. Pegau, J. Garron, and L. Zabilansky, "Detection of oil on-in-and-under ice," Arctic Response Technology: Oil Spill Preparedness, Tech. Rep., 2016.

[7] (2013, October) Natural resources canada. [Online]. Available: http://www.nrcan.gc.ca

[8] N. Firoozy, A. S. Komarov, P. Mojabi, D. G. Barber, J. C. Landy, and R. K. Scharien, "Retrieval of young snow-covered sea-ice temperature and salinity evolution through radar cross-section inversion," *IEEE Journal of Oceanic Engineering*, vol. 41, no. 2, pp. 326–338, April 2016.

[9] D. Lubin and R. Massom, *Polar Remote Sensing Volume 1: Atmosphere and Oceans*, Springer, Ed. Praxis Publishing Ltd, 2006.

[10] P. Wadhams. (2003, January) How does Arctic sea ice form and decay? National Oceanic and Atmospheric Administration. [Online]. Available: http://www.arctic.noaa.gov/essay_wadhams.html

[11] W. F. Weeks, "Sea ice conditions in the Arctic," University of Washington, Tech. Rep., 1976.

[12] K. Kerry and G. Hempel, *Antarctic Ecosystems: Ecological Change and Conservation*, Springer, Ed., 1990.

[13] M. A. Lange, "Development of sea ice in the Weddell Sea," *Annals of Glaciology*, 1989.

[14] F. Ulaby and D. Long, *Microwave Radar and Radiometric Remote Sensing*. The University of Michigan Press, 2014.

[15] N. O. Service, "What is remote sensing?" online, May 2015.

[16] NASA, "Remote sensors," https://earthdata.nasa.gov/user-resources/remote-sensors, December 2016.

[17] X. Li, "Investigation of the interative technique for phaseless planar near-field antenna measurements," Master's thesis, University of Manitoba, 2015.

[18] W. C. Chew, *Waves and Fields in Inhomogeneous Media*, D. G. Dudley, Ed. IEEE PRESS, 1995.

[19] W. J. Ellison, , A. Balana, and G. Delbos, "Study and measurement of the dielectric properties of sea water: Final report," ESTEC/ESA, Tech. Rep., 1996.

[20] C. Mätzler, *Thermal Microwave Radiation: Applications for Remote Sensing*. The Institution of Engineering and Technology, 2006.

[21] W. J. Ellison, A. Balana, and K. Lamkaouchi, "Dielectric properties of sea water in the range 30-105 GHz: Final report," ESTEC/ESA, Tech. Rep., 1997.

[22] W. Ellison, S. English, and K. Lamkaouchi, "A comparison of ocean emissivity models using the advanced microwave sounding unit, the special sensor microwave imagery, the TRMM microwave imagery, and airborne radiometer observations," *Geophysical Research*, 2003.

[23] A. Stogryn, H. Bull, K. Ruayi, and S. Iravanchy, "The microwave permittivity of sea and freshwaterwater," Aerojet, Tech. Rep., 1996.

[24] S. J. Rzoska and V. P. Zhelezny, *Nonlinear Dielectric Phenomena in Complex Liquids*. Kluwer Academic Publishers, 2004.

[25] R. C. Aster, B. Borchers, and C. H. Thurber, *Parameter Estimation and Inverse Problems*, E. Inc., Ed. Academic Press, 2013.

[26] W. Menke, *Geophysical Data Analysis: Discrete Inverse Theory*. Elsevier Ltd., 2012.

[27] H. M. Iyer and K. Hirahara, *Seismic Tomography: Theory and Practice*. Chapman Hall, 1993.

[28] K. Siegrist. (2015) The central limit theorem. University of Alabama. [Online]. Available: http://www.math.uah.edu/stat/sample/CLT.html

[29] Y. Fang, "Imaging from sparse measurements," Ph.D. dissertation, Rensselaer Polytechnic Institute, 2008.

[30] L. Liberti and N. Maculan, *Global Optimization: From Theory to Implementation*. Springer Springer+ Business Media, Inc, 2006.

[31] C. P. Robert and G. Casella, *Monte Carlo Statistical Methods*. Springer Springer+ Business Media, Inc, 2004.

[32] F.Humphreys and M. Hatherly, *Recrystallization and Related Annealing Phenomena*. Elsevier Ltd., 2004.

[33] S. N. Sivanandam and S. N. Deepa, *Introduction to Genetic Algorithms*. Springer Springer+ Business Media, Inc, 2008.

[34] K. E. Parsopoulos and M. N. Vrahatis, *Particle Swarm Optimization and Intelligence*, K. Klinger, Ed. Information Science Reference, 2010.

[35] A. Rollett, G. S. Rohrer, F. Humphreys, and M. Hatherly, *Recrystallization and Related Annealing Phenomena*. Elsevier Ltd., 2004.

[36] A. Corana, M. Marchesi, C. Martini, and S. Ridella, "Minimizing multimodal functions of continuous variables with the simulated annealing algorithm," *ACM Transactions on Mathematica Software*, 1987.

[37] P. J. M. van Laarhoven and E. H. L. Aarts, *Simulated Annealing: Theory and Applications*, F. Calogero, Ed. Springer-Science and Business Media, 1992.

[38] D. Jackson and N. Alexopoulos, "Gain enhancement methods for printed circuit antennas," *IEEE Transactions on Antennas and Propagation*, vol. 33, no. 9, pp. 976–987, Sep 1985.

[39] H. Liu, X. Xie, and M. Sato, "New ground penetrating radar system for quantitative characterization of snow and sea ice," in *Radar Conference 2013, IET International*, April 2013, pp. 1–5.

[40] N. Bayat and P. Mojabi, "On an antenna design for 2d scalar near-field microwave tomography," *ACES*, 2015.

[41] R. F. Harrington, *Time-Harmonic Electromagnetic Fields*, D. G. Dudley, Ed. Wiley-IEEE Press, 1961.

[42] D. M. Pozar, *Microwave Engineering*. John Wiley & Sons, 2012.

[43] W. Fuscaldo, G. Valerio, A. Galli, R. Sauleau, A. Grbic, and M. Ettorre, "Higher-order leaky-mode bessel-beam launcher," *IEEE Transactions on Antennas and Propagation*, vol. 64, no. 3, pp. 904–913, March 2016.

[44] P. M. van den Berg and R. E. Kleinman, "A contrast source inversion method," *Inverse Problems*, vol. 13, no. 6, p. 1607, 1997. [Online]. Available: http://stacks.iop.org/0266-5611/13/i=6/a=013

[45] W. S. Bigelow and E. G. Farr, "Impulse propogation measurements of the dielectric properties of several polymer resins," Farr Research, Inc, Tech. Rep., 1999.

[46] "Duravar uhmw-pe," Artek Inc, Tech. Rep., 2013.

[47] N. Firoozy, T. Nuesitzer, D. Desmond, T. Tiede, M. Lemes, J. Landy, P. Mojabi, S. Rysgaard, G. Stern, and D. Barber, "Electromagnetic detection of crude oil spill in young sea ice- a case study," *IEEE Transactions on Geoscience and Remote Sensing*, 2017.

[48] T. Brown, "Antenna characterization using phaseless near-field measurements," Master's thesis, 2016.

[49] M. Ostadrahimi, P. Mojabi, C. Gilmore, A. Zakaria, S. Noghanian, S. Pistorius, and J. LoVetri, "Analysis of incident field modeling and incident/scattered field calibration techniques in microwave tomography," *IEEE Antennas and Wireless Propagation Letters*, vol. 10, pp. 900–903, 2011.

[50] C. Matzler and U. Wegmuller, "Dielectric properties of freshwater ice at microwave frequencies," *Journal of Physics D: Applied Physics*, 1987.

[51] H. Liebe, G. Hufford, and T.Manabe, "A model for the complex permittivity of water at frequencies below 1 THz," *International Journal of Infrared and Millimeter Waves*, 1991.

[52] M. T. Hallikainen, F. T. Ulaby, and M. Abdelrazik, "The dielectric properties of snow in the 3 to 36 GHz range," *IEEE Transactions on Antennas and Propagation*, 1986.